Receiver Function Analysis of Broadband Seismic Data from Various Seismic Stations and Modelling the Crustal Structure of Northeast India

A Thesis Submitted in Partial Fulfillment of the
Requirements for the Degree of Doctor of Philosophy

Nava Kumar Hazarika

Registration No. 159 of 1998-99

School of Science & Technology
Department of Physics
Tezpur University
(September 2007)

Receiver Function Analysis of Broadband Seismic Data from Various Seismic Stations and Modelling the Crustal Structure of Northeast India

Summary

Northeastern India is framed by two nearly perpendicular plate boundary arcs: the Himalayan and the Indo-Burman that strain northeastwards to form a syntaxis. West of this syntaxis immediately south of the Himalayan front, there exist a sediment covered foredeep overlying the deeply bent Indian plate as elsewhere along the arc except that its eastern morphology has been affected by the gentler intra-plate convergence with the Indo-Burman arc. However, the tectonic response of NE India to Indo-Eurasian collision as exhibited by its geomorphic and seismic expressions is significantly different from that of the more western segments.

The goal of this dissertation is to study the seismic characteristics of the lithosphere beneath i) the ~1 km high Archaean Shillong plateau and its northeastern extension in the Mikir Hills, ii) the Himalaya, iii) the intervening plains including the foreland spur of exposed archaeans in the Brhmaputra valley immediately south of the plateau and the more northerly foredeep overlying the downward flexed Indian plate, and iv) the Bengal basin marking the transition to more oceanic type crust.

The first section of this thesis, presents a review of the current state of our knowledge about the NE India, focusing on the structure, origin and current deformation of the region. I then examine the crustal structure of the NE India by joint inversion of receiver functions and surface wave data. One-dimensional velocity models for fifteen stations are presented. The results show that the Indian crust Moho progressively deepens northward beneath the Himalaya and Tibet. The average shear wave speeds in the crust beneath the various seismic stations in northeast India bring out the remarkable unity of the Indian crust (Vs = 3.49 – 3.67 km/s) structure right from the Shillong plateau northward up to the great Himalaya, and lends credence to the interpretation that the entire crust of the Shillong plateau including the lower has been up-thrust along mantle reaching faults, and that the lower crust beneath it is strong. An oceanic type crust most likely underlies a thick pile of Bengal basin sediments with a relatively undisturbed Moho at a depth of ~38 km. The findings are consistent with the hypotheses that the entire Shillong Plateau crust has been uplifted along mantle reaching faults and that its ~1 km high uncompensated topography is maintained dynamically by reversed faults engineered by the India-Eurasian collision. The crustal structure of the NE India is also characterized by the presence of strong seismic anisotropy in the crust and the azimuth of anisotropy is well correlated with the orientation of the geological grain in the region.

In the next section I presented a three dimensional image of the Moho beneath the Shillong Plateau and Mikir Hills by combining the joint inversion results together with the locations of the conversion points (piercing points) of the incoming rays at the Moho discontinuities and the Moho Ps arrival times for each event after removal of the GCARC dependency by using a simple migration technique. The Moho Ps converted phases for sites on the Shillong Plateau yield a crustal thickness of 34-36 km, with a slight thickening to 38-40 km at the NW edge of the plateau, and substantial thickening to 40-42 km below the Brahmaputra Valley. The site in the eastern Mikir Hills close to the Brahmaputra Valley and northeast of the seismically active Kopili lineament shows a crustal thickness of 35 km, characteristic of the plateau suggesting similar fault generated uplift. This, however, raises new questions about the relationship of the northern reverse fault that uplifts the Shillong Plateau and other faults that may be responsible for having similarly uplifted the less elevated Mikir Hills.   .
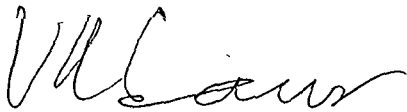
Finally, I investigate the upper mantle and transition zone discontinuities beneath northeastern India using sub-Moho P-to-S converted phases. The findings clearly bring out the existence of the 410 and 660 km discontinuities in the upper mantle of the region and their congruence with the globally averaged depths, with occasional local swerves in the 410 km discontinuity. The near constancy of the mantle transition zone thickness throughout the region, by implication, suggest that no significant anomalous structures exist beneath the region and that it is similar to that as found further north in Tibet. The results affirm that the lithospheric mantle of the region does not have significant thermal anomalies either within or above the transition zone, testifying to the stolid nature of the Indian lithosphere even in the   region of the Indo-Tibetan collision zone.

CERTIFICATE

This is to certify that the thesis entitled "**Receiver Function Analysis of Broadband Seismic Data from Various Seismic Stations and Modelling the Crustal Structure of Northeast India**" submitted to the Tezpur University in the Department of Physics in partial fulfillment for the award of the degree of Doctor of Philosophy in Geophysics is a record of research work carried out by **Mr. Nava Kumar Hazarika** under our joint supervision and guidance.

All helps received by him from various sources have been duly acknowledged.

No part of this thesis has been reproduced elsewhere for award of any other degree.
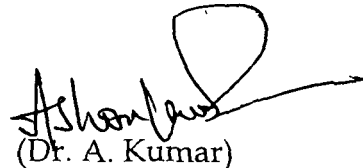
(Prof. V. K. Gaur)

Distinguish Professor

Indian Institute of Astrophysics

Bangalore, India

(Dr. A. Kumar)

Reader

School of Science and Technology

Department of Physics

Tezpur University

Date: 24.08.07

Place: Bangalore, India

Date: 14.09.2007

Place: Napaam, Tezpur

Contents

List of Figures

List of Tables

Acknowledgements

I dedicate this work to my parents and Kuntalika for whom no words can express my heartfelt gratitude None of this work would have been possible without their constant support through the years

Date   *(Nava Kumar Hazarika)*

Chapter 1

Introduction

The persistent northward motion of India resulting into· collision with Eurasia is responsible for the high elevation and seismicity of the Himalaya and the surrounding regions. This process has accommodated an estimated 2000-3000 km of convergence since the late Cretaceous (Molnar and Tapponier, 1977) which continues apace at an annual rate of about 50 mm (Paul et al., 2000). The eastern truncation of the Himalayan plate boundary by the nearly perpendicular Indo-Burman Arc west of India's eastern plate boundary defines the wedged-in geomorphic and tectonic setting of northeastern India which, in consequence, experiences prolific diffused seismicity. The region has been rocked by 2 great earthquakes M ~ 8.7 in the past 110 years. Each of these earthquakes ruptured a fractured fault plane about 200-300 km long. The August 1950 earthquake ruptured the Himalayan segment west of the NE syntaxis on a 60-80 km wide gently plunging plane marked by the upper intact surface of the partly decapitated underthrusting Indian crust. The great Assam earthquake of 1897 however occurred underneath the Shillong plateau and the connection of its rupture plane with the Himalayan plate boundary north of Bhutan still remains to be elucidated. The core contribution of this work includes the results of a re-analysis of broad band seismograms generated during an earlier (Mitra et al., 2005) and more recent experiment designed to further constrain the lithospheric structure beneath northeastern India stretching from Agartala in

the northeastern Bengal Basin through the Shillong Plateau and the Brahmaputra Valley to Tawang in the eastern great Himalaya spanning four, tectonic units, especially the elevated Proterozoic terranes of the Shillong plateau and the Mikir Hills.

Accordingly, this dissertation presents the seismic characteristics of the northeastern Indian lithosphere beneath i) the ~1 km high Precambrian Shillong plateau and its northeastern extension in the Mikir Hills, ii) the eastern Himalaya, iii) the intervening plains including the foreland spur of exposed basement rocks in the Brhmaputra valley immediately north of the plateau and the more northerly foredeep overlying the downward flexed Indian plate, and iv) the Bengal basin marking the transition to a more oceanic 'type crust. The results include: shear wave speed structure, anisotropy and Vp/Vs value of the crust, Moho depth, and upper mantle discontinuities obtained through a rigorous analysis of the seismic data of the region which was largely generated for the purposes of this dissertation.

The shear wave speed structure in the region has been investigated in terms of one dimensional models using joint inversion of receiver functions and surface wave dispersion data calculated for 15 sites from a suite of high quality broad band seismograms selected on the basis of polarization analysis. A move-out correction was applied to all receiver functions using a simple migration technique so as to allow a direct comparison of receiver functions with different ray parameters and a qualitative assessment of azimuthal variations in crustal structure.

The findings provide evidence of i) the virtually intact penetration of the Indian crust into Tibet as far north as Lhasa and the progressive northward deepening of the Indian Moho beneath Himalaya and Tibet, and the existence of an oceanic type structure of the Bengal basin crust. Additionally, they provide a test of the hypothesis that the entire Shillong

Plateau crust has been uplifted along mantle reaching faults engineered by the India-Eurasian collision which continue to support its ~1 km high uncompensated topography (Bilham & England, 2001), and further that the Mikir Hills to the north-northeast of the plateau, in all likelihood, are similarly supported.
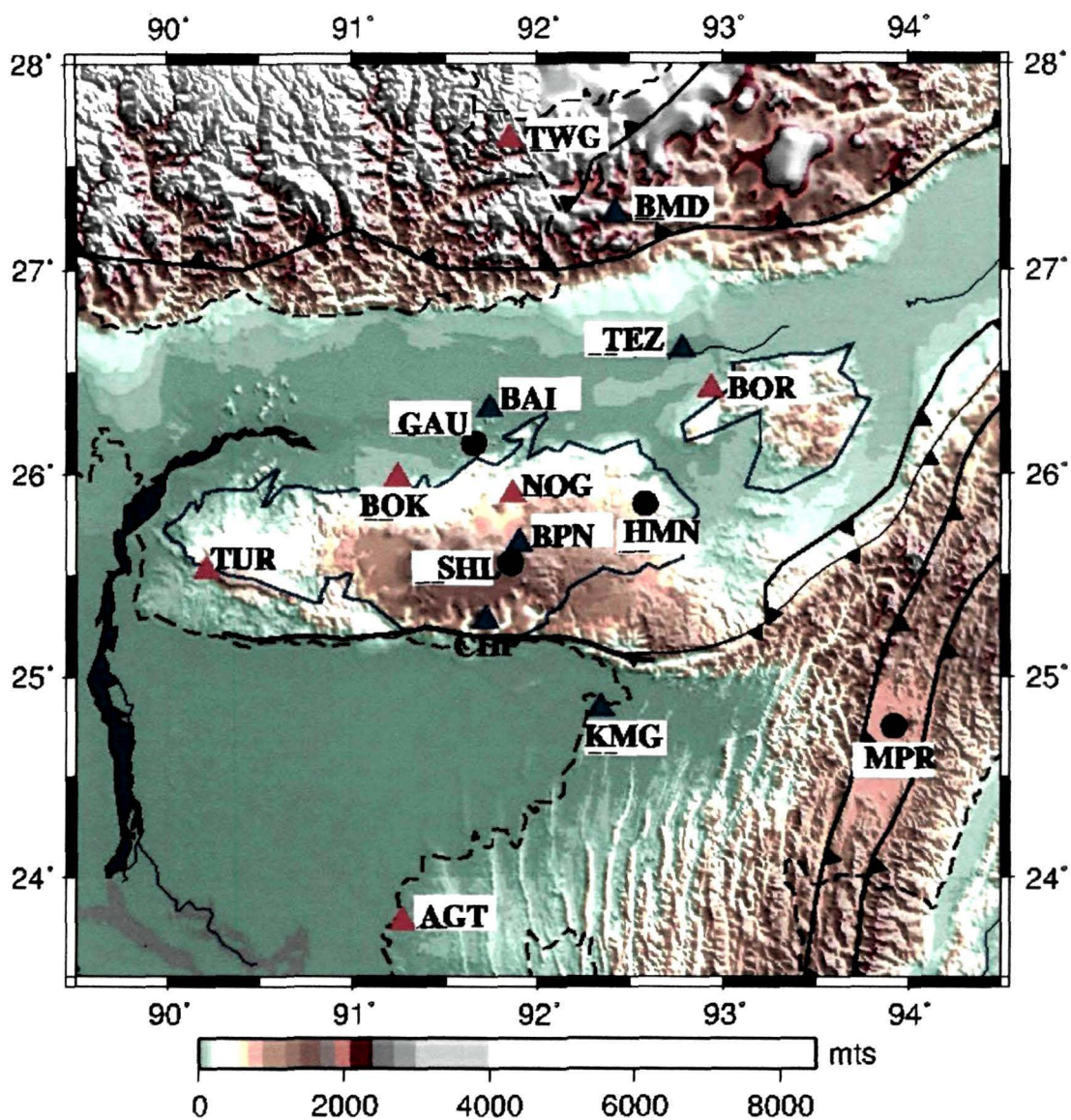
Figure 1.1: Topographic map of Northeastern India showing the main tectonic units of the region and the location of broadband seismic stations. Blue triangles mark the location of broadband seismic stations set up by Mitra et al. (2005), red triangles by Mitra and the present author, and black circles are the DST-sponsored stations operated by other agencies.
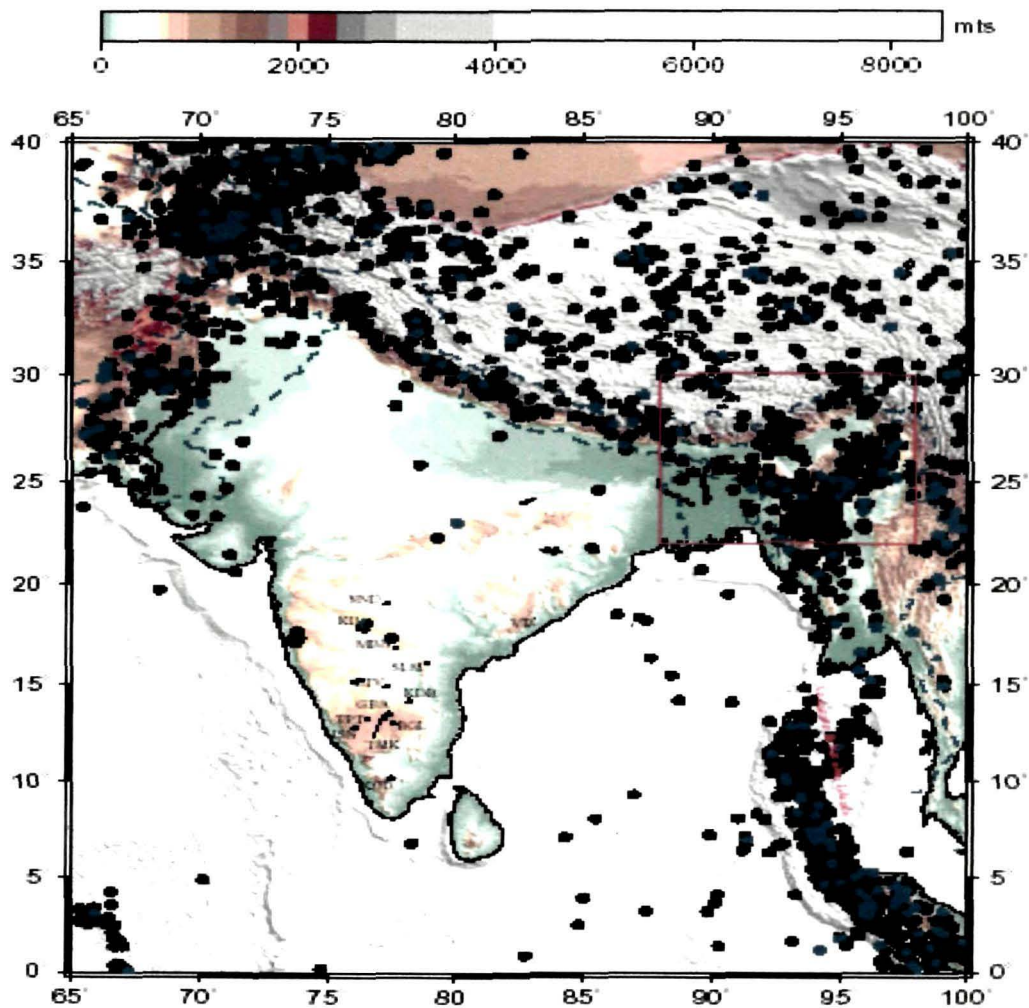
Figure 1.2: Map showing earthquake epicenters along the Himalaya and along India's eastern and western plate boundaries. Earthquakes of magnitude 5.5 and greater are marked in blue and those of lower magnitudes in black.

1.1 Perspective and Statement of the Problem

Northeastern India is framed by two nearly perpendicular plate boundary arcs: the Himalayan and the Indo-Burman that strain northeastwards to form a syntaxis. West of this syntaxis immediately south of the Himalayan

front, there exist a sediment covered foredeep overlying the deeply flexed Indian plate as elsewhere along the arc, except that its eastern morphology has been affected by the gentler intra-plate convergence with the Indo-Burman arc. However, unlike the Himalayan foredeeps and river valleys further west which are bordered by undeformed Precambrian terranes of the Indian shield, this one is bordered by a ~100 km wide and 1 km high plateau of the Indian shield rocks apparently uplifted and sustained by reverse faults, the southern of which also marks a transition to a more oceanic type crust underlain by the Bengal basin.

Furthermore, whilst the tectonic response of the Himalayan plate boundary east of Bhutan, to Indo-Eurasian convergence, conforms to its behaviour along most of the Himalayan arc up to eastern Kashmir, that of its Bhutan segment has been a subject of much speculation since the 1897 Assam earthquake -the only great earthquake of this segment known historically. As this earthquake occurred on a rupture plane over a 150 km south of the Himalayan plate boundary, the mechanism coupling the two has been variously explained. More recently, Bilham and England (2001) modelled triangulation data generated by the Survey of India more than a century ago to demonstrate that the primary fault plane responsible for the 1897 event lay at the northern edge of the Shillong plateau some 100 miles south of Bhutan and most likely penetrated the lower crust. If such were the case, it would have caused only a minor relaxation of strain along the Himalayan front opposite to it. Their analysis further showed that the plateau uplift in the past two to five million years caused by recurrent activity on its northern and southern boundary faults has caused the Indian plate to contract locally. Thus the tectonic response of NE India to Indo-Eurasian collision as exhibited by its geomorphic and seismic expressions is significantly different from that of the more western segments. Understandably, therefore, it has been a subject of much speculative debate that calls for better constrained answers.

Incidentally, the unusual structural feature constituted by the Shillong plateau in the compressive regime of Indo-Eurasian collision and its deeper (greater than ~20 km) seismic activity also constitutes a potentially revealing testing ground for discriminating between hypotheses formulated to describe the lower crust rheology. Thus, the earlier determined sub-crustal focal depths of earthquakes (Chen & Molnar, 1990) beneath the plateau determined on the basis of the then estimated wave speeds had led to an hitherto established belief that the lower continental crust is weak compared with the subjacent mantle owing to the opposite effects on the strength of the material with depth, of increasing temperature on the one hand and of the transition from quartz to olivine rheology, on the other. Receiver functions provide a more reliable means of estimating the crustal S-wave speed structure making it possible to relocate these earthquakes more accurately. Furthermore, they may be used to test the hypothesis whether the lower crust beneath the uplifted plateau is weaker than the subjacent mantle by determining whether its thickness is equal or less compared with that beneath the adjoining Brahmaputra whereunder the Precambrian basement lies no deeper than ~150 meters.

These questions provided the basic motivation for designing the course of investigations whose theoretical foundations, methodologies, data source, analysis and results constitute the subject matter of this dissertation.
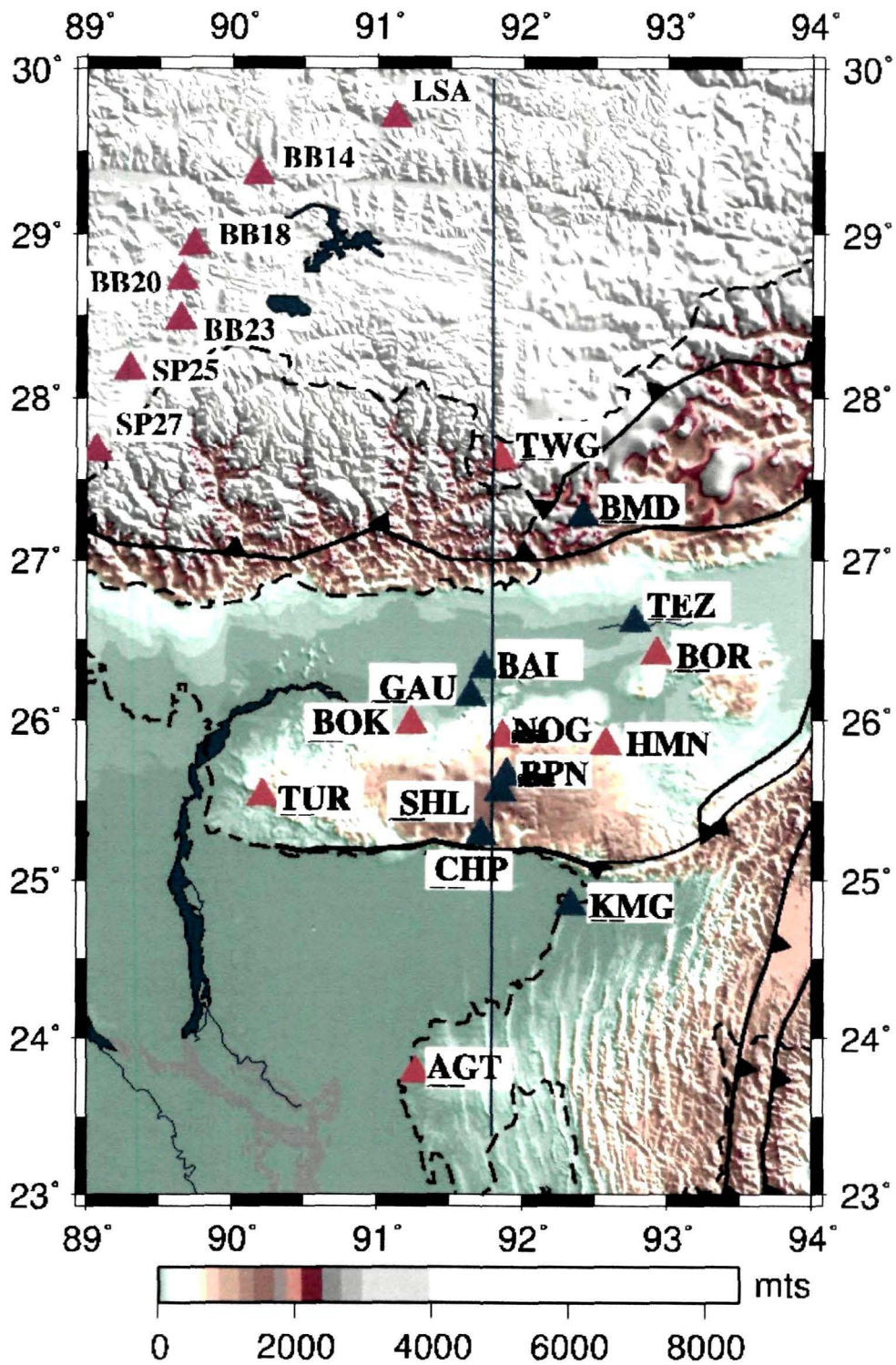
Figure 1.3: Map of Northeastern India and southern Tibet showing the N-S profile stretching from Bengal Basin to the Great Himalayas and the location of broadband seismic stations: blue and purple (the INDEPTH II stations) triangles mark the site for which receiver functions were calculated by Mitra et al. (2005); red triangles denote sites since added where additional data were generated for the present work.

1.2 The Bengal Basin

The Bengal Basin, which includes the world's largest delta, is a composite basin with a varied tectonic history. The dynamic nature of the Bengal Basin can be attributed to the interaction of the three tectonic plates: the Indian Plate, the Tibetan Plate and the Burmese Plate, its development begins in the late Cretaceous (about 127Ma) time when the Indian plate was separated from Antarctica (Sclater and Fisher, 1974). The basin is mostly covered by recent alluvium underlying by a complete sequence of Tertiary sediments, thickening eastward to ~20 km as revealed by geophysical surveys and deep drilling in the region (Das Gupta and Biswas, 2000; Shamsuddin & Abdullah, 1997). The Sylhet trough is a sub-basin of the Bengal Basin, which is characterized by a large, closed, negative gravity anomaly as low as -84 mgal (Ali and Raghava, 1985) and has minimal topography. The Basin is bounded to the north by the Shillong Plateau, which exposes the basement complex of Archean gneisses, greenstones and late Proterozoic granites. To the east of the Bengal Basin, the Indo-Burman fold and thrust belt actively overthrusts the Indian continental basement and its Palaeogene-Neogene cover along a stack of imbricate thrusts whose continued activity creates both shallow and moderate-depth earthquakes in the region (Chen and Molnar 1990; Hallet and Molnar 2001).
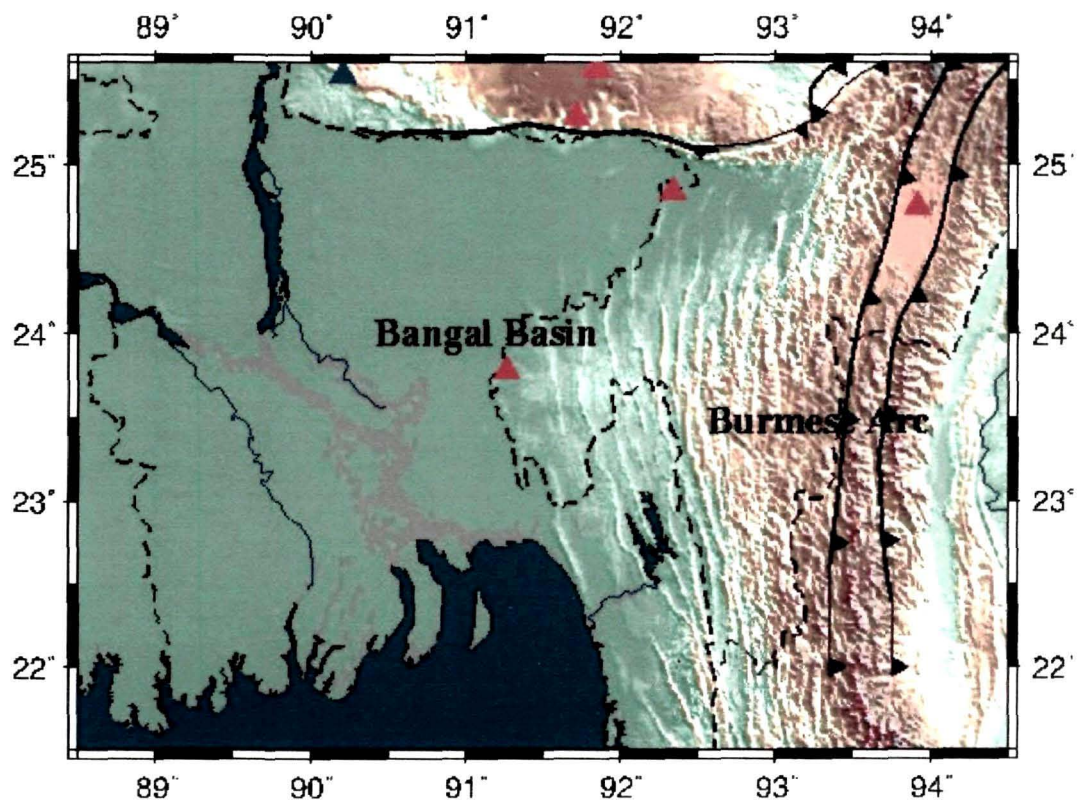
Figure 1.4: Map of the Bengal Basin bounded by the Burmese Arc and the Shillong Plateau on its east and north.

1.3 The Shillong Plateau and the Mikir Hills

The most prominent structural features of Northeastern India south of the Himalaya is the elevated blocks of Archean-Proterozoic basement exposed in the Shillong Plateau and its northeastern extension of Mikir Hills. The Shillong Plateau is bound on the south by the steep north-dipping Dauki fault which is a geomorphic feature of precipitous relief and delimits the northern limits of the Cretaceous age (~120 Ma) Sylhet flood basalts extruded across the region during the break-up of India from Antarctica. This fault is thus required to have predated the India-Eurasian collision although its role before that time must remain highly speculative. At the southeastern margin of the plateau, the Dauki fault merges with the northeastward striking Haflong-Disang thrust continuing into the schuppen

belt of Naga thrusts. Together, these bound the Shillong plateau on the south and the Mikir Hills on the east. On the basis of seismic depth estimates of the top of the sylhet limestone underlying the traps, in the Sylhet trough south of the Dauki fault, Hiller (1998) estimated that the Shillong Plateau has been uplifted by ~15 km along the Dauki fault, most likely since the India-Eurasia collision. Bilham and England (2001) inferred the existence of a buried high-angled reverse fault (the Oldham fault) along the northern margin of the plateau to account for variation in the geodetic data generated over the plateau during the years straddling the 1897 earthquake that had caused it to be uplifted by 11m. This fault is unmapped at the surface and is variously configured by workers relying on space imageries and seismicity patterns. However, since the plateau does not show any dramatic north-south tilt, a northern bounding fault is required to explain the plateau's definite uplift, and can be visualized to have developed after the India-Eurasian collision entered the compressional regime whereafter, movement on the two faults continued to uplift the Shillong Plateau.
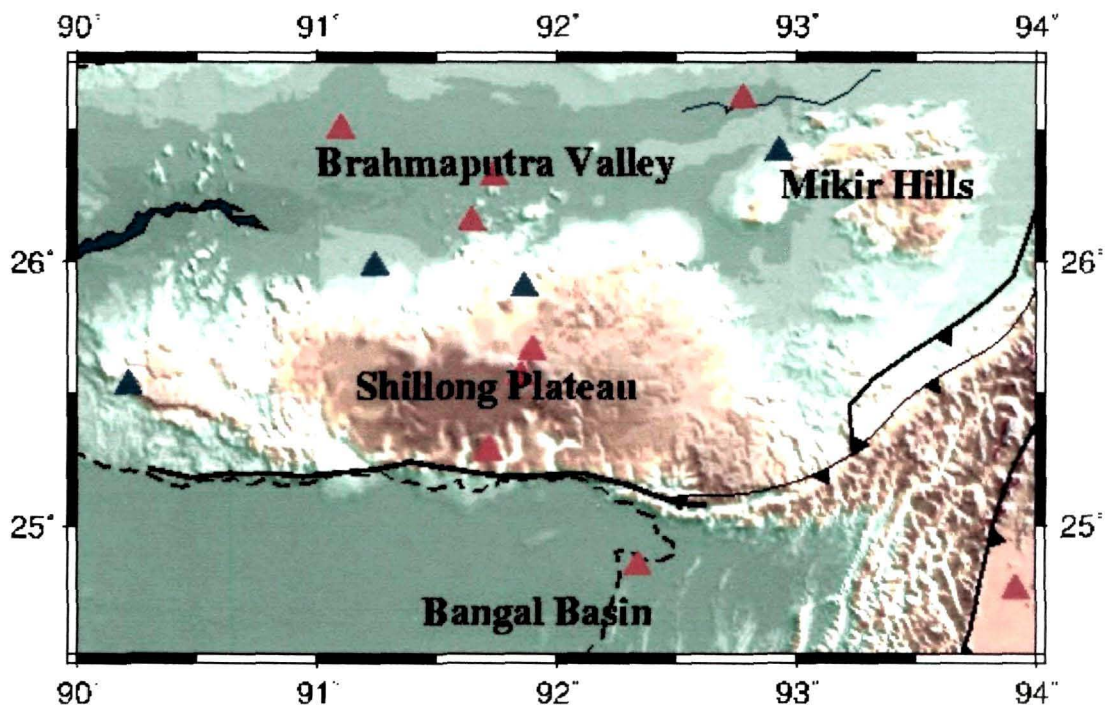
Figure 1.5: Map of the Shillong Plateau and other tectonic features around the Plateau.

1.4 The Brahmaputra Valley

The Brahmaputra valley, ranging in average elevation from 50 to 120 m above msl, represents a unique landscape 800 km long and 130 km wide separated from the comparatively low-lying Surma valley in the east by the Mikir Hills. Its present configuration is the result of uplift and subsidence of the different intricately faulted Precambrian crystalline blocks. Prominent amongst these are the Shillong plateau and the Mikir Hills as well as foreland spurs bordering the lower river valley, whilst a buried horst-graben structure beneath the Brahmaputra river has been mapped by geophysical surveys. On the east, the valley is bound by the Naga-Patkai ranges that developed during the Tertiary geotectonic cycle. North of the valley lies the Himalayan foredeep, the basement being covered by gently dipping Tertiary sediments and recent alluvium that increase in thickness to 4-5 km along the northern Himalayan front. Nandy and Das Gupta (1986) used satellite images to identify a number of buried lineaments beneath the alluvium in the Brahmaputra Valley. Prominent among these are an east-west striking 'Brahmaputra fault ' along the northern edge of the Shillong Plateau, almost paralleling the river, and the north-northwest trending Kopili river lineament that divides the Shillong Plateau from the Mikir Hills.
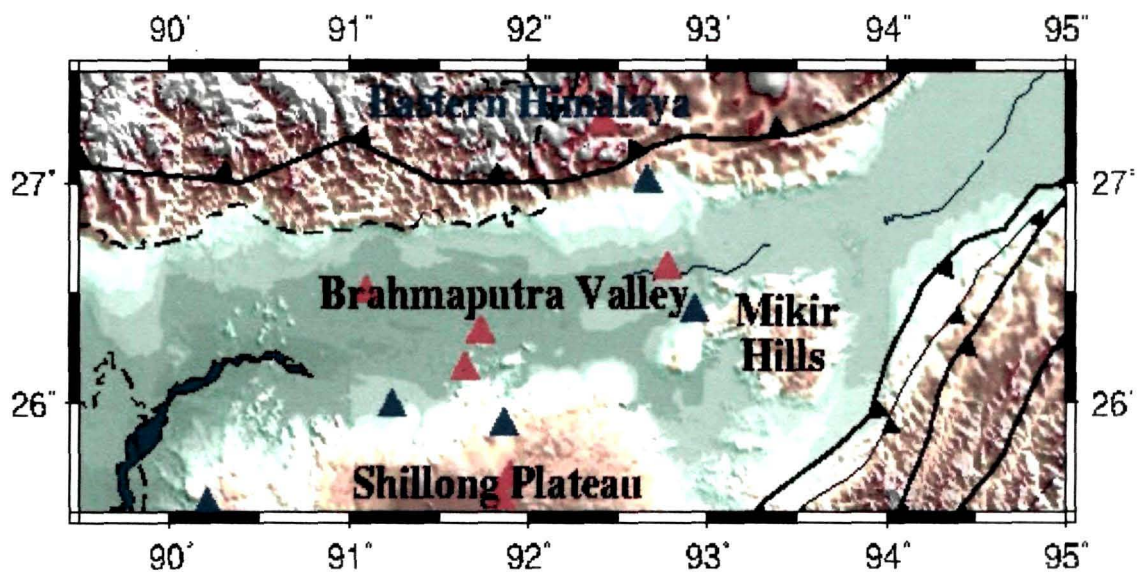
Figure 1.6: Map of the Brahmaputra Valley with the Shillong Plateau and the Mikir Hills, merging northward with the Himalayan foredeep that adjoin the Eastern Himalaya.

1.5 Eastern Himalaya

The most spectacular tectonic feature of the NE Indian region is the Eastern Himalaya, which is formed in response to the early Eocene India-Asia collision. It is comprised of a stack of east-west striking thrust sheets composed of crystalline rocks of the great Himalaya and the meta-sedimentary Lesser Himalaya separated by the Pan-Himalayan Main Central Thrust (MCT). The Lesser Himalaya composed largely of moderate to low grade metamorphic rocks of the Proterozoic era, overthrust the Tertiary foreland sediments along the Main Boundary Thrust (MBT) - a process which continues to the present day in response to the persistent northward penetration of the Indian plate into Tibet. However, the exposed width of the low grade pre-Tertiary metamorphics and the Teriary Siwalik rocks present in the Eastern Himalayas is quite narrow along this belt, because of the greater southward advance of the crystallines, and both the

MCT and MBT have generally steep northerly dips. Eastern Himalaya are distinguished from the Himalayan belt to its west, by the inclusion of... narrow silvers of the Gondwanas as well as marine early-mid Eocene and early Miocene sediments close to and beneath the MBT (Acharyya et al., 1987; Acharyya, 1994). Among the main tectonic features present in the Eastern Himalayas, the Main Boundary Thrust has been geologically mapped all along the Himalaya, and its present activity is testified by both well-constrained earthquake focal mechanisms (Baranowski et al., 1984; Ni and Barazangi, 1984; Molnar and Pandey, 1989; Holt et al., 1991) and GPS Geodesy (Bilham et al., 1997).
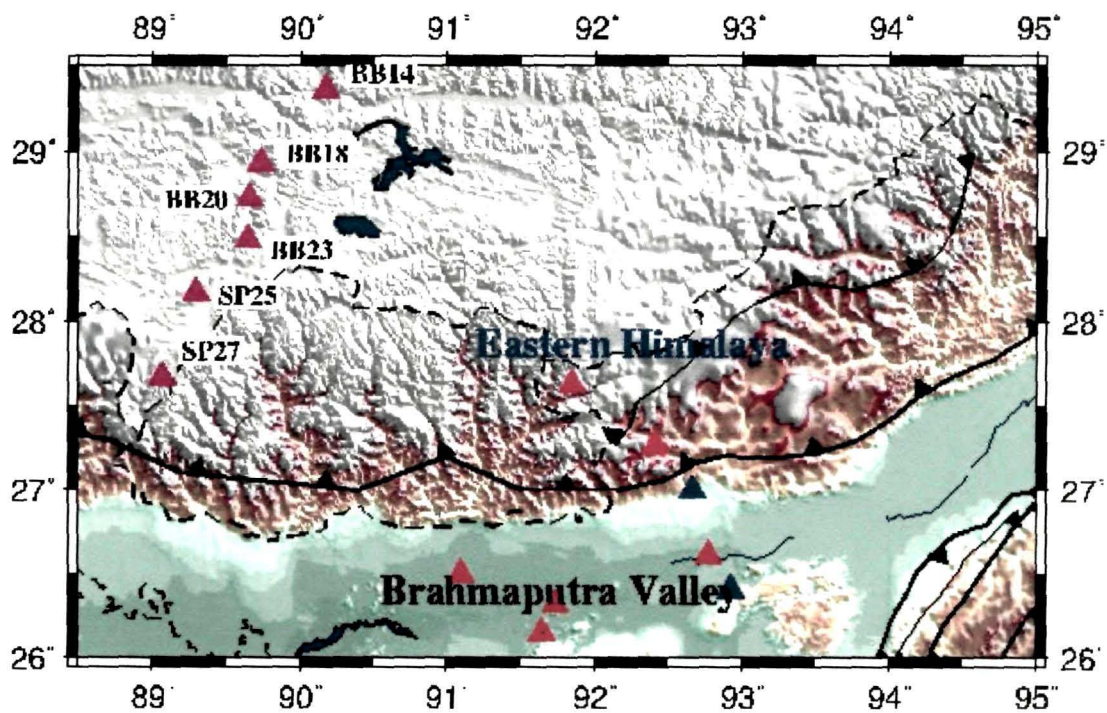
Figure 1.7: Topographic map of the Eastern Himalaya and Tibet. Its southern limit is marked by the Himalayan foredeep and the Brahmaptra Valley

1.6 Outline of the Thesis

This thesis presents new results on the seismic characteristics of the various tectonic elements of northeastern India: shear wave speed structure, seismic anisotropy and Vp/Vs values of the crust, Moho depths and the upper mantle discontinuities.

This Chapter presents an introduction and scope of the problem addressed in this dissertation whilst their theoretical foundations are described in Chapter 2. Chapter 3 deals with the analytical approaches and procedures used for analysis. Polarization analysis of the emergent teleseismic P waves used for selection of uncluttered seismic records ensured a stringent condition on data quality. Chapter 4 presents results of joint inversion of Receiver Functions together with Surface wave dispersion data in terms of the crustal shear wave speed structure underneath 15 sites in the region along a 600 km long N-S profile from Bengal basin to the great Himalaya, whilst chapter 5 provides a 3-dimensional image of the Moho beneath the Shillong Plateau and the Mikir Hills. Chapter 6 contains a study of the upper mantle phases recorded beneath the various sites in NE India using Ps phases. The concluding chapter summarizes the main results presented in this thesis, followed by a discussion of their significance and implications.

Meanwhile, achievements of much tighter constraints on these quantities than obtained here would remain a continuing research goal.

Chapter 2

Theoretical Framework

Theoretical foundations of the analytical methods used in this dissertation rest on the theory of elasticity and wave physics in material media with appropriate limiting and boundary conditions. Infinitesimal strain theory and generalized Hooke's law relating strains to internal stresses in isotropic homogeneous materials are valid approximations for the earth because of small displacements generally, and the random orientation of rock forming crystals which have the effect of statistically homogenizing heterogeneous materials over the dimensions (tens of meters) of a wavelength. When plugged in the equation for conservation of momentum, these stress-strain relations lead to the basic dynamical equation of elasticity. The latter when applied to unbounded media has two transient solutions: a scalar and a vector wave, implying that energy unleashed by any mechanical instability in such a medium travels radially outward from the source as longitudinal and shear waves. Solutions of the dynamical equation for inhomogeneous media constrained by the appropriate boundary conditions of continuity of stresses and strains across interfaces of homogeneous volumes of materials, lead to reflected and refracted waves whose respective amplitudes and therefore energies, can be thereby determined. In particular, when applied to the free boundary of a homogeneous medium such as the earth's surface where both the reflected and refracted waves must simultaneously exist and surface tractions must vanish, the SH wave amplitude is doubled whilst the P and SV waves interact to generate the retrograde elliptically polarized Rayleigh waves. When the half space below the free surface is inhomogeneous, the free

surface reflected SH wave combines with those reflected from internal boundaries to produce a trapped SH reverberation that appear at the surface as Love waves which are dispersed. Even the Rayleigh waves suffer dispersion in a vertically inhomogeneous or layered media owing to the appearance of finite scales that cause wavelength dependent interactions. The phase and group velocities of these surface waves (both Love and Rayleigh) are determined by the scale of the inhomogeneities and their elastic parameters can, in turn, be determined from these velocities abstracted from a set of seismograms generated at sites along the wave passage.

When dealing with inhomogeneous media however, λ and μ being functions of position, the dynamical equation (with zero body force) cannot be reduced to a wave equation and a different approach has to be adopted using an approximation of the wave equation. One thus arrives at the 'Ray Equation' (the Eikonal) following wave trajectories which greatly facilitates the tracking of waves through inhomogeneous media although its range of validity is limited to situations where velocity gradients over the dimensions of a seismic wavelength are small. A concise but complete treatment of these basic theoretical formulations is therefore included in the following sections, together with those relating to converted phases at acoustic impedance boundaries, in particular, the shear waves generated at these boundaries in the earth's crust and upper mantle by near vertical incident P waves. The former when abstracted from the more convoluted seismograms, can be inverted to determine the seismic characteristics of the region traversed by these converted waves. Since for short amplitude seismic waves the earth behaves like a linear system, these converted shear waves and their multiples Rs(t) appearing at the earth's surface can be regarded as the *convolved* product of the generator P-wave P(t) incident at the base of an earth column and the overlying structure, and therefore as the earth column's response to the P-wave excitation. Theory shows that the generator teleseismic $(30° < \Delta < 90°)$ P waves incident at a steep angle are transmitted without any significant

deviation from their original path or diminution in their amplitudes, which allows one to treat them as representing the vertical ground motion recorded at the surface. The converted shear wave time series Rs(t), on the other hand, are quite feeble compared with the much larger amplitude P-wave component appearing on broadband horizontal component seismograms. Fortunately, however, they can be neatly isolated by deconvolving the vertical component seismogram from its radial and transverse components, in turn, vectorially reconstituted from the north and the east component seismograms. The resulting time series Rs(t) contain the horizontal component of the generator P-wave followed by the converted shear wave phases and their multiples, and largely represent the properties of materials immediately beneath the receiver, aptly called a Receiver Function. A grid search method enables testing of the coherence of these multiply generated shear wave phases to constrain the depth of the seismic discontinuity and the average Vp/Vs value, whilst its inversion in terms of the shear wave speeds in a stack of equal thickness layers, yields the shear wave structure of the underlying earth. Accordingly, the topics covered in this chapter, include: the elastodynamic equation and the Eikonal (wave to rays), partitioning of energy at seismic discontinuities, converted phases, receiver functions, surface waves, inverse theory and seismic anisotropy.

2.1 Deformation of Elastic Media

Physical bodies when subjected to forces may suffer displacement or deformation. The latter involve changes in volume, shape or both due to rearrangement of contiguous matter. Response of macroscopic bodies to forces can be adequately analyzed using Newton's laws of classical mechanics for a particle by treating a material body as a continuous distribution of particles - a continuum - in which the point position of the particle is abstracted from an infinitesimal surrounding volume (dv) as this volume

approaches zero and its mass as concentration of the mass (ρ dv) contained in this volume element as it shrinks to a point. Mathematically, this is realized with the help of the peaked Dirac Delta function $\delta(R - R_0)$ defined as follows:

δ(R - Ro) = 1 for R = Ro, and is zero for all other values of R

$$\int \delta(R - R_0)dR = 1; \qquad \int f(R)\delta(R - R_0)dR = f(R_0)$$

Thus, applying Newton's laws to a continuous distribution of infinitesimal volumes dv, we can analyze the behaviour of material bodies when subjected to external forces.

In an undeformed body, the arrangements of constituent molecules are determined by the state of its thermal equilibrium. Any portion of such a body at constant temperature, is therefore in mechanical equilibrium and the sum of all forces therein is zero. When deformed, the equilibrium molecular arrangement within the body is altered requiring the creation of *internal forces* to return the body to equilibrium. These internal forces are sustained by *interaction between molecules*, as distinct from *'molecular forces'* whose range of action extends only to molecular distances and is therefore of no consequence to macroscopic behaviour. For analyzing elastic behaviour of bodies, therefore, we may regard 'internal forces' as *'neighbourhood acting forces'* impressed by any point (infinitesimal of volume) on to its neighbourhood points only or vice versa. Therefore, forces acting on any part of the body due to a surrounding part act only at their interface, and, in general, would vary with the orientation of the neighbourhood.

For proceeding further to analyze the response of material bodies to forces using Newton's laws of mechanics, we need a quantitatively complete description of both Forces acting over an infinitesimal volume representing a

point and the resulting **Deformation** in terms of relative displacements of neighbourhood points.

2.1.1 Quantitative Measure of Deformation

We first seek a quantitative description of Deformation of an infinitesimal volume of material centred at a point ($P(X) = i_k x_k$) which, in general, may have suffered a displacement (U(X)= $i_k du_k$) accompanied by an altered structure of its neighbourhood. Accordingly, we enquire as to what happens to the neighbourhoods of the point X in this process, and more specifically, to the variously directed infinitesimal $dX (= i_k dx_k)$ vectors originally centred at X. We answer this by drawing upon our abstraction of the continuum, to express the displacement $U(X + dX)$ at a neighbouring point $(X + dX)$ as a Taylor's expansion about $U(X)$ retaining only the first term in view of the infinitesimal value of $|dX|$. Thus, writing the kth component of $U(X + dX)$, that is the displacement of the tip of the vector dX as

$$u_k(X + dX) = u_k(X) + \sum_l \left(\frac{\partial u_k}{\partial x_l} \right) dx_l \, , \qquad (2.1)$$

the deformation dX' suffered by dX can be written in terms of the strain components: S_k

$$dx_k' = S_k = u_k(X + dX) - u_k(X) = \sum_l \left(\frac{\partial u_k}{\partial x_l} \right) dx_l \qquad (2.2)$$

Expressed in a matrix form, the strain S, suffered by the vector dX appears as the result of an operation on dX by the matrix E

Or, $S = EdX$ (2.3)

with the matrix E itself decomposed as a sum of its 3 irreducible (Arfken, 2005) components ($E = h + c + e$), h behaving as a scalar, c as a vector (= Curl U), and e as a symmetrical tensor. Thus, it is easily seen that

$$h = \begin{bmatrix} \varepsilon & 0 & 0 \\ 0 & \varepsilon & 0 \\ 0 & 0 & \varepsilon \end{bmatrix}, \text{ where } \varepsilon = \frac{1}{3}\left[\frac{\partial u_1}{\partial x_1} + \frac{\partial u_2}{\partial x_2} + \frac{\partial u_3}{\partial x_3}\right]$$

$$c = \begin{bmatrix} 0 & \frac{1}{2}\left(\frac{\partial u_1}{\partial x_2} - \frac{\partial u_2}{\partial x_1}\right) & \frac{1}{2}\left(\frac{\partial u_1}{\partial x_3} - \frac{\partial u_3}{\partial x_1}\right) \\ \frac{1}{2}\left(\frac{\partial u_2}{\partial x_1} - \frac{\partial u_1}{\partial x_2}\right) & 0 & \frac{1}{2}\left(\frac{\partial u_2}{\partial x_3} - \frac{\partial u_3}{\partial x_2}\right) \\ \frac{1}{2}\left(\frac{\partial u_3}{\partial x_1} - \frac{\partial u_1}{\partial x_3}\right) & \frac{1}{2}\left(\frac{\partial u_3}{\partial x_2} - \frac{\partial u_2}{\partial x_3}\right) & 0 \end{bmatrix}$$

$$e = \begin{bmatrix} \frac{\partial u_1}{\partial x_1} - \varepsilon & \frac{1}{2}\left(\frac{\partial u_1}{\partial x_2} + \frac{\partial u_2}{\partial x_1}\right) & \frac{1}{2}\left(\frac{\partial u_1}{\partial x_3} + \frac{\partial u_3}{\partial x_1}\right) \\ \frac{1}{2}\left(\frac{\partial u_2}{\partial x_1} + \frac{\partial u_1}{\partial x_2}\right) & \frac{\partial u_2}{\partial x_2} - \varepsilon & \frac{1}{2}\left(\frac{\partial u_2}{\partial x_3} + \frac{\partial u_3}{\partial x_2}\right) \\ \frac{1}{2}\left(\frac{\partial u_3}{\partial x_1} + \frac{\partial u_1}{\partial x_3}\right) & \frac{1}{2}\left(\frac{\partial u_3}{\partial x_2} + \frac{\partial u_2}{\partial x_3}\right) & \frac{\partial u_3}{\partial x_3} - \varepsilon \end{bmatrix}$$

The strain S suffered by dX, thus turns out to be the sum of the operations on dX by the matrices h, c and e. The first of these leading to a uniform extension/contraction of all three components of dX does not therefore alter the shape of the neighbourhood around $P(X)$, but only hydrostatic changes in volume, the cubical dilatation being given by the trace of h,

$$h_{trace} = \left[\frac{\delta V}{V}\right] = \theta = \left[\frac{\partial u_1}{\partial x_1} + \frac{\partial u_2}{\partial x_2} + \frac{\partial u_3}{\partial x_3}\right] \tag{2.4}$$

The second operating on dX transforms it to $\frac{1}{2}[CurlU \times dX]$ which signifies rigid body rotation of the vector dX by an amount equal to $\frac{1}{2}[(CurlU)]$ about the vector $CurlU$. The symmetric matrix e with zero trace, alone is responsible for the non-hydrostatic shear deformation of the infinitesimal neighbourhood of $P(X)$ and is referred to as the deviatoric components of strain e_{kl} which

happens to be symmetrical: $e_{kl} = e_{lk}$ The deviatoric strain suffered by dX can thus be written as:

$$S_k = \sum_l e_{kl} dx_l \qquad (2.5)$$

where,

$$e_{kl} = \left[\frac{1}{2} \left\{ \left(\frac{\partial u_k}{\partial x_l} + \frac{\partial u_l}{\partial x_k} \right) \right\} - \varepsilon \delta_{kl} \right] \qquad (2.6)$$

and δ represents the Kronecker delta. It may be noted that the deviatoric strain tensor matrix **e** like all symmetric matrices can be diagonalized by transformation to an appropriate set of orthogonal axes. These new axes then represent directions along which the strain at P(X) is entirely longitudinal and are therefore called the Principal strains.

2.2. Quantitative Description of Force

It will be recalled that the equilibrium molecular arrangement of a body is altered when it suffers deformation, raising in consequence internal forces to create a new equilibrium state, and that these forces are 'near action' forces impressed by a point (infinitesimal volume element) only on the neighbouring points at their interfaces. To sharpen our focus on a mathematical description of the total force on a body, we isolate some part of it defined by an imaginary surface that separates it from the surrounding matter. The total force on this isolated volume of material is the sum of all the forces on all the infinitesimal volume elements contained within this isolated volume expressible as the volume integral Fdv where F is the force density. In equilibrium, the forces which these various infinitesimal volume elements impress on their neighbouring elements as contact forces of action and reaction have a zero resultant, leaving only those acting at the imaginary surface of the isolated volume, exerted upon it by the parts that surround it.

The total force on this isolated portion of the body is thus the sum of forces exerted on all of its surface elements by its neighbours.

We further recall the well known vector relation that the volume integral of a scalar quantity which can be expressed as the divergence of a vector, can be transformed into an integral of the surface density of that vector over the surface that encloses this volume:

$$\int (\nabla . A) dv = \int A.dS \qquad\qquad (2.7)$$

Making use of the above equivalence, we can express the total force Fdv on any volume element in terms of the surface density of forces (Force per unit area) or 'tractions' impressed on the various elements of the surface that bounds it. However, since the integrand of the volume integral in this case is a vector with 3 scalar components $\left(f_k\ k = 1,2,3\right)$ each one of which can be separately transformed into 3 surface integrals, we would require that each scalar component f_k is the divergence of a corresponding vector T_k. Therefore, for a complete definition of the total force in the elementary volume, we require 3 vectors with components T_{jk}, where the first subscript refers to the three tractions and the second to their respective components. The nine T_{jk} quantities thus distilled for the complete description of the force at a point in the body, are called the **Stress Tensor** or just stress at the point to which the infinitesimal volume shrinks in the limit. Tensors, originating from the word **Tension** whose analysis first led to their formulation, form a much more general class of entities. The total force density $F(= i_k f_k)$ at a point within a body can thus be expressed as the divergence of the stress tensor T:

$$F(X) = -\nabla.T(X) \qquad\qquad (2.8)$$

Or, in terms of their components:

$$f_k = -\nabla.T_{jk} \qquad\qquad (2.9)$$

where the negative sign signifies the convention that positive traction on $\hat{n}$ is

the force exerted by the material on the positive side of the surface vector $\hat{n}$.

The components of T_{jk}, can be written in a matrix form as follows:

$$T_{jk} = \begin{bmatrix} T_{11} & T_{12} & T_{13} \\ T_{21} & T_{22} & T_{23} \\ T_{31} & T_{32} & T_{33} \end{bmatrix}$$ (2.10)

An intuitively appealing approach to visualizing the description of stress at a point within a given body is to consider dividing the body by an imaginary surface passing through the point under consideration. Each part of this divided body acts on the other at that point exerting equal and opposite forces. But, we describe the force vector at a point on one of the two divided portions under consideration in terms of its surface density or *traction*: $Lim_{s \to 0}[F/S]$ where F is the force vector acting over an infinitesimal contact area S around the point of the imaginary surface. However, the traction at the point, for any given configuration of applied forces, would depend on the orientation of the imaginary dividing surface through the point and would therefore furnish an incomplete description of the force acting thereon. This arbitrariness can, however, be removed by incorporating three traction vectors T_k on three imaginary orthogonal planes through the point, thereby involving nine scalar quantities. These nine components of the stress tensor, T_{jk} at a point completely describe the force acting at that point because they

can be used to calculate the traction across any arbitrarily oriented surface $\hat{n}$ through the point. We shall follow the convention that the first subscript of T_{jk} denotes the planes: x_1, x_2, x_3, and the second denotes the components along the respective axes.

When a body is made of constituent volume elements that are susceptible to additional forces because of the presence of some specific fields e.g., masses in a gravitational field [e.g. $\rho g dv$] or charged and magnetically polarized particles in an electromagnetic field, there would appear these 'body' forces fdv that must be added to the stresses described above.

For equilibrium, $(F/dv = F)$ must balance all other forces. In general, therefore

$$F + f = \rho\left(\frac{\partial^2 U}{\partial t^2}\right)$$ (2.11)

Further, the conditions of i) rotational equilibrium of the infinitesimal volume about the various axes can be shown to require that the stress tensor be symmetrical, that is,

$$T_{jk} = T_{kj}$$ (2.12)

and, ii) the equilibrium of an elementary tetrahedron bounded by the three axial planes and an arbitrarily oriented surface $\hat{n}$ require that

$$T_{nj} = \sum_k T_{n_k n_k}$$ (2.13)

which enables one to calculate the jth component of the traction at a point across an arbitrary surface $\hat{n}$, given the stress tensor T_{jk} at that point.

Like the strain tensor, the symmetric stress tensor $(T_{ij} = T_{ji})$ can be decomposed into its irreducible parts,

$$\begin{bmatrix} T_{11} & T_{12} & T_{13} \\ T_{21} & T_{22} & T_{23} \\ T_{31} & T_{32} & T_{33} \end{bmatrix} = [p] + [T^{shear}]$$ (2.14)

where $p = \frac{1}{3}\sum_k T_{kk}$ (2.15)

$$\text{and,}\quad \left[T^{shear}\right]=\begin{bmatrix} T_{11}-\dfrac{1}{3}\sum_{k}T_{kk} & T_{12} & T_{13} \\[2mm] T_{21} & T_{22}-\dfrac{1}{3}\sum_{k}T_{kk} & T_{23} \\[2mm] T_{31} & T_{32} & T_{33}-\dfrac{1}{3}\sum_{k}T_{kk} \end{bmatrix}\qquad (2.16)$$

The deviatoric stress tensor $\left[T^{shear}\right]$, being symmetric can be diagonalized like the deviatoric strain components to yield the Principal (normal) stresses at a point.

2.3 Elastic Energy and Relationship between Stress and Strain

The relationship between stress and strain, called the constitutive relation, is an important characteristic of the medium and can be elucidated from thermodynamic arguments. Consider an elastic body in equilibrium that suffers an infinitesimal strain characterized by the displacement of its constituent points by $\delta U(R)$. The work δW done by the applied stresses against the elastic restoring forces in the course of this infinitesimal strain is:

$$\delta W = \int (f\,\delta U)\,dv + \int (T.\delta U)\,ds \qquad (2.17)$$

Since $(T_n.\delta u)ds = \delta u_1\{T_{11}n_1 + T_{21}n_2 + T_{31}n_3\}ds$

$$+ \delta u_2\{T_{12}n_1 + T_{22}n_2 + T_{32}n_3\}ds \qquad 2.18)$$

$$+ \delta u_3\{T_{13}n_1 + T_{23}n_2 + T_{33}n_3\}ds = \delta u_i\{T_{ki}n_k\}ds = (\delta u_j T_{kj}).\,dS$$

$$\therefore \int (T.\delta U)\,ds = \int (T_k.\delta U).dS = \int \nabla.(T\,\delta U)\,dv \qquad (2.19)$$

But $\nabla.(T_{k1}\delta u_1) = \delta u_1\nabla.T_{k1} + T_{k1}.\nabla u_1$

$$\therefore \delta W/dt = d/dt \int [(f_p + \nabla.T_{kp})\delta u_p]\,dv + d/dt \int [T_{k1}.\nabla\delta u_1 + T_{k2}.\nabla\delta u_2 + T_{k3}.\nabla\delta u_3]\,dv \qquad (2.20)$$

According to the first law of thermodynamics, the internal energy may change with deformation and the energy balance for the work done on the body is:

rate of doing mechanical work (δw) + rate of heating δQ

$\qquad$ = rate of increase of both kinetic (δE$_k$) and $\hfill$ (2.21)

internal energies (δE$_i$)

Where δE_i is the resulting change in internal energy. Substituting for δW from (2.20) in the above equation and noting that, in view of (2.11), the first integral on its RHS equals $(1/2)(d/dt)[2\rho(\partial U/\partial t)(\partial\{\delta U\}/dt | = d/dt(\delta E_k)$, and that the second is the product $T_{jk}\delta e_{jk}$ of the strain and the corresponding strain tensor, we obtain using (2.21),

$$\delta E_i = \delta Q + T_{jl}\delta e_{jl} \qquad (2.22)$$

For adiabatic deformation $\delta Q = 0 = T\delta S$ (for reversible processes), and (2.22) reduces to

$$\delta E_i = T_{jl}\delta e_{jl} = dW \text{ if } \delta(\text{kinetic energy}) \text{ is extremey small} \qquad (2.23)$$

The internal energy density, E_i, at any point of the body must depend on the local state of strain.

Or, $\quad E_i = E_i(e_{jl})$, and $\delta E_i = (\partial E_i/\partial e_{jl})\delta e_{jl}$ $\hfill$ (2.24)

Comparing (2.23) and (2.24), we identify E_i as the strain energy function of the strain components that evokes stresses according to $T_{jl} = (\partial E_i/\partial e_{jl})$. When deformations are small, the stress components can be expressed as linear functions of strain (Generalized Hooke's law).

Or, $\quad T_{ij} = C_{ijlm}e_{lm}$ $\hfill$ (2.25)

where C_{ijlm} are called the elastic constants of the medium. The symmetry of e

and T, ensures that $C'_{ijlm} = C'_{jilm} = C'_{ijml} = C'_{jiml}$.

Further, from (2.25) we deduce that

$$\left(\partial T_{jk}/\partial e_{pq}\right) = \left(\partial^2 E_i/\partial e_{jk}\partial e_{pq}\right) = \left(\partial T_{pq}/\partial e_{jk}\right)$$

Or, $C_{jkpq} = C_{pqjk} = C_{pqkj} = C_{qpjk} = C_{qpkj} = C_{kjpq} = C_{kjqp} = C_{jkqp}$ (2.26)

Therefore, the number of elastic constants necessary to specify the relation between stress and strain of any arbitrarily chosen material is reduced to 21. Rock materials of the earth, generally made up of randomly oriented crystals except where exceptional thermal and stress regimes may orient them preferentially, can be treated as being isotropic on the scale of a seismic wave length of a few kilometers. This condition drastically reduces the number of elastic constants to just two. For, the most general isotropic 4th order tensor such as $C_{jk\,pq}$ having the (2.26) symmetries, can be expressed (Jeffereys) as:

$$C_{jk\,pq} = \lambda\delta_{ij}\delta_{kl} + \mu\left(\delta_{ik}\delta_{jl} + \delta_{il}\delta_{jk}\right)$$ (2.27)

So that only the $C_{ii\,ii}$, $C_{ii\,kk}$ and $C_{jk\,jk}$ terms survive and can be expressed in terms of just two elastic constants λ nd μ, called the Lame's constants.

$$C_{ij,ij} = \left(\lambda + 2\mu\right); \quad C_{ii\,kk} = \lambda \text{ and } C_{jk\,jk} = \mu$$ (2.28)

The stress – strain relations, in turn, are thus distilled into

$$T_{jk} = \lambda\theta\delta_{jk} + 2\mu e_{jk}$$ (2.29)

Where

$$\theta = e_{11} + e_{22} + e_{33}$$ (2.30)

In turn, the various physically evocative elastic modulii, namely the Young's modulus (Y), rigidity (μ), incompressibility (k), and Poison's ratio (σ) can be expressed in terms of λ and μ or in terms of each other. For example, the Poisson's ratio can be written as:

$$\sigma = [\lambda/2(\lambda + \mu)] = [\lambda/(3k - \lambda)] = [(3k - 2\mu)/2(3k + \mu)] = [(3k - Y)/6k] \quad (2.31)$$

(2.23) and (2.25) also enable one to show that the work done by stresses T_{ij} in developing a state of strain equal to e_{ij} is equal to $\frac{1}{2}(T_{ij} e_{ij})$.

2.4 The Dynamic equation

Using the constitutive equations (2.29), we can now write Newton's equation for the conservation of momentum

$$\rho U = F + (\lambda + 2\mu)\nabla(\nabla \cdot U) - \mu \nabla \times \nabla \times U \quad (2.32)$$

(2.32) is the full equation of motion for an elastic medium from which we can deduce solutions to various specific problems of motion and deformation. For example, by replacing F in the above equation by a concentrated point force at R_0 directed along $\hat{a}$ $\left[F = |F|\hat{a}\,\delta(R - R_0) \right]$ and ignoring inertial forces, we obtain the fundamental Kelvin solution which is the key to constructing solutions of a wide variety of problems involving a complex set of body forces. Another most important solution to the basic problem of elastic wave propagation is obtained by treating the body forces to be zero and seeking transient solutions of the resulting equation by considering the most general displacement vector composed of a conservative (gradient of a scalar) and a

solenoidal (curl of a vector) vector $U(X) = (\nabla\phi + \nabla \times \psi)$. Thus both ϕ and ψ, are found to satisfy the wave equation

$$\nabla^2 \chi = \left(1/V_\chi\right)^2 \left[\partial^2 \chi/\partial t^2\right] \tag{2.33}$$

where

$$V^2{}_\phi = (\lambda + 2\mu)/\rho \text{ and } V^{\prime}{}_\psi = \mu/\rho \tag{2.34}$$

Solutions to the above wave equation can be determined by separation of the three spaces and the time coordinates. Thus, writing $\chi = [X(x)Y(y)Z(z)T(t)]$ in the rectangular coordinate system and its substitution in (2.33), one obtains the following set of 4 coupled equations:

$$\ddot{X} = k_1{}^2\Delta X; \ \ddot{Y} = k_2{}^2\Delta Y; \ \ddot{Z} = k_3{}^2\Delta Z; \ \ddot{T} = \omega^2\Delta T$$

Where, $\left|k_1{}^2 + k_2{}^2 + k_3{}^2\right| = (\omega^2/\left(V_\chi{}'\right)) = K^2$, and k_q are the cartesian components of the wave number vector K which defines the propagation direction of the wave. The solution of (2.33) can now be written in a straightforward manner as:

$$\chi = A\exp[\pm j(\omega t - K.X)] \tag{2.35}$$

where χ will be recognized as a forward travelling wave whose form is reproduced at a subsequent position $(X + dX).\hat{k}$ and time $(t + dt)$ provided it moves with a velocity $(dX/dt) = (\omega/|K|)$. A signifies the amplitude of χ and the quantity $(\omega t \pm K.X)$ describes its phase with respect to a zero phase reference at $t = 0$. In 3 dimensions as the wave radiates outwards from the source, there would be many points X_i in space whereat the phase $(\omega t \pm K.X_i)$ for any given time t would be the same. The locus of all these equiphase X_i points would be a surface called the *wavefront* $S(X_i)$. We may, therefore write (2.35) in 3 dimensions as:

$$\chi(X_i,t) = A\exp\left[j\left(|K|S(X_i) - \omega t\right)\right] \tag{2.36}$$

where $\hat{k}$ defining the unit vector normal to the wavefront at each point, marks the direction of propagation of that element of the wavefront analogous to the 'ray' in optics. The orientation of the ray at any time is therefore normal to the surface S(t)=constant or along ∇S.

Since the earth is largely a spherically layered medium the Fermat path between an earthquake source and a receiver lies in the plane connecting the two through the center of the earth. Assuming the x_1 axis to lie opposite the back azimuth of an arriving wave and the x_1 axis to be vertical (positive downwards), one could further simplify the above solution to 2 dimensions:

$$\psi(X,t) = A\exp\left[\pm j\left(\omega t \pm k_1 x_1 \pm k_3 x_3\right)\right] \tag{2.37}$$

This corresponds to a plane wave advancing along the vector K, the surface of constant phase ϕ_0 at any given time '$t = 0$', that is the wave front, being given by the plane containing the x_2 axis and the line $[x_3 = [\phi_0 - k_1 x_1]/k_3]$. If we define the angle i between the K vector and the x_3 axis as the angle of incidence of the wave, we obtain

$$k_1 = \omega Sin i / V_r = \omega p \quad \text{and} \quad k_3 = \omega Sin i / V_\chi = \omega \eta_\chi \tag{2.38}$$

where p will be recognized as the reciprocal of the apparent horizontal velocity called the horizontal slowness or the 'ray parameter' and η the vertical slowness. It is often more convenient to write the solution of the wave function in terms of p and η.

Or, for a plane wave incident from below the surface propagating along the positive x_1,

$$\psi(X,t) = A\exp\left[j\omega(px_1 - \eta x_3 - t)\right] \tag{2.39}$$

The ϕ solution of the above equation represents a scalar wave polarized along the direction of propagation $\hat{k}$, and is identified with the longitudinal or the P-wave. The ψ solution, on the other hand, represents a vector shear wave

also traveling along k, but having its displacement components (from

$U = \nabla \times \psi$) perpendicular to k in the $x_1 - x_3$ plane, constituting the SV component. The x_2 component involving purely horizontal displacements which in this case is zero, is called the SH component.

2.5 Short Wave Approximation: The Eikonal Equation

Solutions of the wave equation for any given instant of time yield the surface of constant phase (wavefront) normal at any of its point to the direction of propagation, so that all particle displacements thereon are exactly in step. Wavefronts evoke an intuitive understanding of radiating energy particularly in inhomogeneous media. In analogy with light waves, seismic waves can be shown to approximate as rays (the Eikonal equation) with respect to large-scale heterogeneities in the earth.

For simplicity, we consider the propagation of compressional waves in heterogeneous media. The displacement $u(= \nabla \phi)$ can be expressed in terms of the P-wave scalar potential ϕ as

$$\nabla^2 \phi - \frac{1}{\alpha^2} \frac{\partial^2 \phi}{\partial t^2} = 0 \tag{2.40}$$

where the P-wave velocity, α, is a function of position, $\alpha = \alpha(X) = [\omega / k(X)]$.

We assume a harmonic solution of the form

$$\phi = A(x) e^{-i\omega T(X)} \tag{2.41}$$

where $\omega T(X)$ represents the wave phase $[= (\omega t \pm K.X)]$, and A the local amplitude. Substituting this value of ϕ in the wave equation and dividing out the constant $e^{-i\omega T(X)}$ factor, we obtain

$$\nabla^2 A - \varpi^2 A |\nabla T|^2 - i\left[2\varpi\nabla A \cdot \nabla T + \varpi A \nabla^2 T\right] - -\frac{A\varpi^2}{\alpha^2}$$ (2.42)

Equating the real and imaginary parts, we obtain

$$\nabla^2 A - \varpi^2 A |\nabla T|^2 - -\frac{A\varpi^2}{\alpha^2}$$ (2.43)

$$2\varpi\nabla A \cdot \nabla T + \varpi A \nabla^2 T - 0$$ (2.44)

Dividing (2.43) by $A\varpi^2$ and rearranging, we obtain

$$|\nabla T|^2 - \frac{1}{\alpha^2} = \frac{\nabla^2 A}{A\varpi^2}$$ (2.45)

We now adopt the high frequency approximation that ϖ is large and $1/\varpi^2$ can therefore be ignored,

$$\cdot |\nabla T|^2 \approx \frac{1}{\alpha^2}$$ (2.46)

This can be written in a more general form as $|\nabla T|^2 - \frac{1}{c^2}$, called the Eikonal

equation, where c is the local wave speed, $\alpha(X)$ in the case of P-wave and $\beta(X)$ in the case of S-waves.

The equation can also be expressed as $|\nabla T|^2 - S^2$ where $S=1/c$ is called the slowness. Accordingly, we can write

$$|\nabla T(X)|^2 = (\partial_x T_x)^2 + (\partial_y T_y)^2 + (\partial_z T)^2 - S(X)^2$$ (2.47)

The phase factor T has a gradient whose amplitude is equal to the local slowness. The surface $T(X)$=constant, defines surfaces on which the phase is constant i.e. wavefronts. Radiating energy along $\nabla T(X)$ is perpendicular to the surface $T(X)$ = constant, and are therefore defined as rays.

$$\nabla T = s\hat{k} = S$$ (2.48)

where $\hat{k}$ marks the unit vector in the local ray direction and S is the slowness vector. The function $T(X)$ has the units of time because the wavefronts

advance with local slowness along a direction parallel to the rays, and is simply the time required for a wavefront to reach the point X.

2.6 Partitioning of Energy across seismic discontinuities

When a body wave, P or S, traveling in a homogeneous medium encounters a seismic discontinuity across which the velocity changes, it is refracted according to Fermat's principle that requires the ray parameter p to be conserved by changing its direction to compensate for the change in velocity. In turn, this causes the stresses and displacements associated with the incident and refracted rays on the two sides of the boundary to change and become discontinuous unless supplemented by additional waves generated at the boundary. In general, therefore, the energy of an incident P or S-wave at a boundary is required to be partitioned into 4 new generated waves at the boundary in order to ensure the continuity of displacements and stresses across it. These are: the reflected P, reflected S, refracted P and refracted S, each obeying the Snell's law with respect to the parent wave. The S waves being of transverse nature, their particle motion can be split into two orthogonal components: one in the plane of propagation and the other normal to it. These S wave components are respectively denoted by SV and SH. The latter being confined to the plane perpendicular to the plane of propagation of P and S waves, are completely decoupled from the P wave particle displacement. Therefore the partitioning of an SH wave energy at a boundary will involve only two daughter waves: reflected and refracted SH waves.

Consider an incident P wave traveling in the $x_1 - x_3$ direction, impinging on a horizontal boundary at an angle i (figure below). We can write the displacement potentials corresponding to all 5 waves: the parent and the 2 reflected ones in the first medium and the two refracted ones in the second, in the form (2.37) or (2.39), and require that the associated normal stresses and

displacements at each pair of points on either side of the boundary must be equal.
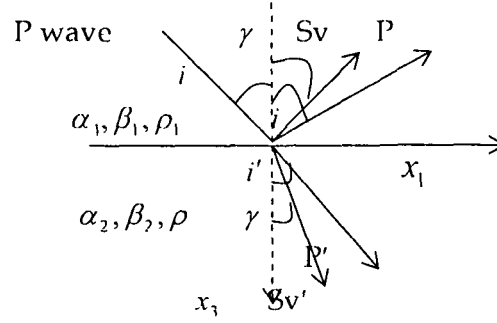
It may be noted that since the particle motion associated with the incident P-wave is confined to the $x_1 - x_3$ plane, it will not generate any SH wave (particle motion in the $x_1 - x_2$ plane) at the interface. However, since the P wave displacements alone cannot combine to yield continuous displacements or tractions across the boundary, additional particle motion in the $x_1 x_3$ plane would be required at each point of the boundary to make up for the difference and this is exactly what the reflected and a refracted SV wave provides.

The P and SV wave potentials, ϕ and ψ, for the 5 wave components,

$$\phi_{(layer1)} = \phi_{incident-ray} + \phi_{reflected-ray} \tag{2.49}$$

$$\phi^+_{(layer2)} = \phi_{refracted} \tag{2.50}$$

$$\psi^- = \psi_{reflected} \tag{2.51}$$

$$\psi^+ = \psi_{refracted} \tag{2.52}$$

can, in turn, be expressed by:

$$\varphi_{incident} = A_1 \exp[i\omega(px_1 + \eta_{\alpha 1} x_3 - t)] \tag{2.53}$$

$$\phi_{reflected} = A_2 \exp[i\omega(px_1 - \eta_{\alpha 1}x_3 - t)]$$

$$\phi_{refracted} = A_3 \exp[i\omega(px_1 + \eta_{\alpha 2}x_3 - t)]$$

$$\psi_{reflected} = B_2 \exp[i\omega(px_1 - \eta_{\beta 1}x_3 - t)]$$ (2.54)

$$\psi_{refracted} = B_3 \exp[i\omega(px_1 + \eta_{\beta 2}x_3 - t)]$$

Particle displacements associated with each of these waves can be derived for any general point on either side of the boundary from (2.72 & 2.73), using the assumed Helmholtz relation: $U(X) = (\nabla\phi + \nabla \times \psi)$ and the various stress components from the relation $[T_{ij} = \lambda\theta\delta_{ij} + \mu\left\{\left(\frac{\partial u_i}{\partial x_j} + \frac{\partial u_j}{\partial x_i}\right)\right\}$. Equating the stresses and displacements at points on either side of the boundary, yield the ratios of post-conversion amplitudes (A_2, A_3, B_1, B_2) with respect to the incident amplitude (A_1), respectively called the reflection and transmission coefficients. These coefficients determine the proportion of the incident energy partitioned among the derived waves. Calculations of these coefficients for a general boundary between two solid media involves complex algebraic manipulations but can be found in various texts (e.g. Lay & Wallace).

Accordingly,

$$T_{PP} = [2\rho_1\eta_{\alpha 1}F(\alpha_1 / \alpha_2)] / D$$ (2.55)

$$T_{PS} = [2\rho_1\eta_{\alpha 1}Hp(\alpha_1 / \beta_2)] / D$$ (2.56)

$$R_{PP} = |(b\eta_{\alpha 1} - c\eta_{\alpha 2})F - (a + d\eta_{\alpha 1}\eta_{\beta 2})Hp^2| / D$$ (2.57)

$$R_{PS} = -[2\eta_{\alpha 1}(ab + cd\eta_{\alpha 2}\eta_{\beta 2})p(\alpha_1 / \beta_1)] / D$$ (2.58)

where $D = EF + GHp^2$ (2.59)

$$E = b\eta_{\alpha 1} + c\eta_{\alpha 2}$$ (2.60)

$$F = b\eta_{\beta 1} + c\eta_{\beta 2}$$ (2.61)

$$G = a - d\eta_{\alpha 1}\eta_{\beta 2}$$ (2.62)

$$H = a - d\eta_{\alpha 2}\eta_{\beta 1}$$ (2.63)

$$a = \rho_2 \left(1 - 2\beta_2^2 p^2\right) - \rho_1 \left(1 - 2\beta_1^2 p^2\right) \qquad (2.64)$$

$$b = \rho_2 \left(1 - 2\beta_2^2 p^2\right) - 2\rho_1 \beta_1^2 p^2 \qquad (2.65)$$

$$c = \rho_1 \left(1 - 2\beta_1^2 p^2\right) + 2\rho_2 \beta_2^2 p^2 \qquad (2.66)$$

$$d = 2\left(\rho_2 \beta_2^2 - \rho_1 \beta_1^2\right) \qquad (2.67)$$

Products of the material density and the wave velocity such as ($\rho\alpha$) or ($\rho\beta$) represent the associated acoustic impedances of the medium. In the case of an incident P-wave at a horizontal boundary, the 4 coefficients for the converted phases can be simply determined for the case of vertical incidence ($I = 0 = p$).

From (2.55-2.60), there are no reflected or transmitted shear waves because both R_{PS}, and T_{PS} are zero. The coefficients of reflected and refracted P waves are respectively reduced to:

$$T_{PP} = \left[2\rho_1 \eta_{\alpha 1} F(\alpha_1 / \alpha_2)\right]/ D = \left[\left(\left[(2\rho_1\alpha_1)/(\rho_1\alpha_1 + \rho_2\alpha_2)\right]\right)\right] \qquad (2.68)$$

$$R_{PP} = \left|(b\eta_{\alpha 1} - c\eta_{\alpha 2})F - (a + d\eta_{\alpha 1}\eta_{\beta 2})Hp^2\right|/ D$$

$$= \left[\left(\left[(\rho_2\alpha_2 - \rho_1\alpha_1)/(\rho_1\alpha_1 + \rho_2\alpha_2)\right]\right)\right] \qquad (2.69)$$

It may be noted that if the wave is traveling from a higher acoustic impedance medium to a lower one, the reflected wave has a negative coefficient signifying a phase reversal at the boundary. This is reflected in the sum of the quantities in (2.68) and (2.69) being equal to unity. Computation of T_{PP} and R_{PP} for different values of the incident angle i, shows that these coefficients have very small gradients near i=0. In fact the coefficients change very little even for incident angles as large as ~ 20°.

2.7 Converted Phases as Response to Time Invariant Linear

System

As stated in the previous section, converted waves derived from a parent incident wave at a boundary, can also be expressed as the output of a linear system. The three main characteristics of a time invariant linear system are:

(i)   Superposition: If $g_1(t)$ is the output of an input $f_1(t)$, and $g_2(t)$ is the output of $f_2(t)$, then the output of $[f_1(t) + f_2(t)]$, is $[g_1(t) + g_2(t).]$

(ii)   Scaling: If $g_1(t)$ is the output of an input $f_1(t)$, then $a\, g_1(t)$ is the output of $a\, f_1(t)$.

(iii)   Shifting (time invariance): If $g_1(t)$ is the output of an input $f_1(t)$, then $g_1(t - t_1)$ is the output of $f_1(t - t_1)$.

Also, the response of a linear system to a unit impulse function called the Dirac-Delta function is known as the transfer function. A Delta function $\delta(t - t_0)$ is defined as a function that is zero for all values of t except at $t = t_0$ where it tends to infinity in a manner that

$$\int_{-\infty}^{\infty} \delta(t - t_0)dt = 1, \text{ and } f(t) = \int_{-\infty}^{\infty} f(\tau)\delta(t - \tau)d\tau \tag{2.70}$$

Consider two time series $f(t)$ and $g(t)$. Then the convolution of these functions is defined as

$$f(t) * g(t) = \int_{-\infty}^{\infty} f(\tau)g(t - \tau)d\tau \tag{2.71}$$

If $g(t) = G[f(t)]$ is output of a linear system to an input $f(t)$, we first express $f(t)$ as an integral involving the delta function as

$$f(t) = \int_{-\infty}^{\infty} f(\tau)\delta(t - \tau)d\tau \qquad (2.72)$$

and the response of the system to the input $|f(\tau)|\delta(t - \tau)$ where $|f(\tau)|$ is the scalar value of $f(t)$ at $t = \tau$

Thus the output $g(t) = G[f(t)]$ of the system to the input

$$f(t) = \int_{-\infty}^{\infty} f(\tau)\delta(t - \tau)d\tau \qquad (2.73)$$

is

$$G[f(t)] = \int_{-\infty}^{\infty} f(\tau)h(t - \tau)d\tau \qquad (2.74)$$

which is known as the convolution integral and the process is called convolution. An inverse process called deconvolution can then yield a knowledge of either the input or the system function from a knowledge of the output or data.

2.8 Receiver Function

A Receiver Function is the record of converted Ps phases from underlying acoustic boundaries or the corresponding Impulse function response. As a P wave travels through the crust and upper mantle, it encounters velocity contrasts where the P wave can be reflected, transmitted and /or converted to as SV wave. Assuming that the distance between the earthquake events and seismometer station is large enough, the angle of incidence of the P wave will be close to vertical within the lithosphere beneath the station and so will be most strongly recorded on the vertical component seismogram, whereas the converted shear waves would be most prominent in the horizontal components.

Calculation of receiver function therefore would involve a rotation of the horizontal components to lie parallel and orthogonal to the great circle path along the Earth's surface, between the source and the receiver. The signal recorded by a seismometer can then be viewed as a convolution in the time domain:

$$X_i(t) = S(t) * I(t) * E_i(t) \qquad i = Z, R, T \qquad (2.75)$$

where Z, R and T represent the vertical, radial and transverse components of motion respectively, S(t) represents the near source and mantle propagation effects, I(t) is the instrument response and E(t) is the Earth's response below the receiver.

As the SH phases are a minor feature of the vertical seismogram (Langston, 1979) for teleseismic events, we can write

$$X_Z(t) \approx S(t) * I(t) \qquad (2.76)$$

Therefore a receiver function can be isolated from the radial or tangential seismograms by deconvolving the source and instrument responses, which corresponds to the vertical seismogram. Figure 2.1 shows the phases that arrive at a seismometer station as a result of interaction with a single crustal layer over an upper mantle half-space, and the corresponding radial receiver function.
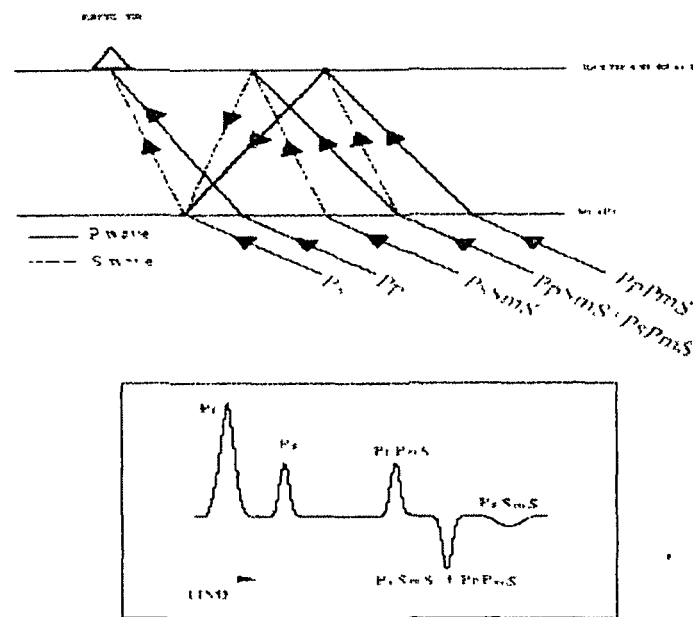
Figure 2.1: (top) A series of seismic phases being generated at a single sub-receiver interface. Solid lines represent the P-wave and dotted lines represent the S-wave. (bottom) The radial receiver function corresponding to the simple earth model shown in top.

In general, of course there would be some energy scattered away from the Fermat plane, and would appear on the transverse component of the seismogram. Its amplitude can thus be deemed to provide a measure of the departure of the underlying earth structure from the ideal radially symmetrical, or over a limited region, a layered flat earth model.

As our objective is to investigate the shear wave speed structure of the earth to a depth of the sharpest discontinuity, and this information is contained in $E_R(t)$, we first need to abstract this function from the seismogram before proceeding to invert this function to obtain the velocity structure.

There exist several methods of extracting receiver function. As for example, the water level stabilized frequency domain deconvolution process (Clayton and Wiggins, 1976), the time domain approach (e.g. Gurrolaet al., 1995 and Sheehan et al., 1995) and the iterative time domain deconvolution procedure (Pablo Ligorria and Ammon, 1999).

Frequency domain deconvolution technique exploits the fact that convolution of two functions in the time domain is equal to the product of their Fourier Transforms of each. So, we can take the Fourier transforms of the quantities to get the corresponding equation in the frequency domain. Finally, by taking the Inverse Fourier Transform of $E_R(\varpi)$ one can recover $E_R(t)$.

Alternatively, one can abstract $E_R(t)$ directly without forward and backward Fourier transformation, by recognizing the fact that this function when convolved with the vertical yields the radial, and therefore building a function iteratively, which when convolved with the vertical seismogram would yield the radial. Specifically, the process is based on the source-time function estimation algorithms of Kikuchi and Kanamori (1991). The process begins by cross-correlating the vertical and radial component seismograms to establish the lag of the first and largest spike in the receiver function. Convolution of the current estimate of the receiver function with the vertical component seismogram is then subtracted from the radial component seismogram to form an updated radial seismogram. This means that after one iteration there exists a synthetic receiver function containing only one spike which models the direct P arrival, and a new radial seismogram lacking the direct P arrival. The same process is then repeated several times using the iteratively updated radial seismograms to look for the subsequent spike lags and amplitudes. At each iteration a misfit function between the vertical seismogram and receiver function convolution, with the real radial component seismogram is computed. By repeating the above procedure, we

finally get a train of delta functions which when convolved with $E_Z(t)$ gives a function that is very close to $E_R(t)$, i.e., the desired receiver function.

2.9 Surface Wave Dispersion, Phase and Group Velocity

Surface wave dispersion measurements have been employed for a long time to understand the average structure of the crust and upper mantle. Surface wave group and phase velocities are mainly sensitive to the shear structure of the underlying crust and upper mantle. A pulse shaped waveform become spread out (dispersed) as the different frequency components become spatially separated when the different frequency components of the wave packet travel at different velocities. The associated phase velocity of each frequency component defines the wave speed of that particular frequency. Also the various frequency components of the signal will undergo interference effects leading to the overall canceling out of energy except at particular times defined by the group velocity of the wave as the waveform, originally a pulse of energy, become dispersed.

Consider a seismic signal with only two frequencies ϖ_1 and ϖ_2. Then we have

$$U(x,t) = \cos(\varpi_1 t - k_1 x) + \cos(\varpi_2 t - k_2 x) \qquad (2.77)$$

where $U(x,t)$ is the observed displacement due to the seismic signal, $\varpi_1 = \varpi - \delta\varpi$, $\varpi_2 = \varpi + \delta\varpi$, $k_1 = k - \delta k$, $k_2 = k + \delta k$ and ϖ, k are the average frequency and wave number respectively.

Substituting the values of $\varpi_1, \varpi_2, k_1, k_2$ in equation (2.94), we obtain

$$U(x,t) = 2\cos(\varpi t - kx) + \cos(\delta k x - \delta\varpi t) \qquad (2.78)$$

In the above equation ϖ is the average frequency and $\delta\varpi$ is the modulated frequency of the resultant waveform defined by the equation (2.106). The

wave speed for the shorter period signal is $c = \dfrac{\varpi}{k}$ (phase velocity) and for the

longer period is $u = \dfrac{\delta\varpi}{\delta k}$ (group velocity) (Lay and Wallace, 1995).

2.10 Inverse Theory

Most of the physical problems require estimation of system parameters, which cannot be obtained directly from the observed data. This inverse estimation depends on the availability of a physical theory that defines the physical influences by relating the values of the parameters [m] to observed data [d] in a form Gm=d, where m may represent a column vector of m quantities m_i to be estimated, d a column vector of n data sets d_n, and G the Green's Function matrix G_{jk}. It is very rare to have a unique inverse (G^{-1}) of G such that G G^{-1}= $G^{-1}G$=I, which enables one to calculate m from the data d by the inverse relation m= $G^{-1}d$.

In spite of the fact that the data (observable) are completely free from error, G must be square and non-singular to avail a unique inverse G^{-1} of G. Since all physical measurements involve some errors, experiments are usually designed in a manner that the presence of errors in the data is indicated, and · the measurements are made in large numbers than the model parameter set. Such a problem is known as an over-determined problem and the solution of such problems are obtained by using minimization techniques.

2.10.1 Least Square Solution

Consider that $G\,m = d$. Since this is an over determined system, G will not be a square matrix and consequently will have no unique inverse.

Let G' be an acceptable inverse of G i.e. [G'G =I].

Then we can write

$$G'(Gm) = G'd = \hat{m} \tag{2.79}$$

$$G\hat{m} = \hat{d} \tag{2.80}$$

Now we minimize

$$|d - G\hat{m}| \quad \text{i.e.} \quad (d - G\hat{m})^2 = E \tag{2.81}$$

in order to make sure that $\hat{m}$ is very close to m.

Replacing $\hat{m}$ by m, we obtain

$$E = (d - Gm)^T (d - Gm)$$

$$= \sum_{I}^{N} [d_I - \sum_{J}^{M} G_{IJ} m_J][d_I - \sum_{k}^{M} G_{Ik} m_k]$$

$$= \sum_{I}^{N} [d_I d_I - d_I \sum_{J}^{M} G_{IJ} m_J - d_I \sum_{k}^{M} G_{Ik} m_k + \sum_{J}^{M} \sum_{k}^{M} G_{IJ} G_{Ik} m_J m_k] \tag{2.82}$$

$$= \sum_{J}^{M} \sum_{k}^{M} [m_J m_k \sum_{I}^{N} G_{IJ} G_{Ik}] - 2 \sum_{J}^{M} [m_J \sum_{I}^{N} G_{IJ} d_I] + \sum_{I}^{N} d_I d_I$$

Now we demand a model $m(m_q)$ for which

$$\frac{\delta E}{\delta m_q} = 0. \tag{2.83}$$

As such

$$\frac{\delta E}{\delta m_q} = \sum_{J}^{M} \sum_{k}^{M} [\delta_{Jq} m_k + m_J \delta_{kq}] \sum_{I}^{N} G_{IJ} G_{Ik} - 2 \sum_{J}^{M} \delta_{Jq} \sum_{I}^{N} G_{IJ} d_I$$

$$= \sum_{J}^{M} \sum_{k}^{M} [m_k \sum_{I}^{N} G_{Iq} G_{Ik} + m_J \sum_{I}^{N} G_{IJ} G_{Iq}] - 2 \sum_{I}^{N} G_{Iq} d_I$$

$$= 2 \sum_{k}^{M} m_k \sum_{I}^{N} G_{Iq} G_{Ik} - 2 \sum_{I}^{N} G_{Iq} d_I \tag{2.84}$$

We can express the equation in matrix form as

$$G^T Gm - G^T d = 0$$ (2.85)

Thus, the least square solution of the inverse problem $Gm = d$ is given by

$$\hat{m} = [G^T G]^{-1} G^T d .$$ (2.86)

2.10.2 Finding of Velocity Structure of the Earth using Minimization Technique

Simultaneous inversion of receiver function and surface wave dispersion can be employed to determine a single velocity model beneath the earth surface. This inversion scheme seeks to find a minimum to the following objective function,

$$S = [(1-p)N_r + pN_s] \left[\frac{(1-p)}{N^r} \sum_{i=0}^{N^r} \left(\frac{O_{ri} - P_{ri}}{\sigma_{ri}} \right) + \frac{p}{N^s} \sum_{j=0}^{N^s} \left(\frac{O_{sj} - P_{sj}}{\sigma_{sj}} \right) \right]$$ (2.87)

where S is the standard error between the observed and predicted data, p is a weighting value, O_{ri} is the ith observed receiver function measurement, O_{sj} is the jth observed surface wave dispersion measurement and P_{ri}, P_{sj} are the corresponding predicted values based on the current velocity model. N^r and N^s are the number of receiver function and surface wave measurements respectively and σ_{ri} and σ_{sj} are the standard error limits for the ith and j^{th} pieces of receiver function and surface wave information respectively.

Consider the current model M_0 and the residual matrix [d] corresponding to the model. Then the matrix [d] is represented by a linear combination of changes to the current model as follows:

$$w[G].[\delta m] = |d|$$ (2.88)

where $[G]$ is the partial derivative matrix with respect to changes in the current model, $[\delta m]$ is the model correction vector and w is the weighting system.

If we expand the above equation it will take the form as follows:

$$\begin{bmatrix} w_r & 0 \\ 0 & w_s \end{bmatrix} \begin{bmatrix} \dfrac{\delta r}{\delta m_1} & \dfrac{\delta r}{\delta m_2} & \cdots & \dfrac{\delta r}{\delta m_N} \\ \dfrac{\delta s}{\delta m_1} & \dfrac{\delta s}{\delta m_2} & \cdots & \dfrac{\delta s}{\delta m_N} \end{bmatrix} \begin{bmatrix} \Delta m_1 \\ \Delta m_2 \\ \vdots \\ \Delta m_N \end{bmatrix} = [d]$$

(2.89)

where

$$w_r = [(1-p)N_r + pN_s]\left(\frac{1-p}{N_r \sigma_r}\right)^{1/2}$$

(2.90)

$$w_s = [(1-p)N_r + pN_s]\left(\frac{p}{N_s \sigma_s}\right)^{1/2}$$

(2.91)

The equation (2.117) can be written in a short notation as

$$[d] = \begin{bmatrix} w_r res \\ w_s res \end{bmatrix}$$

(2.92)

where

$$w_r res = w_r \sum_{i=1}^{N}\left[\frac{\delta r}{\delta m_i}\Delta m_i\right]$$

(2.93)

and $\quad w_s res = w_s \sum_{i=1}^{N}\left[\frac{\delta s}{\delta m_i}\Delta m_i\right]$.

(2.94)

Singular value decomposition technique is employed to minimize the objective function S. Being the no-linearity involved in the forward problem, an iterative sequence of linearised inversion steps are used to approach a minimum of S.

2.11 Seismic Anisotropy

Seismic rays, by analogy to optical rays also suffer birefringence when crossing material media with directional properties. Geological materials invariably exhibit this property because of prevailing stresses and fractures in the earth or due to preferential alignment of anisotropic crystals such as olivine which is one of the principal minerals in the earth's mantle. A seismic shear wave entering upon an anisotropic region thus splits into two phases with polarizations and velocities that mimic the properties of the anisotropic media. The phases, polarized into fast and slow directions, progressively separate in time as they propagate through the anisotropic media. This split is preserved in any isotropic segment along the ray path and can be detected as a time delay between two horizontal components of motion, its polarity and amplitude being strongly affected by the azimuth of an arriving wave. The existence of such split S-waves, whenever detected, therefore signifies the presence of anisotropy and an analysis of the polarity and amplitudes of the split phases, yields knowledge of the anisotropy characteristics of the subsurface.

In an anisotropic medium, there are three plane waves that propagate with three different speeds and with mutually perpendicular polarizations. Because of the near parallelism (not more than 10° away from parallel and perpendicular to the propagation direction), the three waves are often referred to as the quasi-P and quasi-S waves. Quasi-SV and quasi-SH are occasionally used instead for the polarizations that are closest to being in and out of the sagittal plane respectively.

The polarizations and speeds of the two quasi-S waves are determined by both the properties of the medium and the propagation direction through the medium. The time delay (δt) between the two quasi-S waves depends on both

the path length in the anisotropic material and the difference in speed between the two quasi-S waves. This can be obtained by

$$\delta t = L(1/V_{s1} - 1/V_{s2})$$ (2.95)

where V_{s1} and V_{s2} represent the speeds of the two quasi-shear waves given the direction of propagation and the material properties and L is the length of the anisotropic path traversed. The differences between V_{s1} and V_{s2} are often reported as a percent anisotropy Ks, calculated as

$$Ks = 200(V_{s1} - V_{s2})/(V_{s1} + V_{s2})$$ (2.96)

However, this anisotropy should be distinguished from the intrinsic anisotropy of the material, which is defined as the percent difference between the maximum and minimum velocities (Birch, 1961).

A shear wave traversing in an anisotropic layer splits according to equation (2.112). The splitting is preserved if the shear wave then subsequently traverses an isotropic layer and the polarization of the first shear wave (ϕ) and δt can be determined. ϕ and δt are called the shear wave splitting parameters, or simply the splitting parameters. The amplitude of the fast and slow shear waves is directly proportional to the amplitude of the initial S wave in the fast and slow directions, respectively (the S wave polarization). After passing through a single anisotropic layer and entering an isotropic layer, the P wave has the same linear particle motion as before, but the S wave has a characteristic shape that depends on δt compared to the period. For large splitting or short periods the two split shear waves may be entirely separated from each other and the polarization diagrams take on a cruciform appearance with the initial polarization from the fast quasi-S wave and one from the slow quasi-S wave (e.g., Keith and Crampin, 1977). On the other hand, for smaller splitting or longer periods the two split waves are separated

by only a fraction of a period and the initial portion of the particle motion is linear and polarized in the fast direction, but the majority of the waveform has elliptical particle motion. With assumptions about the type and degree of anisotropy, ϕ determines the orientation of the anisotropic symmetry system, and δt gives the thickness of the anisotropic layer. Furthermore, by knowing the relationship between the orientation of the system and the strain, one can infer the orientation and magnitude of the strain.

Chapter 3

Data and Methodology

Outline

This chapter describes the analytical approaches and procedures used for studying the seismic characteristics of northeastern India. At the outset is given a brief account of the sources of data used in this dissertation followed by a detailed treatment of the rationale and methodologies used for i) scrutinizing the quality of data, ii) calculating and inverting receiver functions to determine the shear wave speed structure in the crust and the upper mantle, and iii) for studying the anisotropic characteristics of the crust.

3.1 The Seismic Data

Three component broad band seismic data were generated at 12 sites in northeast India (Figure 3.1) by the Tezpur University under a collaborative project with the Indian Institute of Astrophysics at Bangalore, Indian Institute of Technology at Kharagpur and the University of Cambridge (UK). Each station consisted of a Guralp CMG-3TDM sensor with a flat velocity response between 0.0083 and 50 Hz, and a Guralp SAM/DCM data logger. Data were continuously recorded at 100 samples per second and time-stamped by a GPS receiver. Additionally, some available data generated by the DST sponsored stations operated by the National Geophysical Research Institute (NGRI), the Indian Meteorological department (IMD) and Gauhati University, were also

included in the analysis. The seismographs at Agartala (AGT) and Karimganj (KMG) were located on the sediments of the Bengal Basin south of the Shillong Plateau. Those at Cherapunji (CHP), Barapani (BPN), Nongpoh (NOG) and Tura (TUR) were installed on the exposed Precambrian crystalline basement of the Shillong Plateau whilst the Baihata (BAI), Boko (BOK) and Tezpur (TEZ) seismic stations were located on the low-lying basement ridges (foreland spur) in the Brahmaputra Valley, and Borjuri (BOR) on the northwestern Mikir Hills. The two Himalayan stations Bomdila (BMD) and Tawang (TWG) were each installed on bedrocks in the Lesser and the Greater Himalayas respectively (Figure 3.1). The three stations for which we obtained data from NGRI, IMD and Gauhati University were also located on basement outcrops of the Shillong plateau at Hamren (HMN) and Shillong (SHL), and at Gauhati (GAU) on the exposed basement in the Brahmaputra valley. In addition to these Indian stations, we also used data from the permanent Chinese Digital Seismic Network (CDSN) station at Lhasa (LSA) and the six INDEPTH II stations (SP27, SP25, BB23, BB20, BB18 and BB14) for which broadband data were obtained from the Incorporated Research Institution in Seismology (IRIS) data center. Fortunately, some of these data sets had a fairly good azimuthal coverage to yield well-constrained models of the seismic characteristics of the region. A list of the data inventory, station locations and periods of data availability at each of the stations used in this study is presented in Table 3.1. Figure 3.2 shows an example of a three-component broadband seismogram recorded at Baihata (BAI)
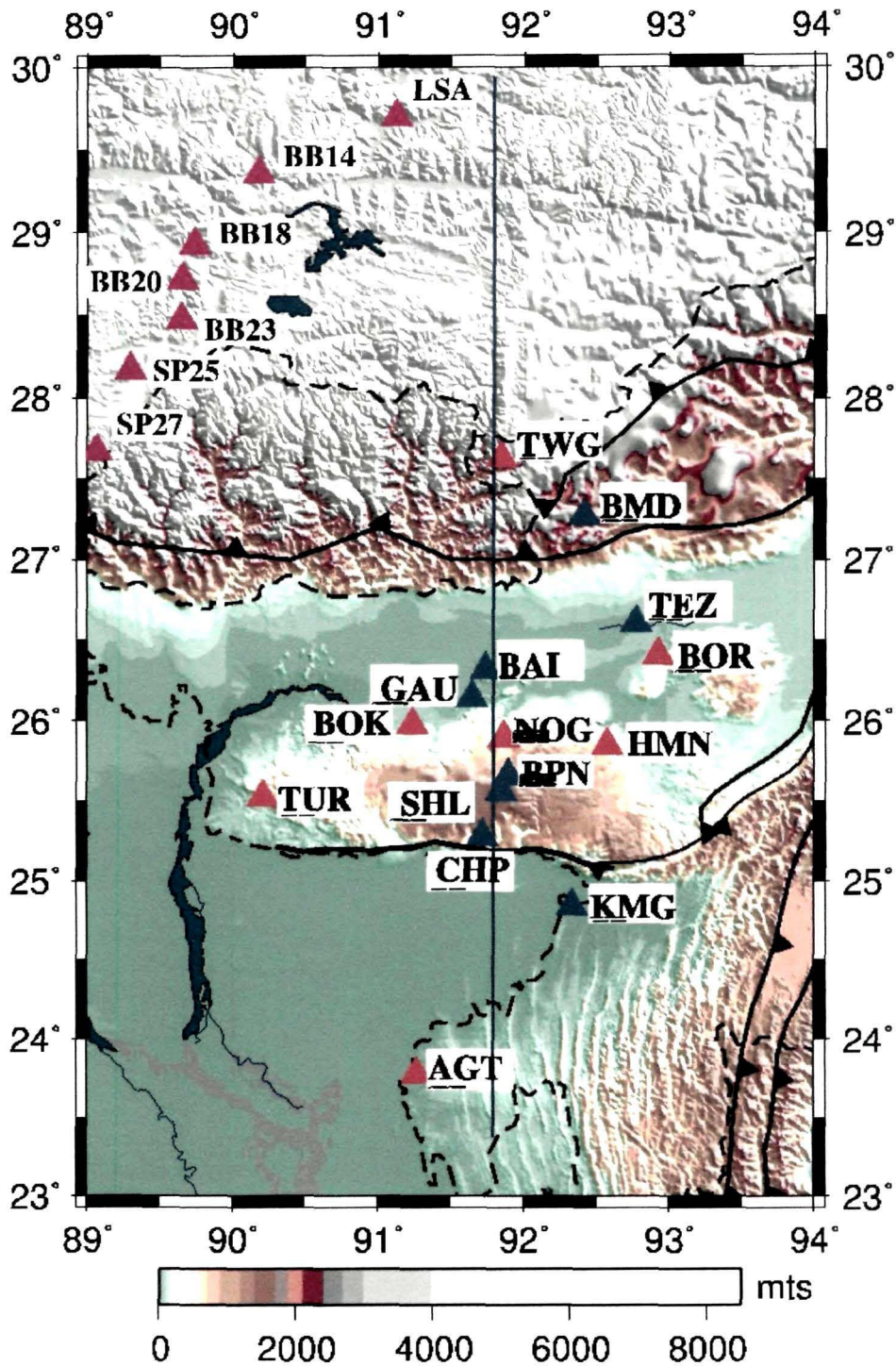
Figure 3.1: Map of Northeastern India, showing the location of broadband seismic stations whose data were used in this dissertation. Blue and purple (the INDEPTH II stations) triangles mark the sites for which receiver functions were calculated by Mitra et al. (2005) and red triangles denote the sites since added where additional data were generated for the present work.

Table 3.1: Location of Broadband Seismic Stations and periods of data availability.

Station Name	Lat°	Long°	Altitude (in meters)	Period of Availability of Data Year/Julian day
TWG	27.6298	91.8583	3800	2004137 - 2005342
BMD	27.2713	92.4181	2477	2002164 - 2006021
TEZ	26.6330	92.8530	77.97	2001001 - 2006003
BOR	26.4112	92.9321	67.54	2005134 - 2005354
BAI	26.3180	91.7390	69.82	2002195 - 2003027
GAU	26.1500	91.6500	49.00	2002064 - 2002104
BOK	25.9799	91.2422	55.47	2005130 - 2006003
NOG	25.8999	91.8669	512	2005134 - 2006273
HMN	25.8548	92.5808	528	2001171 - 2001181
BPN	25.6690	91.9080	976	2001065 - 2006034
SHL	25.5660	91.8550	1554.6	2000035 - 2002148
TUR	25.5300	90.2114	388	2005130 - 2006003
CHP	25.2800	91.7230	1121	2001065 - 2005101
KMG	24.8460	92.3430	16.00	2003337 - 2003364
AGT	23.7874	91.2711	15.78	2003337 - 2005092
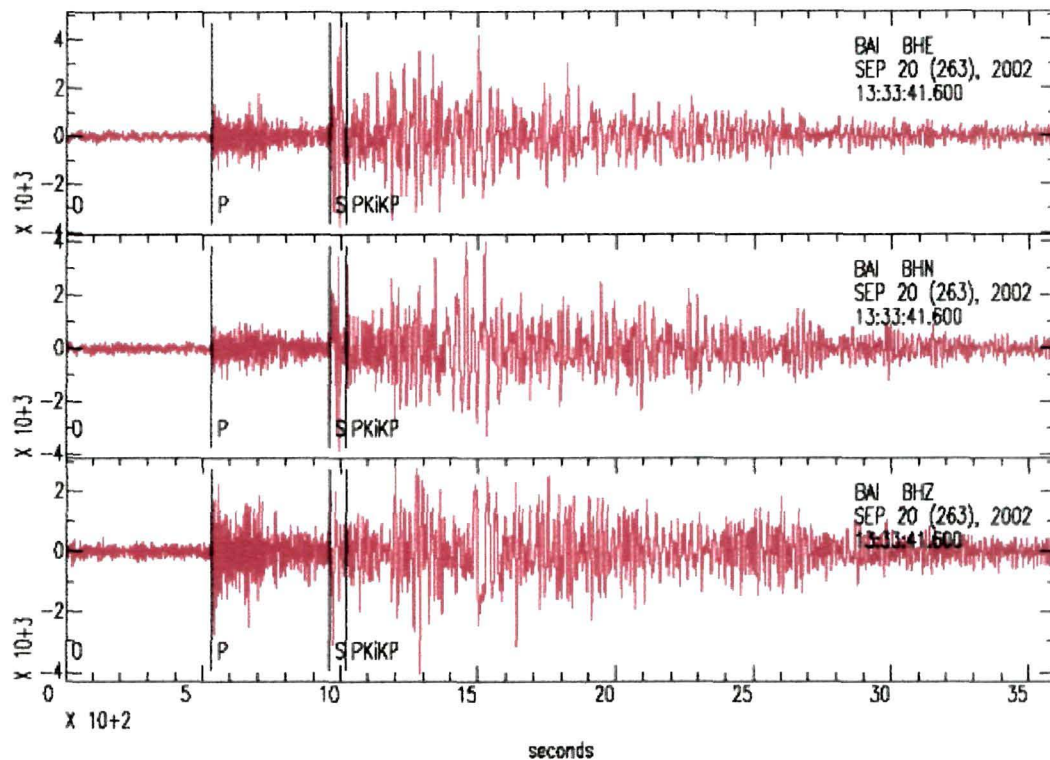
Figure 3.2: Three-component broadband seismogram of an M6.0 event of September 20, 2002 recorded at Baihata (BAI) in Northeast India. The earthquake occurred at 13 hrs 33 min and 41.6 seconds. The source latitude 1.743E, longitude 134.013N and magnitude 6.0, were obtained from NEIC-PDE catalogue.

3.2 Seismogram Analysis

Planet earth is for the most part, a spherically layered body which from its centre upto within ~200 km of the surface, can be regarded as a stack of concentric homogeneous spherical shells. Nearer the surface its longer lived solid state has the strength to preserve inhomogeneous structures and materials created by a succession of earth processes since its earliest structurization.

A seismic record or a seismogram is the time varying record of ground motion at the site caused by diverse streams of energy arriving from some source of mechanical instability within the earth. Wave trains along a multiplicity of ray paths in the earth between the source and the receiver, introduced by the presence of reflecting, refracting and diffracting heterogeneities in the earth, arrive at slightly differing times thereby sustaining a continuous state of ground vibration over a period determined by the interval between the first significant arrival and the last. Since the Fermat ray paths of energy flow through a largely layered earth, they can be fairly well charted using Snell's laws and it would be readily seen that ray paths from near events traverse a large part of the crust and upper mantle between the source and the recording site and would therefore contain information that largely characterizes the lateral crustal heterogeneities. Distant earthquakes on the other hand, would be dominated by the relatively simpler velocity structure of the core and the deep mantle.

Since the wave amplitude of the energy radiated from an earthquake source is small all along the ray path except in its immediate neighbourhood, the assumption of linear elasticity is valid and the earth-structure behaviour can be approximated to that of a linear system. Ground motion recorded on seismograms can therefore be regarded as the output of a linear earth structure to a mechanical instability injected in its body in the form of an impulsive force (an earthquake slip). Or, the output ground motion $R(t)$ at a site can be expressed as the convolved product of the composite earth structure representing the domain between the source and the receiver,

$$E(t) = \sum E_k(t)\text{, arising from a source of vibrations } S(t):$$

$$R(t) = S(t) * \sum E_k(t) \tag{3.1}$$

The diverse problems of seismic analysis consist in extracting either $S(t)$ or some k^{th} component of the composite earth structure $\sum E_k(t)$ from the seismic record of ground motion $(R(t)$, both exercises being essentially non-unique. The questions addressed in this dissertation relate to the second category of the above mentioned problems all of which have to contend with the obvious issue of having to isolate and separate from the seismic record that part of the earth structure response which is not pertinent to a specific quest. At the outset, of course, a sensible step is to screen seismograms before their detailed analysis, for freedom from spurious and unwanted signals such as those that may creep in because of misalignment of sensors, unstable or noisy site and environmental conditions, or contributions from localized scatterers. The next obvious strategy for focusing on a specific part of the earth structure is to select seismograms generated by events at an appropriate epicentral distance. Finally, selective highlighting of information pertaining to specific earth features being investigated, can be accomplished by exploiting the understanding of how the various phases of a sequence of ground motion may be identified with location specific physical processes of reflection, refraction and interference within the earth. For example, in addressing the problem of determining the shear wave speed structure beneath a receiver by analyzing the converted waves from their boundaries, i.e., location of refracting layers underneath and their respective shear wave speeds, we select i) high quality seismic records from amongst distant earthquake records ($30°<\Delta<90°$) so that ray paths to the receiver would be incident at a steep enough angle to sample a deep cylindrical region of small radius about the receiver, and ii) focus for analysis that part of the seismic waveform which includes the first P wave arrival and ~60-90 sec long wave train immediately following it. For, the latter contains a succession of slower traveling shear waves generated from the incident P wave at the various acoustic boundaries beneath the seismic station which, despite being feeble, can be retrieved

because the much larger main shear wave phase from a distant earthquake would not arrive earlier than ~ 300 seconds after the first P-impulse.

3.2.1 Data Quality Test: Polarization Analysis

In a spherically layered earth with wave speed increasing towards the center, the Fermat ray path between an earthquake source and a surface receiver is curved, concave upwards, and lies in the plane containing the source, the receiver and the centre of the earth. Since the emergent ray vector at the surface also marks the direction of the P-wave oscillations which are linearly polarized, it is expected to be concordant with the back-azimuth. Scattering of any part of the P-wave energy away from the Fermat plane by lateral inhomogeneities would degrade the linear polarization of the emergent P-wave. Deviations in the direction of approach of seismic waves from their expected azimuth therefore provides a measure of contamination of the seismic signal with off-azimuth arrivals and/or possible misalignment of the seismic receiver.

Polarization analysis of teleseismic body-wave data which have been widely used for investigating the presence of anomalous structural features such as lateral inhomogeneities in the crust and upper mantle (Crampin et al., 1982; Hu and Menke, 1994; Farra and Begat, 1995; Bokelmann, 1995), by that very token, proves valuable in screening seismograms intended for analyzing the vertical structure beneath a seismic station. Among the several methods used for scrutinizing the integrity of the P-wave polarization from a three component seismogram, the simplest is a visual inspection of the particle motion diagram plotted between each of the two pairs of the three seismogram components. The linearity and inclination of the particle motion have obvious significance. For, whilst the first gives an indication as to whether the incident arrival represents a plane-polarized wave (Samson,

1983a), the latter allows estimation of its azimuth and inclination. However, it becomes difficult to rely on the visual inspection of the particle motion diagram if more than one arrival is superimposed at the same time because the resulting complex waveform will have a less linear particle motion making it difficult to identify the major axis of the polarization ellipse. A more general approach is to make an eigenvalue analysis of the first few seconds of the P-waveform to determine the observed azimuth of a P-wave arrival within a typical frequency window, and compare it with the expected wave propagation path calculated from a knowledge of the source and receiver coordinates. The principal axes (V_i) of the polarization ellipsoid are calculated by diagonalizing the covariance matrix S of the North, East and Vertical component time series of the 3-component seismograms.

$$S = \begin{pmatrix} var[Z] & cov[Z,N] & cov[Z,E] \\ cov[N,Z] & var[N] & cov[N,E] \\ cov[E,Z] & cov[E,N] & var[E] \end{pmatrix} \tag{3.2}$$

where the covariance of two variables X_1 and X_2 of n observations with means μ_1 and μ_2 respectively is given by

$$cov[X_1, X_2] = \frac{1}{n} \sum_{i=1}^{n} (X_{1i} - \mu_1)(X_{2i} - \mu_2)$$

and $cov[X_1, X_2] = cov[X_2, X_1]$

and V_i are determined by solving the eigenvalue equation:

$$(S - \lambda I)V = 0 \tag{3.3}$$

The azimuth of approach and the angle of incidence respectively are:

$$BAZ = \arctan\left(\frac{V_1^I}{V_1^N}\right), \qquad INC = \arctan\left(\frac{V_1^{rad}}{V_1^Z}\right) \tag{3.4}$$

where V_1^I, V_1^N, V_1^Z are the eigenvectors corresponding to the east, the north, and the vertical, and V_1^{rad} represents the radial direction.
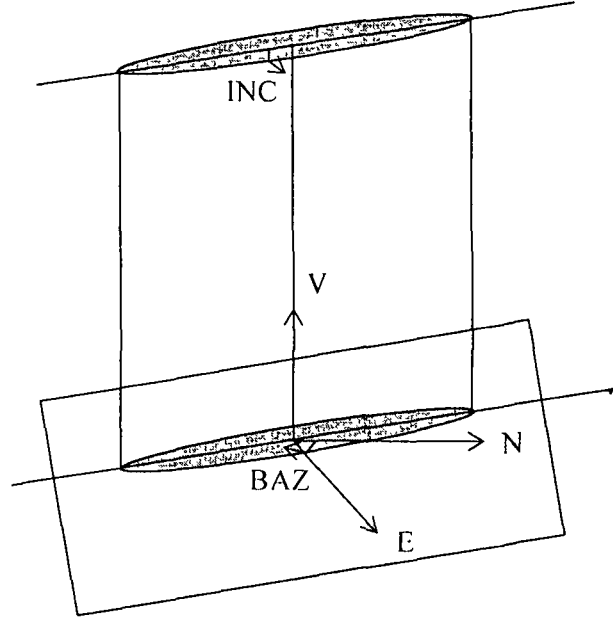
Figure 3.3: Schematic representation of the polarization ellipsoid (taken from A. K. Rai, 2004, personal communication). The three principal axes are marked as V, N and E. Back-azimuth (BAZ) and incidence angle (INC) are also shown in the picture.

Furthermore, the analysis enables determination of the degree of rectilinearity R of the motion defined as

$$R = \text{Rectilinearity} = \left[1 - \frac{\lambda_2 + \lambda_1}{2\lambda_1} \right]$$ (3.5)

which takes the value 1.0 when there is only one non-zero eigenvalue, as for pure P-wave, the value 0.5 when $\lambda_1 = \lambda_2, \lambda_1 = 0$ (i.e. circular polarization) and the value 0 when $\lambda_1 = \lambda_2 = \lambda_1$ (i.e. spherical polarization).

It is instructive to keep in mind the possible sources of error in the calculation of azimuthal anomalies. For example, errors in epicentral location affect the calculated azimuth. Also the reliability of polarization measurements depends on the duration of the analysis window because multiply reflected and converted phases generated in the near surface can affect the results. In practice, the window of analysis extends upto one cycle of the dominant period of motion both before and after the P-wave onset.

Results of the P-wave polarization analysis for all 10 stations of northeastern India whose data have been used in this dissertation are shown in Figure 3.4. For each set of the three component seismograms analysed, the data were filtered prior to the principal component analysis through two distinct and separate frequency bands. The first band pass filter (0.06 Hz - 0.2 Hz) corresponding to wavelengths comparable with crustal dimensions (100 - 30 kilometers) are expected to be less sensitive to the details of the crustal structure. The second pass band set at 0.5 to 2.0 Hz and corresponding to smaller dimensions of 12 to 3 kilometers, are more sensitive to structural variations on a smaller scale. Results of analysis of these two sets of band-passed filtered data are shown separately for each station: frequency band of 0.06-0.2 Hz on the right, and frequency band of 0.5-2.0 Hz on the left. For each event analyzed, the calculated back-azimuth is plotted with a red line and the characteristic polarization axis in blue. These figures for all the northeast Indian stations illustrate the close parallelism between the polarization axes of the P-wave and the calculated back-azimuths, over a fair range of azimuths and epicentral distances, with a standard deviation of less than 5°. They therefore testify that the corresponding time series selected for a detailed analysis of the seismic characteristics of the region could be fairly regarded as consisting of plane wave arrivals consistent with the expected azimuth, and that within the frequency band of interest, they were substantially free from any contamination by scatterers in the vicinity of the receiver.
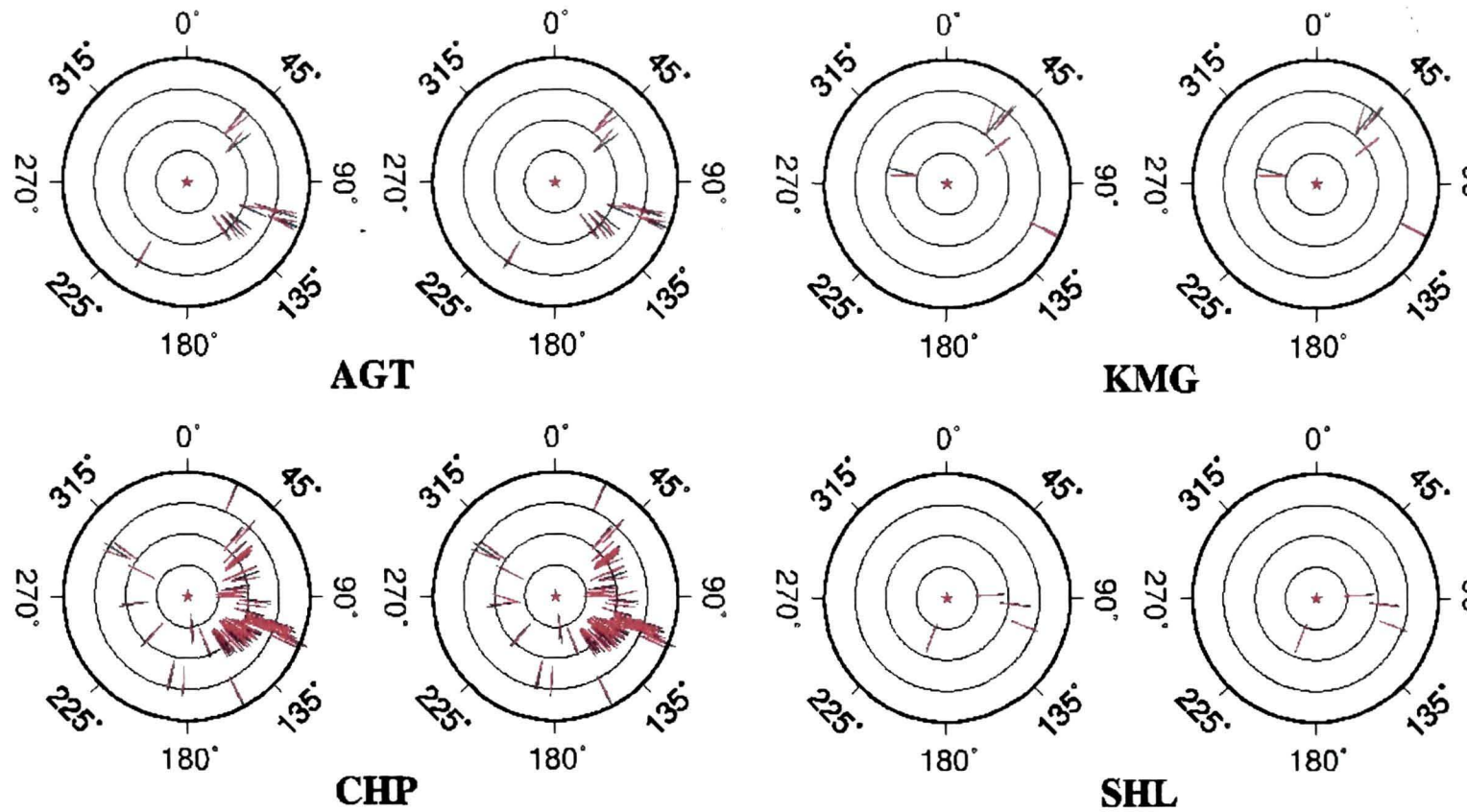
Figure 3.4: Characteristic polarization measurements. For each stations, (left) back-azimuth anomaly in the frequency band of 0.06-0.2 Hz and (right) back-azimuth anomaly in the frequency band of 0.5-2.0 Hz. For each event analysed, the calculated event back-azimuth is plotted with a red line and the characteristic polarization axis in blue. The great circle arc length between source and receiver is indicated by the position of the lines on the polar plots (0° at the origin with 30° increments).
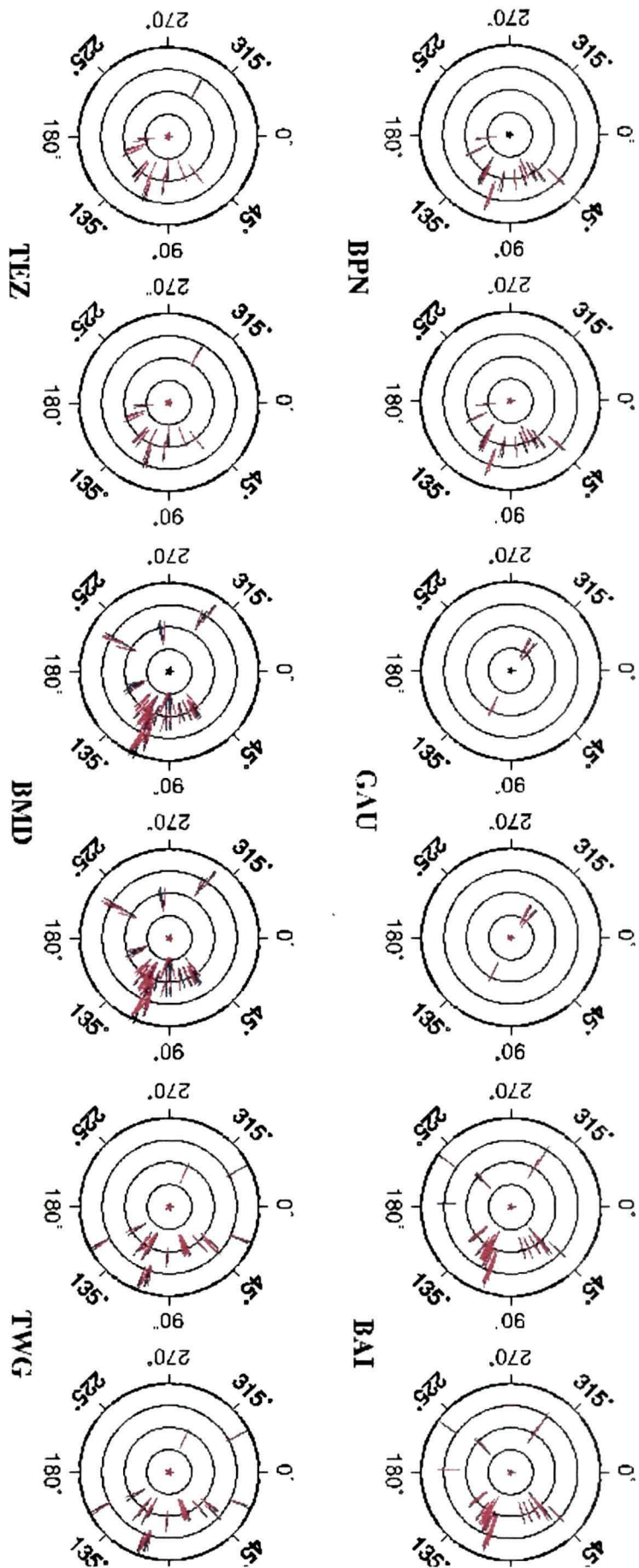
Figure 3.4: - (Continued.)

3.3 ·Determination of the Shear-Wave Speed Structure of the Crust and Upper Mantle

3.3.1 Teleseismic P-wave Receiver Function

Shear wave speed structure i.e., $V_s(Z)$ of a selected earth column beneath a seismic station can be determined from an analysis of converted shear wave phases generated at acoustic impedance boundaries within the column, by the first arriving P-waves incident at the bottom of the column. This approach is based on the recognition that the horizontal component ground motion $R_h(t)$ at the column's surface caused by the converted shear phases $P_s(t)$, can be expressed as the convolution of the incident generator P-wave $P(t)$ at the bottom of the column with the overlying earth structure response $E_h(t)$:

$$R_h(t) = P(t) * E_h(t) \tag{3.6}$$

Equation 3.6 shows how $E_h(t)$ may be extracted from a horizontal component seismic time series $R_h(t)$ by deconvolving from $P(t)$ or its proxy record on the vertical component, that is, $R_v(t)$. The earth structure response $E_h(t)$ thus represents the impulse function response of the earth column to P-wave excitation and can be shown to be a function of the shear wave structure $Vs(Z)$ within the column, which can thereby be inverted to yield the desired $Vs(Z)$ of the earth column. Manifestly, the earth structure response $E_h(t)$ principally contains information of the seismic characteristics of the laterally confined earth column beneath the receiver and is therefore aptly called the Receiver Function.

The use of receiver functions to determine the shear wave structure of the crust and upper mantle beneath a three-component broadband seismograph station is now a well-established seismological method widely applied for

exploring the shear wave speed structure inside the earth (e.g., Langston, 1979; Owens et al. 1984; Ammon, 1991; Zhu and Kanamori, 2000; Rai et al., 2003).

Deconvolution to extract the receiver function may be performed in the frequency domain (Claton and Wiggins, 1976; Langston, 1979; Ammon, 1991) or in the time domain (Liggoria and Ammon, 1999, Park and Levin, 2000). Both these approaches work well when the data are wideband with good signal-to-noise levels, but are subject to the endemic instability of the deconvolution process caused by the ubiquitous presence of noise. For northeastern India stations, the most stable receiver functions were obtained using the iterative time-domain deconvolution technique (Liggoria and Ammon, 1999). This method, recognizing that the horizontal component of the P waveform consisting of the P-to-S converted phases, is the convolved product of the incident P wave signal with the receiver function, uses a least-squares minimization of the difference between the observed horizontal seismogram, and a predicted signal generated by the convolution of an iteratively updated spike train with the corresponding vertical component seismogram. The process is based on the source-time function estimation algorithms of Kikuchi and Kanamori (1991). The method originally devised for estimating the radial receiver function is equally applicable to the transverse motion and can be easily generalized to accommodate simultaneous deconvolution of any number of signals. This process begins by first cross-correlating the vertical component with the radial to establish the lag of the first and largest spike in the receiver function (the direct P wave) followed by convolution of this partial one-spike receiver function with the vertical component seismogram and subtraction of the product from the horizontal to yield the residual part of the horizontal seismogram to be iteratively made consistent with the progressively updated receiver function. Thus, after the first iteration there exists a synthetic receiver function containing only one spike corresponding to the direct P arrival, and a new

radial seismogram short of the direct P arrival. The procedure is repeated to estimate other subsequent spike lags and amplitudes, each adding an additional spike in the receiver function till the misfit between the radial and the convolved product of the vertical and the spike train which is the desired receiver function, is reduced to an insignificant value.
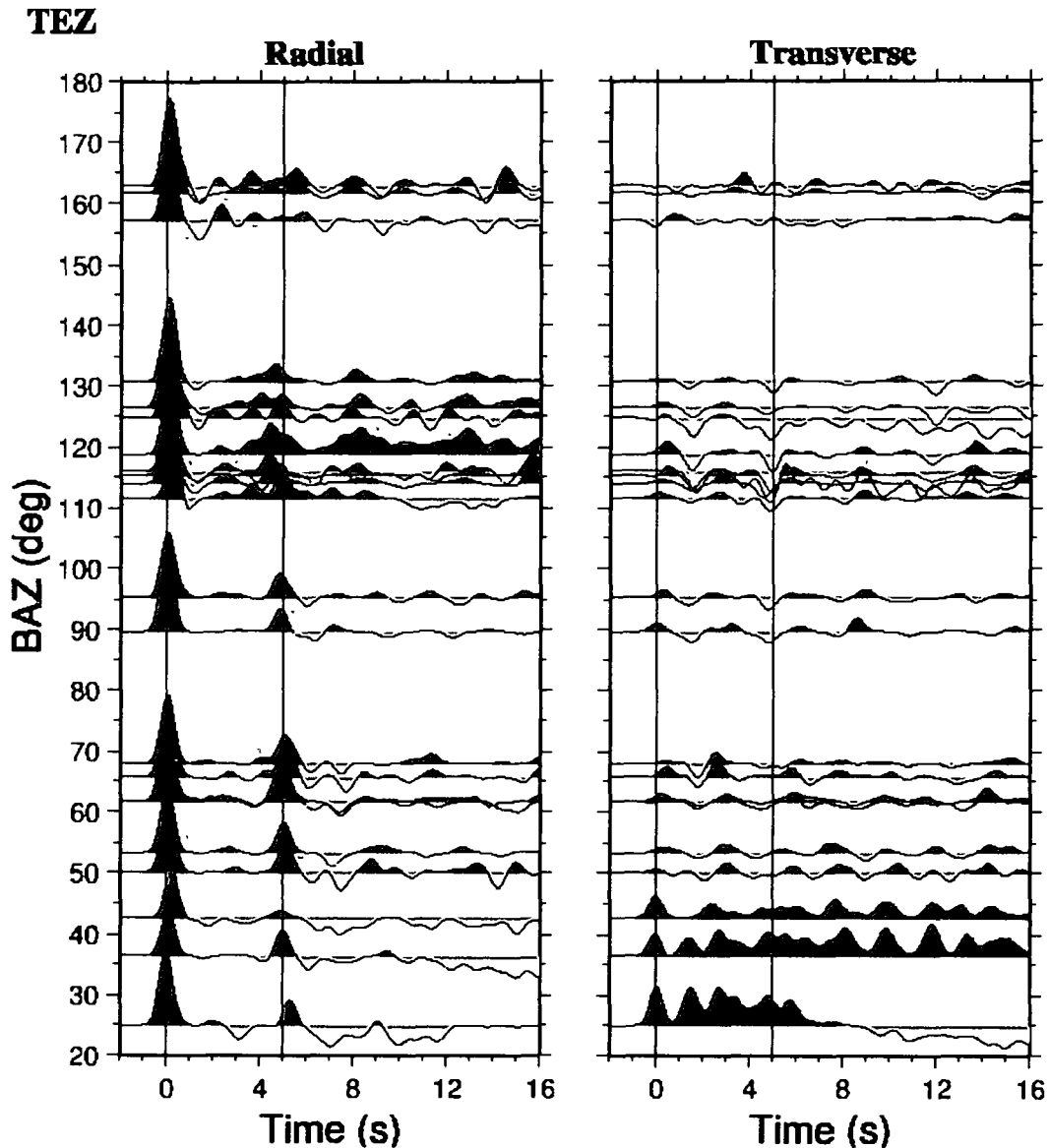
Figure 3.5: Azimuthal variation of the radial and transverse components of the teleseismic receiver functions at TEZ. The Moho converted Ps arrivals are clearly seen on radial component of the receiver function at about 5±0.25 s after the direct P-wave. Backazimuth (BAZ) is plotted from 20-180 degrees as all the events recorded at TEZ are from this BAZ range.

As stated above, earthquake events used for receiver function analysis at a site must meet several requirements. They should be distant enough so that the incidence angle of the emergent wave is fairly steep (~20°) rendering the vertical Earth Response function a near identity and the separation of the P and S arrivals long enough not to interfere with those of the Moho and mantle converted phases and their multiples. However, they should not be too distant so that the emergent waves skirt the core-mantle boundary thereby obviating the sub-mantle converted phases. Accordingly, the source-receiver great-circle arc length is chosen to be greater than 30° but less than 90°. For each event of magnitude greater than 5.5, a 90 second time window centered on the direct P arrival is selected and receiver functions calculated using the iterative, time-domain deconvolution approach (Ligorria and Ammon, 1999). Receiver functions thus obtained are further screened by polarization analysis to retain only those for further analysis which had a misfit of 10% or less. The Gaussian width used throughout this study was set to 2.5 which corresponds to the application of a 1.2 Hz low pass filter to the seismograms and allows a minimum resolvable wavelength of $\lambda = \pm 3.08$ km for an average crustal shear wave velocity of 3.7 km s^{-1}. Since the minimum resolvable length scale is $\lambda/4$, only model features larger than 0.77 km are resolvable. In order to enhance their signal to noise ratio by coherent stacking, receiver functions were further classified according to azimuth and distance and closely similar ones within narrow bins of a few degrees, stacked to produce the representative receiver function for the site corresponding to the mean distance and azimuth of the bin along with their ± 1 standard deviation bounds. Observing the stacked receiver function within its bounds qualitatively enables identification of its significant features with arrivals of a seismic phase. Figure 3.5 shows a suite of radial and tangential components of P-wave receiver functions for Tezpur (TEZ), in respect of waves arriving from different azimuths, plotted in ascending order. These clearly show the appearance of the Moho converted Ps phase at about 5 ± 0.05 s after the direct P-wave. Clear intra-crustal arrivals between the direct P and the Moho converted Ps phase in both the radial and

tangential receiver functions indicate the presence of a significant intra-crustal feature beneath the site. Two stacked radial and transverse receiver functions, in respect of back azimuth events from 50° to 68° and epicentral distance of 35° to 52°, recorded at TEZ are shown in Figure 3.6. This radial stack was inverted to model the shear wave variations with depth beneath TEZ.
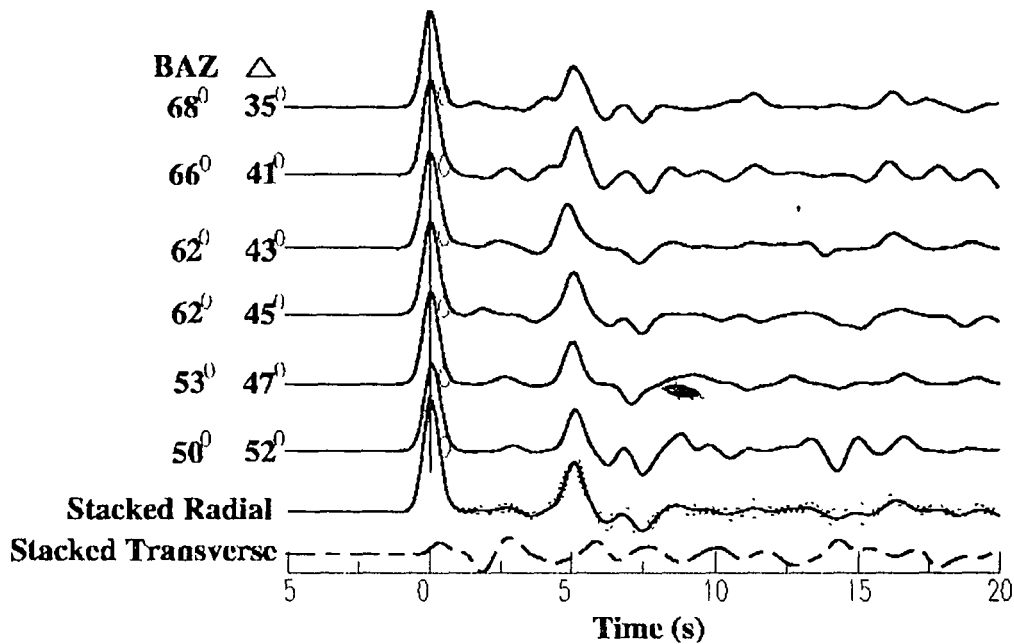
Figure 3.6: TEZ receiver functions for a back-azimuth bin of 50° - 68° and a great circle arc distance bin of 35° - 52°. The averaged radial and tangential receiver functions with ±1 standard deviation bounds for the radial are plotted beneath the individual radial receiver functions.

3.3.2. Vp/Vs Ratio and Moho Depth

As continents are characterized by large lateral variations in the thickness and composition of their crust, further insights into their structures can be gained by characterizing the materials at different depths beneath a seismometer station by the value of their Poisson's ratio, a characteristic rock property,

which can be calculated from the ratio between Vp and Vs. The thickness H and average Vp/Vs of the crust can both be estimated from the relative timing of the Ps conversions and their multiples (Zandt et al. 1995; Zhu & Kanamori, 2000). For example, the Ps-Pp time difference is dependent on the crustal thickness, the average crustal velocity and the Vp/Vs value. The two leg P-wave multiple PpPms is the phase that reflects off the surface then converts to an S-wave on reflection from the Moho, and travel-time difference between this P-multiple and Ps is simply the two-way P wave travel time through the crust. The two leg S-wave multiple is composed of two kinematically similar waves, PpSms+PsPms, which have identical travel times in a uniform layer, and the travel time difference between this S multiple and the direct P-wave is the two-way S wave travel time through the crust. The ratio of the Ps-Pp and PpPms-Ps time is independent of crustal thickness but weakly dependent on Vp. On the other hand, the ratio of the PpPms-Ps and (PpSms+PsPms)-Pp time is proportional to Vp/Vs and independent of crustal thickness (Zandt et al., 1995). Thus by considering the fact that the travel times of converted phases and their reverberations depend on average P-wave velocity, the radial component of a P-wave receiver function can be used to determine the average Vp/Vs as well as the thickness of the crust for a chosen value of the average P-wave velocity in the crust that may be available from other geophysical observations in the region (Zandt et al., 1995; Zhu and Kanamori, 2000). This analysis procedure is illustrated below:

If t_{p_s} and t_{p_p} denote the time of arrivals of the Moho converted Ps and the direct P phases respectively, one can write:

$$t_{p_s} - t_{p_p} = H[(Vs^{-2} - p^2)^{\frac{1}{2}} - (Vp^{-2} - p^2)^{\frac{1}{2}}]$$

(3.7)

where H is the crustal thickness with average velocities Vp and Vs and p is the ray parameter, related to the angle of incidence i by $p = \sin(i)/V$.

The travel-time difference between the P-multiple and Ps is simply the two-way P wave travel time through the crust for a ray with the ray-parameter p and is given by

$$t_{P_p P_{ms}} - t_{P_s} = 2H[(V_s^{-2} - p^2)^{\frac{1}{2}}]$$
(3.8)

The two leg S-wave multiple (called S-multiple) is composed of two kinematically similar waves, PpSms+PsPms, which have identical travel times in a uniform layer, and the travel time difference between this S multiple and the direct P-wave is the two-way S wave travel time through the crust is:

$$t_{P_s P_{ms} + P_p S_{ms}} - t_p = 2H[(V_s^{-2} - p^2)^{\frac{1}{2}}]$$
(3.9)

From the above equations, it is clear that the ratio of the Ps-Pp and PpPms-Ps time is independent of crustal thickness but weakly dependent on Vp, and the ratio of the PpPms-Ps and (PpSms+PsPms)-Pp time is proportional to the Vp/Vs ratio and independent of crustal thickness (Zandt et al., 1995). However, the signature of Vp/Vs values on the observed arrival times of converted phases and multiples is not immediately apparent. These arrivals are modified by the combined effect of 3 distinct crustal parameters: the average P-wave velocity in the crust, Vp/Vs and the crustal thickness H. Fortunately, they can be separately estimated by exploiting their different contributions to the arrival times of specific multiples. This is accomplished by using a special stacking procedure developed by Zhu and Kanamori (2000). The methodology exploits the fact that the arrival times and amplitudes of specific Moho converted phases and multiples appearing on receiver functions, are each determined by known functions of the Moho depth, H, Vp/Vs and the average Vp in the crust. For a near true combination of H and Vp/Vs value, the quantity R defined as the weighted sum of the receiver function amplitudes at the calculated times of arrivals of Ps, PpSs and PpSs + PsPs phases would be expected to be a maximum:

$$R = W1 * t_{p_s} + W2 * t_{p_p p_s} - W3 * t_{p_p s_s + p_s p_s} \qquad (3.10)$$

where the weights W1, W2 and W3 (0.7, 0.2 and 0.1 respectively) attached to the various multiples are progressively decreased according to their distance from the Ps phase in consideration of their reduced energies and thereby lower resolution. Eventually, the accuracy with which these two parameters are determined critically depends on the strength of the crustal multiples generated at the Moho.
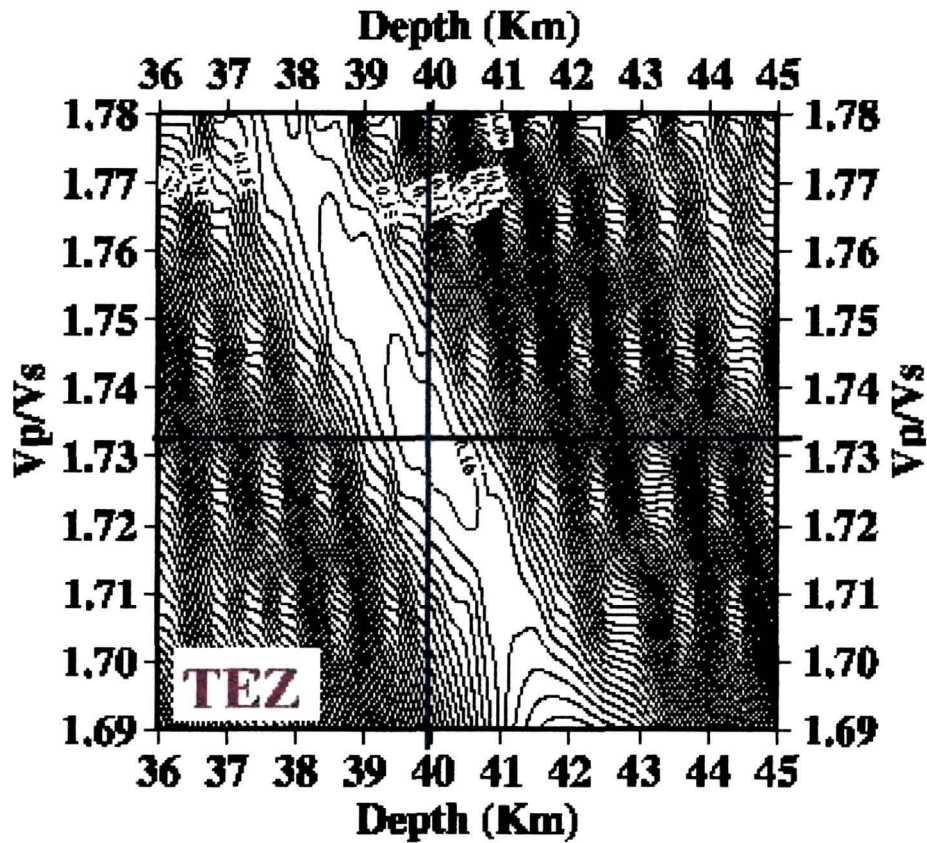
Figure 3.7: Showing contours of the weighted sums of the receiver function amplitudes at the calculated times of arrivals of the Ps phase and its multiples as the measure of mismatch between the observed Ps time series and those calculated for various pairs of values of Vp/Vs and crustal thickness H for Tezpur (TEZ), for an assumed average crustal Vp = 6.45 km/s. The best estimates of Vp/Vs and H are marked by the blue cross lines.

In this study, depth to the Moho and average crustal Poissons ratio beneath each of the stations in NE India were obtained by converting the time series Receiver Functions into the H-Vp/Vs domain (Zandt, et al. 1995, Zhu and Kanamori, 2000), by weighting the Ps, PpPms and PpSms+PsPms phases by 0.7, 0.2 and 0.1 respectively. Figure 3.7 shows the estimates of Vp/Vs and Moho depth for Tezpur (TEZ).

3.3.3. Crustal Structure: Joint Inversion of Receiver Functions and the Surface Wave Data

The combined sensitivity of teleseismic P-wave receiver functions and surface wave dispersion data to the shear wave speed structure of the upper earth layers is now routinely exploited to supply constraints on the crustal and upper mantle geology. Receiver function analysis allows modeling of the 1D structure beneath a seismometer station, yielding a spot velocity depth function characterizing the underlying earth. This method relying on the sharpness of converted phases highlights abrupt changes in the shear wave speed with depth but is insensitive to absolute velocities which must, however, be prescribed with some reliability to initiate the inversion of receiver functions. This requirement makes the receiver function inverted model strongly influenced by the prescribed initial velocity model. On the other hand, phase and group velocity information derived from surface wave data is sensitive to the average absolute shear wave velocity structure over the whole sampled region but has poor interface resolving power. Joint inversion of receiver functions with surface wave dispersion data over the area by offsetting the shortcomings of either of these when used alone, thus opens the possibility of determining the crustal shear wave speed structure with greater reliability. A velocity model which satisfactorily fits both the relevant surface wave and receiver function information will therefore yield a velocity structure relatively unbiased by the choice of the initial model for inverting

the reveiver function thereby producing a more reliable image of the subsurface. However, to combine receiver function and dispersion data, the vertical and lateral extent of the area sampled by both data sets must be similar, otherwise one would be merging structural attributes that may be incommensurate. Rayleigh wave dispersion measurements provide source-receiver path average group velocity variations with frequency. These 1D measurements sampling a region are combined to form group velocity variation maps using tomographic inversion (Gobarenko & Yanovskaya, 1984; Snieder, 1996; Mokhtar et al., 2000). Depending on the parametrization of the final model obtained from inversion, localized group velocity dispersion can be extracted corresponding to each receiver station. These localized dispersion curves are then jointly inverted with receiver functions for every seismograph site. The joint inversion technique is based on the least squares problem in terms of eigenvalues and eigenvectors and uses the Singular Value Decomposition (SVD) approach to invert the Green's Function matrix yielding the model vector. The model vector is parametrized by shear speeds in a stack of subsurface layers of equal thickness. The variance-covariance matrix and the resolution matrix are also generated in the process to evaluate the quality of the solution. The mathematical formulations are discussed in details by Julia et al (2000). The algorithm and computer programs used for the analysis are documented in Herrmann (2003). A quick overview of the procedure is given below.

To perform the joint inversion of the receiver functions and surface wave dispersion curves, we seek the earth model that minimizes the joint prediction error defined as:

$$E_{v/z} = \frac{1-P}{N_1} \sum_{i=1}^{N_1} \left[\frac{y_i - \sum_{j=1}^{M} Y_{ij} x_i}{\sigma_{y_i}} \right]^2 + \frac{P}{N_z} \sum_{i=1}^{N_z} \left[\frac{z_i - \sum_{j=1}^{M} Z_{ij} x_j}{\sigma_{z_i}} \right]^2 \qquad (3.15)$$

where y could be the residual dispersion curve, Y could the partial derivative matrix and x the shear velocities for a given set of plane layers with fixed thicknesses, and the z could be the residual receiver function and Z could be the partial derivative matrix. Ny and Nz represent the number of data points for each data set and σ_y^2 and σ_z^2 are corresponding variances, assuming the data points to be statistically independent. Parameter P controls the influence of receiver function and surface wave data sets on minimization procedure. For P=0, the solution is only affected by the receiver function data set and ignores the surface wave data completely. On the other hand, P=1 gives a solution which is derived only from the surface wave data sets.

In practice, the minimization procedure described above in equation (3.15), is implemented through the following weighted systems of equations:

$$
\begin{pmatrix}
\alpha_1 y_1 \\
\vdots \\
\alpha_{N_y} y_{N_y} \\
\beta_1 z_1 \\
\vdots \\
\beta_{N_z} z_{N_z}
\end{pmatrix}
=
\begin{pmatrix}
\alpha_1 Y_{11} & \alpha_1 Y_{12} & \cdots & \alpha_1 Y_{1M} \\
\vdots & \vdots & \ddots & \vdots \\
\alpha_{N_y} Y_{N_y 1} & \alpha_{N_y} Y_{N_y 2} & \cdots & \alpha_{N_y} Y_{N_y M} \\
\beta_1 Z_{11} & \beta_1 Z_{12} & \cdots & \beta_1 Z_{1M} \\
\vdots & \vdots & \ddots & \vdots \\
\beta_{N_z} Z_{N_z 1} & \beta_{N_z} Z_{N_z 2} & \cdots & \beta_{N_z} Z_{N_z M}
\end{pmatrix}
\begin{pmatrix}
x_1 \\
x_2 \\
\vdots \\
\vdots \\
\vdots \\
x_m
\end{pmatrix}
\qquad (3.16)
$$

where $\alpha_i^2 = \dfrac{1-P}{N_y \sigma_{y_i}^2}$, $\beta_i^2 = \dfrac{P}{N_z \sigma_{z_i}^2}$.

However, the data contain uncertainties because of noise, which may be characterized by means of a variance-covariance matrix. For the weighted system defined in equation (3.16), the variance-covariance matrix becomes

$$
[\mathrm{cov}\, y\,|\,z] =
\begin{pmatrix}
\dfrac{1-P}{N_1} & \cdots & 0 & 0 & \cdots & 0 \\
\vdots & \ddots & \vdots & & \vdots & \ddots & \vdots \\
0 & \cdots & \dfrac{1-P}{N_1} & 0 & \cdots & 0 \\
& & & \dfrac{P}{N_2} & & \\
0 & \cdots & 0 & \dfrac{P}{N_2} & \cdots & 0 \\
\vdots & & & & \ddots & \vdots \\
0 & \cdots & 0 & 0 & \cdots & \dfrac{P}{N_z}
\end{pmatrix}
\qquad (3.17)
$$

These uncertainties translate into uncertainty in the model parameter estimations as they propagate through the inverse operator to the model space. The variance-covariance matrix that characterizes the uncertainties in the model parameter, [cov x] can be estimated from

$$
[\mathrm{cov}\, x] = G^{-g}.[\mathrm{cov}\, y\,|\,z].G^{-gt}
\qquad (3.18)
$$

where G is the $\left[(N_1 + N_2) \times M \right]$ matrix in equation (3.16) (Menke, 1984). Thus, the joint inversion technique expresses the least squares problem in terms of eigenvalues and eigenvectors and uses singular value decomposition to invert the matrix yielding the model vector which is parameterized by shear speeds in a stack of subsurface layers of equal thickness.

While inverting the observed data, the velocity structure is represented by a set of flat lying homogeneous isotropic velocity layers of equal thickness, whilst the layer velocity is free to be adjusted. In this study, the starting velocity model comprised velocity layers that were 1.5 to 2.0 km thick with a half-space below 70 km. The starting shear wave speed was set equal to Vs=4.7 km/s for every layer in the model which equates with the upper mantle velocities. This was so chosen in order to provide a check on how well the dispersion data could eventually constrain the inverted velocities despite the starting model having no resemblance to the real earth, thereby demonstrating that the final results were free from possible bias in the a-priori

information so introduced The P-wave velocity Vp was calculated directly from Vs according to the following relationship:

$$\frac{Vp}{Vs} = \left[\frac{2(1-\sigma)}{(1-2\sigma)}\right]^{\frac{1}{2}}$$ (3.19)

where σ is the Poission's ratio. The finely parameterized model was first inverted to determine the depth to the Moho and identify mid-crustal interfaces, if any. Then, adjacent model layers with similar wave speeds were stacked to form a more coarsely parameterized velocity model and the new model was used as the starting model in the next iteration. This procedure was repeated til we got a velocity model with the minimum number of parameters that fit the main features on the receiver function besides satisfying the surface-wave data at the same time. Forward modeling was then carried out to estimate how well the main features of the crustal model were constrained by inverting the receiver function and surface-wave data by adding and removing features obtained from the inversion as shown in Figure 3.9.

The Frequency-Time-Analysis (FTAN) of Levshin et al. (1992) was employed for measurement of fundamental mode Rayleigh waves on the vertical component seismogram. In this technique group velocity is computed from the distance between the preliminary determination of epicenter location and the receiver and the group arrival time. Detailed description of the method and analysis procedure is extensively discussed by Levshin et al. (1992). Fundamental mode Rayleigh Wave Group velocity dispersion data for each station in the northeast India was taken from Mitra et al. (2006) between 15s and 45s period (Figure 3.8) where it is most sensitive to crustal S-wave velocities.
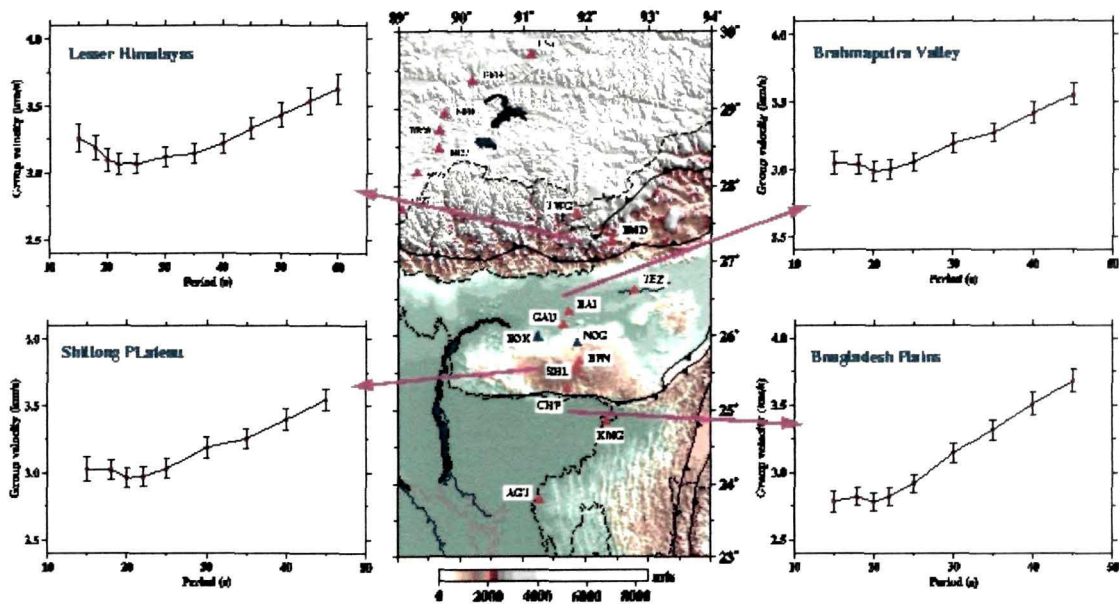
Figure 3.8: Fundamental mode Rayleigh Wave Group velocity dispersion from the four different regions across NE India.

Figure 3.9 summarises the inversion result for the crustal velocity structure at TEZ based on the receiver function stack with a mean back-azimuth of 59°. This stack contains 6 events with the epicentral distance range from 50° - 68°. The tangential signal observed over this back-azimuthal range is small and both the radial and tangential stacks have a high signal-to-noise ratio as evidenced by the small ±1σ bounds. The inversion model thus obtained for TEZ indicates a two-layer crust consisting of an upper layer of 11±2 km thickness underlain by a lower crust of thickness 29±1 km with average crustal shear-wave velocity Vs 3.57±0.2km/s.
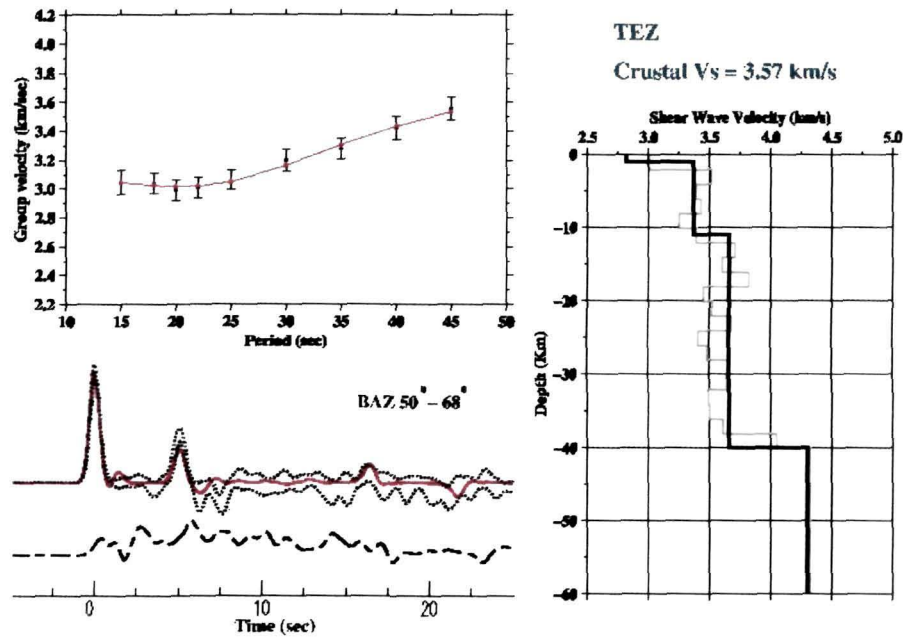
Figure 3.9: Joint inversion results for Tezpur (TEZ). (left) Synthetic dispersion and receiver function (red) are plotted within the error bounds of dispersion and ±1 SD bounds of Receiver Functions respectively calculated from the thick-layer(bold line) model shown in the right. In the velocity model the thin line represents the thinly parametrised model while the bold line represents the coarsely parametrised velocity model.

3.4 Anisotropy in the Crust: Analysis of Ps Splitting

Moho converted Ps splitting has been used for determination of the crustal anisotropy parameters by many authors (e.g. McNamara and Owens, 1993). Routine measurements of shear wave splitting yield high-lateral resolution estimates of the polarization of the fast wave (ϕ) and of the delay time (δt) between fast and slow waves. When the anisotropy and path length are both large or the frequency is high, δt may be greater than the pulse duration, and the two split phases may be completely separated. One direct method for

determination of ϕ and δt, is to rotate the horizontal seismograms to various azimuths (e.g., Ando et al., 1983). When the seismograms have been rotated to fast and slow directions, the first shear arrival is seen entirely on the fast component, and the second shear arrival follows on the slow component at a time δt after the first arrival. Bowman and Ando (1987) used polarization diagrams to determine the polarization of the fast shear wave, then rotate the seismograms to fast and slow direction, and perform a cross correlation between the fast and slow components to determine the time separation as the time that gives the maximum cross correlation. Polarization diagrams and plots of fast and slow components are used as diagnostics, to assure that ϕ and δt have been correctly identified.

Accordingly, a cross-correlation technique (Browman and Ando, 1987; McNamara and Owens, 1993; Tong et al., 1994; Herquel et al., 1995) was used in this dissertation to determine the split-time and the azimuth of the symmetry axis of anisotropy responsible for splitting of the Ps phases and thereby the anisotropy in the crust beneath northeast India stations. The technique exploits the fact that in the fast-slow coordinate system, the components of the split Ps phase will be almost similar since they are generated by the same parent phase. This was analysed by incrementally rotating the two orthogonal components of the receiver functions from -90° to 90° in steps of 2° at a time and their cross-correlation coefficients calculated for time lags of -0.5 to +0.5 s in steps of 0.01 s. The analysis window was chosen manually ranging from approximately ±2 s about the Moho converted Ps phase. The correlation is the maximum in the fast-slow coordinate system (McNamara and Owens, 1993).

An example of splitting in the Moho converted Ps phase recorded at TEZ and the corresponding particle motions before and after the correction for anisotropy is shown in Figure 3.10.

(a)

(b)   **(c)**

(d)
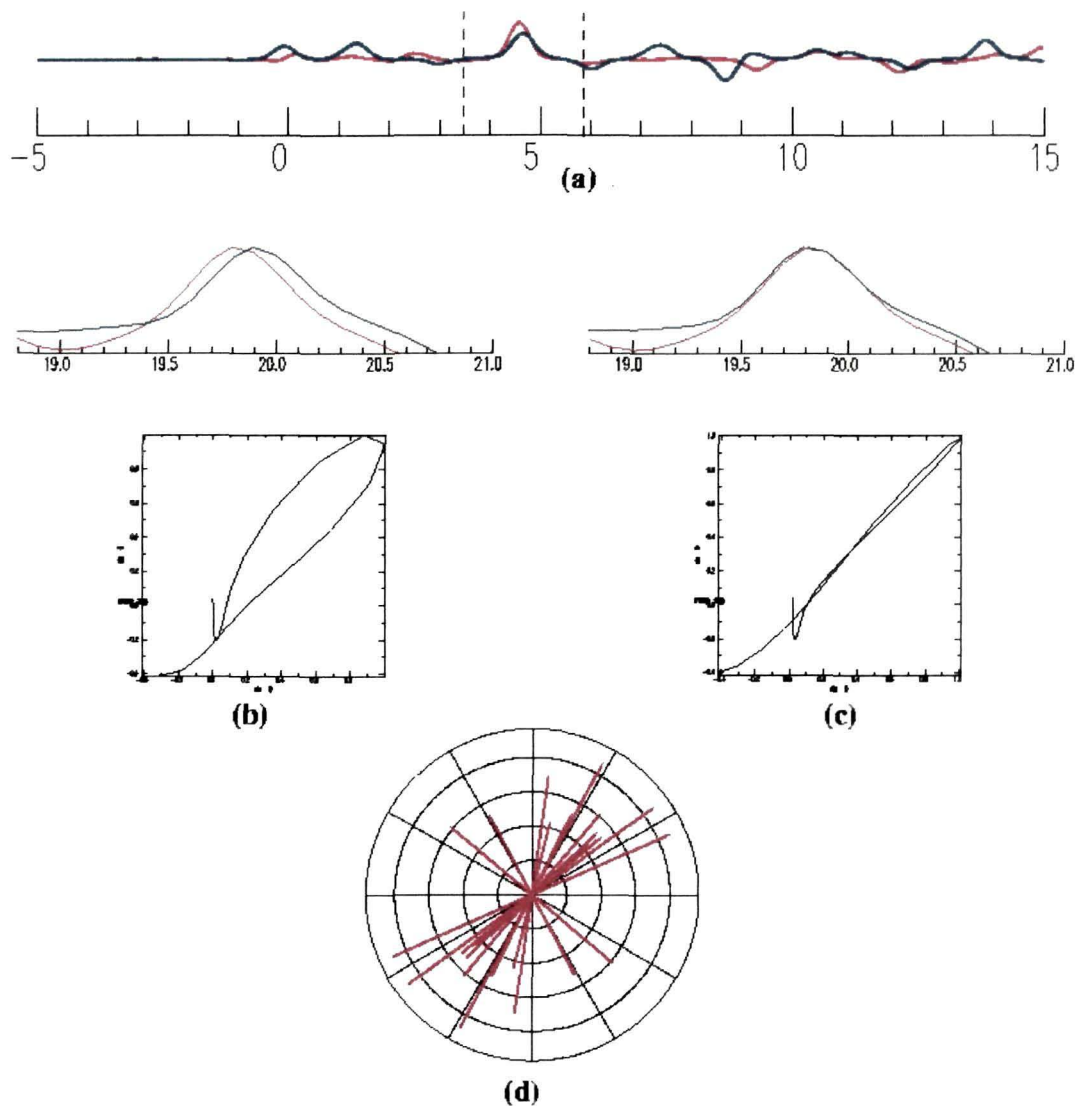
Figure 3.10: (a) Splitting of Moho converted Ps phases observed in the radial and tangential components of the receiver functions recorded at TEZ. (b) Uncorrected radial and tangential receiver functions with the corresponding particle motion diagram for the window length considered for the analysis. (c) Corrected radial and tangential receiver functions with the corresponding particle motion diagram for the window length considered for the analysis and (d) observations of splitting from various directions is shown in the rose diagram.

Chapter 4

Crustal structure of NE India constrained by P-wave Receiver Function and Surface Wave Dispersion Data

4.1 Perspective

The first images of the crustal structure of northeastern India were constructed by Mitra et al. (2005) from inversion of Receiver Functions calculated for 15 sites including the permanent Chinese Digital Seismic Network (CDSN) station at Lhasa, the six INDEPTH II stations for which broadband data were obtained from the IRIS data centre, as well as 8 sites within the region (Figure 4.1: blue triangles) at which such data were specially generated by the authors. Partly, these earlier data sets had been re-inverted jointly with surface wave dispersion data by Sinha (2007). This chapter presents the results of joint inversion along the entire profile of Mitra et al (2005) and further extends the crustal image of the region using data generated at 7 new sites (Figure 4.1: red triangles) located in the great Himalya, the Bengal basin as well as off profile sites on the Meghalaya plateau and Mikir Hills.

The rationale for joint inversion of receiver function and surface wave dispersion data follows from the possibility of offsetting the likely bias introduced in the inverted estimates using the receiver function alone. For,

whilst receiver function inversion is sensitive to discontinuities in the shear wave speed structure of the crust signifying acoustic impedance contrasts, it is insensitive to absolute values of shear wave speeds. On the other hand, phase and group velocity information derived from surface wave dispersion data, are sensitive to the average absolute shear wave speeds over the entire sampled region but has poor interface resolving power. To further refine the earlier crustal model, therefore, P-wave receiver functions for each site were jointly inverted with the Rayleigh wave group velocity data of Mitra et al. (2006) which have since become available. The sources of data used for analysis presented in this chapter, together with site descriptions of seismic stations are described in chapter 3 section 3.1.

4.2 Receiver Function Analysis

Among the various seismic imaging tools used for analysis, that using Receiver Functions is based on the inversion of converted seismic phases (P-to-S) generated by a steeply incident P-wave heading towards the recording site. These P to S converted phases are generated as the P-wave heading to the surface encounters seismic discontinuities along its journey in the underlying crust and upper mantle. To isolate these much weaker shear-wave converted phases and multiples on the horizontal components of P-waveforms- the seismogram segment appearing between the onset of P and S waves- we deconvolve the vertical component of ground motion from the radial and transverse component waveforms (Ammon, 1991). The resulting time series constitute the radial and tangential components of the receiver functions respectively. For northeastern India stations, the most stable receiver functions were obtained using the iterative time-domain deconvolution method of Liggoria and Ammon (1999). This method was accordingly, used for all the analyses presented in this dissertation.
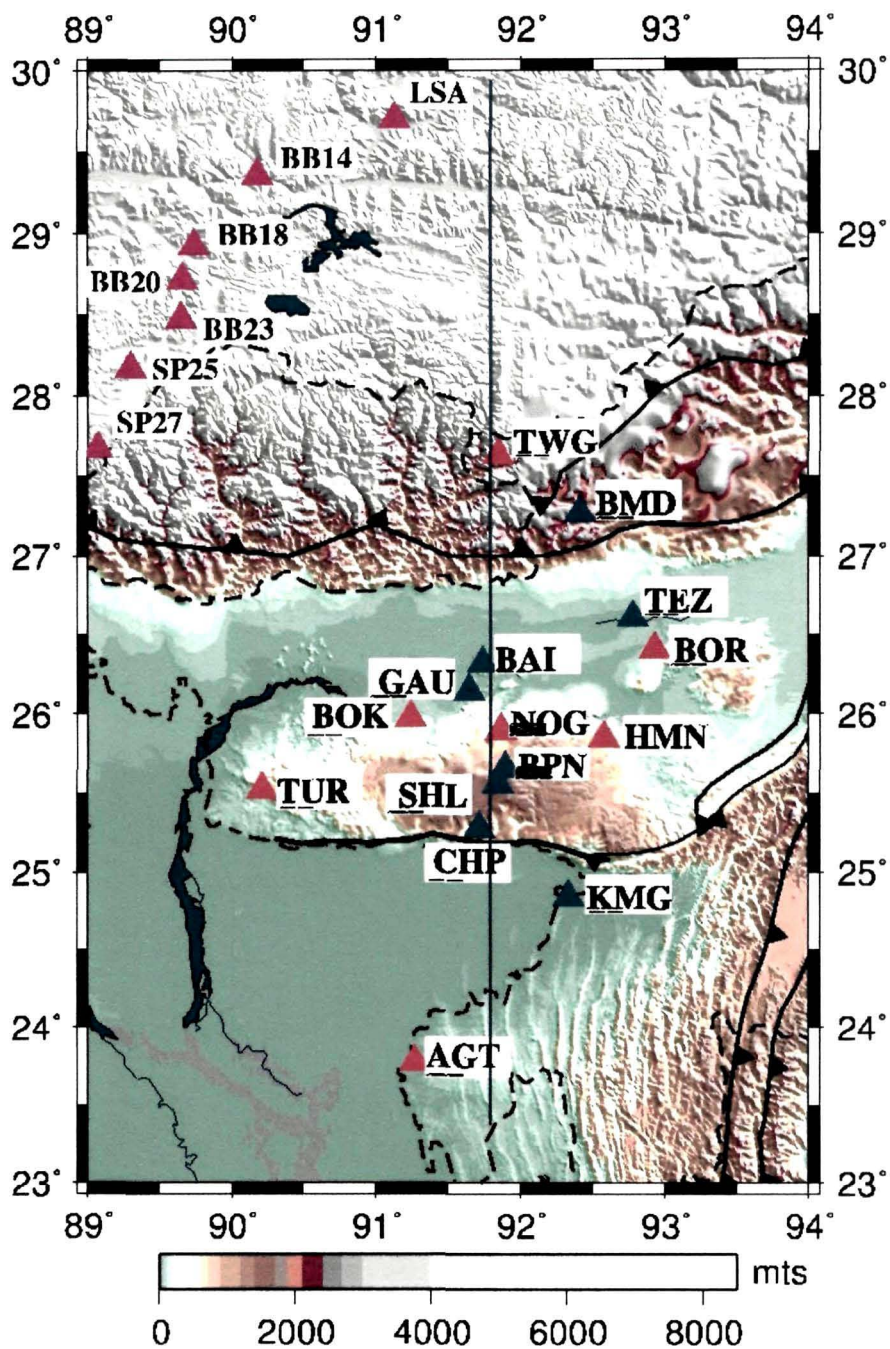
Figure 4.1: Topographic map of Northeast India and southern Tibet, showing the location of broadband seismic stations: blue and purple (the INDEPTH II stations) triangles mark the site for which receiver functions were calculated by Mitra et al. (2005)., red triangles denote sites since added where additional data were generated for the present work.

Earthquake events used for receiver function analysis of the crustal structure beneath a site must meet several requirements. They should be distant enough so that i) the incidence angle of the emergent wave is fairly steep (~20°) justifying the assumption that the vertical Earth Response function may be treated as an identity and ii) the separation of the P and S arrivals long enough to capture the Moho converted phases but not those of mantle converted phases and their multiples. At the same time they should be near enough so that the emergent waves skirt the core-mantle boundary thereby obviating the sub-mantle converted phases. Accordingly, the source-receiver great-circle arc length was chosen to be greater than 30° but less than 90°. Accordingly, we isolated all high signal-to-noise ratio seismograms at each of the 22 sites pertaining to M ≥ 5.5 earthquakes located within the 30°-90° distance range and abstracted therefrom a 90 seconds long signal centered on the direct P arrival.

Receiver functions were calculated from all such pre-selected 3-component seismogram segments using the iterative, time-domain deconvolution approach (Ligorria and Ammon, 1999). This approach exploits the fact that the vertical ground motion waveform which is assumed to approximate to the P waveform incident at the base of the crust when convolved with the corresponding crustal receiver function should yield the horizontal (radial or transverse). One therefore proceeds to iteratively construct a spike train by minimizing the misfit between the observed horizontal seismogram and the convolution of the vertical seismogram with the iteratively constructed spike train. Receiver functions thus obtained were next screened to retain only those for further analysis which had a misfit of 10% or less. The Gaussian width used throughout this study was set to 2.5 which corresponds to the application of a 1.2 Hz low pass filter to the seismograms and allows a minimum resolving wavelength of $\lambda = \pm 3.08$ km for an average crustal shear wave velocity of 3.7 km s^{-1}. This allows resolution of model features larger than 0.77 km allowing for the minimum resolvable length scale to be $= \lambda/4$. In

order to enhance their signal to noise ratio by coherent stacking, receiver functions were further classified according to azimuth and distance and closely similar ones within narrow bins of a few degrees, stacked to produce the representative receiver function for the site corresponding to the mean distance and azimuth of the bin. The stacking also allowed evaluation of their ±1 standard deviation bounds.

The procedure followed for the analysis of receiver functions and their joint inversion with surface wave dispersion data was identical for each of the 15 sites. It is therefore considered instructive to discuss one of these in detail: the site at Tezpur (TEZ). Results for other sites were obtained in a similar fashion and are synthesized in the last section.

4.2.1 Receiver Function Analysis of Seismograms Recorded at Tezpur

Receiver functions were calculated for all the high quality seismograms recorded at TEZ of events larger than M 5.5 lying within the epicentral distance range of 30° to 90°, and a Gaussian width of 2.5. Figure 4.2 shows the radial and tangential components of the P-wave receiver functions for TEZ, ordered according to azimuth. The Moho converted P-to-S phases from the back azimuth range of 25° - 163° are clearly seen arriving at ~ 5±0.25 s after the direct P.

TEZ
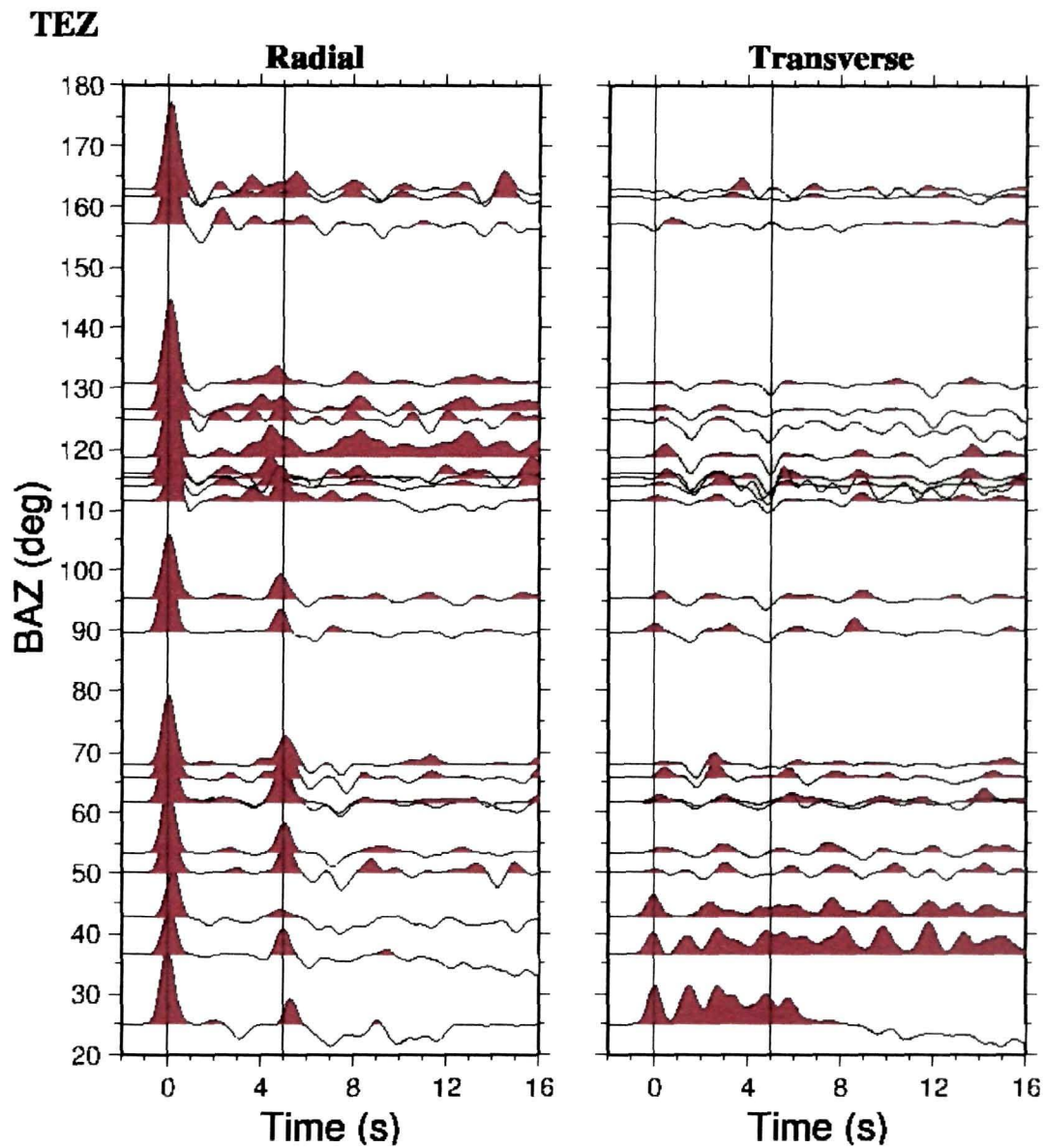
Figure 4.2 Azimuthal variations of the radial and transverse components of teleseismic receiver functions at TEZ. The Moho converted Ps arrivals are clearly seen on radial components of the receiver functions at about 5±0.25 s after the direct P-wave.

To enhance the signal-to-noise ratio, receiver functions pertaining to events from the backazimuth range of 50° – 68° and lying within the epicentral

distance range of 35° - 52°, were stacked and their ±1 standard deviation bounds calculated (Figure 4.3). These individual and stacked receiver functions, both, show a clear Ps arrival at about 5±0.25 s A downward pull is observed at about 2.0 s on the stacked transverse receiver function, most likely an indication of the presence of a low-velocity layer or seismic anisotropy underneath the station.
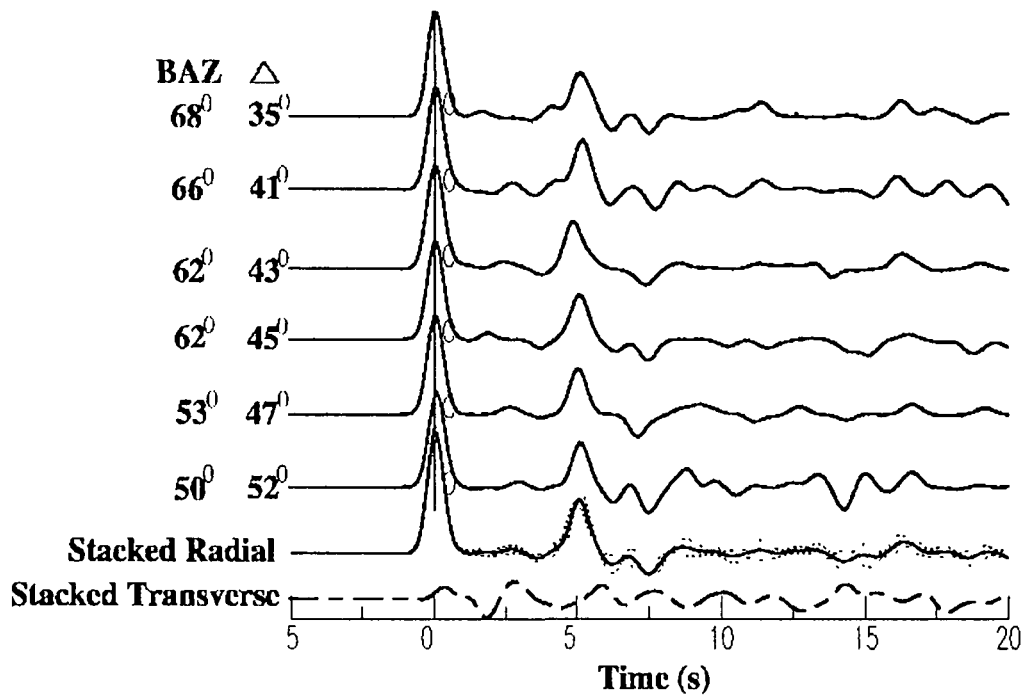
Figure 4.3 TEZ receiver functions from the back-azimuth bin of 50° - 68°. The averaged radial and tangential receiver functions with ±1 standard deviation bounds for the radial are plotted beneath the individual radial receiver functions.

4.2.2 Crustal Thickness and Vp/Vs Ratio for Tezpur

Since there is an inherent tradeoff between the crustal thickness H and the average Vp, it is desirable to constrain these quantities separately. To accomplish this we use the methodology proposed by Zhu & Kanamori (2000) which exploits the fact that for a given average Vp of the crust, arrival times of the various multiply reflected converted phases can be uniquely calculated for any given pair of values: the crustal thickness H and the ratio, Vp/Vs. Accordingly, one calculates for various credibly estimated values of average crustal Vp, the arrival times of the various multiply reflected converted phases for a suite of H and Vp/Vs values to constrain those for which the calculated and the observed Ps trains are maximally correlated. Thus, the Ps train in the Tezpur (TZP) receiver function time series was translated into a residual map representing the mismatch between the data derived receiver function and the one calculated for pairs of values of the crustal thickness H and Vp/Vs for the most credible value of Vp. Figure 4.4 shows a residual map in the H-Vp/Vs domain for a range of average Vp values (6.1 - 6.5 km/s) determined from previous studies. However, as the resolution of each succeeding conversion is expected to degrade progressively, we weighted the Ps, PpPms and PpSms+PsPms phases, respectively by 0.7, 0.2 and 0.1, as suggested by Zhu and Kanamori (2000). The best constrained values of crustal thickness H and Vp/Vs beneath TZP was thus estimated to be 40 km and 1.732 corresponding to an average crustal Vp speed of 6.1-6.4 km/s, with an estimated error of ~2 km and 0.02 km/s respectively and the ±1 standard deviation bounds of 0.5 km and 0.03 respectively.
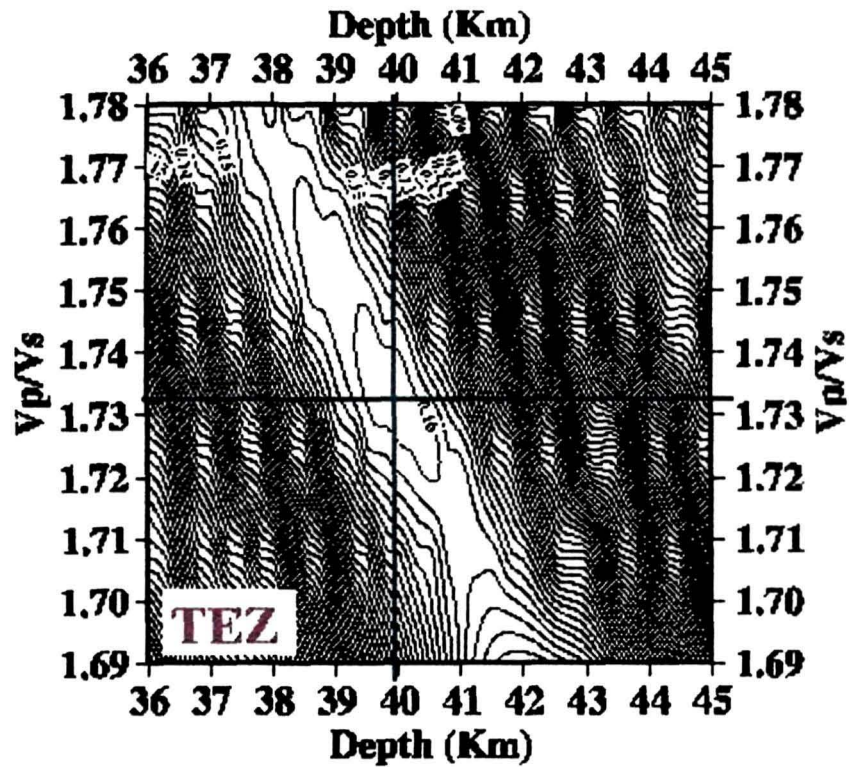
Figure 4.4: Showing contours of the weighted sums of the receiver function amplitudes at the calculated times of arrivals of the Ps phase and its multiples as the measure of mismatch between the observed Ps time series and those calculated for various pairs of values of Vp/Vs and crustal thickness H for Tezpur (TEZ), for an assumed average crustal Vp = 6.45 km/s. The best estimates of Vp/Vs and H are marked by the blue cross lines.

4.3 Joint Inversion of Receiver Function and Rayleigh Wave Dispersion Data at Tezpur

Crustal receiver function calculated for a site constitutes the observable that can be inverted to estimate the one-dimensional crustal shear wave speed structure beneath a seismometer station. This method is sensitive to

discontinuities in the shear wave speed structure of the crust but insensitive to absolute velocities, thereby rendering the inverted model susceptible to errors in the assumed shear wave speeds of the starting model chosen to initiate the inversion process. However, this undesired effect can to some extent be offset by requiring that in addition to minimizing the prediction error of a receiver function time series, the iteratively estimated inverse model of the crust simultaneously minimizes the prediction error in the surface wave dispersion time series if available for that area. Because the latter are sensitive to the average absolute shear wave speed structure of the larger region surrounding the site, this joint inversion of both the receiver function and surface wave dispersion data has the effect of constraining the final solution to be consistent with the average crustal speed structure of the region whilst simultaneously highlighting the crustal structure discontinuities through their proxy contrasts in the acoustic impedance characterizing the Ps wave train in the receiver function.

Accordingly, the P-wave receiver functions calculated for Tezpur (TEZ) were jointly inverted alongwith the Rayleigh wave group velocity data for this site (15s and 45s period) computed by Mitra et al. (2006), using the stochastic least squares approach of Hermann (2002). The method expresses the least squares problem in terms of eigenvalues and eigenvectors extracted by singular value decomposition to estimate the inverted model vector parameterized by shear wave speeds in a layered crust of equal thickness. The method also provides the variance-covariance matrix and the resolution matrix which enables evaluation of the quality of the solution.

Fundamental mode Rayleigh Wave Group velocity dispersion data for TEZ is taken from Mitra et al. (2006) between 15s and 45s period (Figure 4.5) where it is most sensitive to crustal S-wave velocities. The Frequency-Time-Analysis (FTAN) of Levshin et al. (1992) was employed for measurement of the fundamental mode Rayleigh waves on the vertical component seismogram. In

this technique group velocity is computed from the distance between the epicenter and the receiver and the group arrival time. A detailed description of the method and analysis procedure is extensively discussed by Levshin et al. (1992).
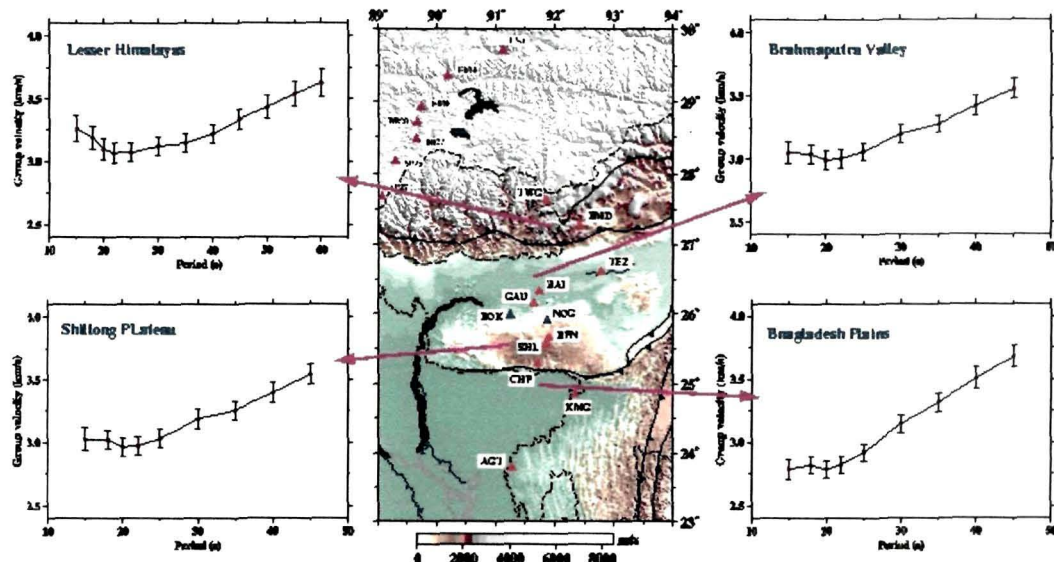
Figure 4.5: Fundamental mode Rayleigh Wave Group velocity dispersion curves from the four different regions across NE India.

The initial velocity model for the inversion process was parametrized as a stack of 1.5 to 2.0 km thick layers overlying a half-space, the shear wave speeds of each being 4.7 km/s. This initial model introduces little a-priory information to bias the inversion results. The iteratively adjusted models were then smoothed by merging layers with substantially similar speeds to create the next initial model and the process was repeated until the model matched the main features of the receiver function and also satisfied the surface wave data. Significant features of the crustal model so obtained were then intensively tested using forward modeling with controlled parametrization, i.e by addition and removal of layers or by changing their shear wave speeds.

Figure 4.6 summarizes the inversion result for shear wave speed structure of the TEZ crust based on the receiver function stack with a mean back-azimuth of 59°. This stack contains 6 events from an epicentral distance range from 50° - 68°. The tangential signal observed over this back-azimuthal range is small and both the radial and tangential stacks have a high signal-to-noise ratio as evidenced by the small ±1σ error limit. The inversion model thus obtained for TEZ indicates a two-layer crust consisting of an upper layer of 11±2 km thickness underlain by a lower crust of thickness 29±1 km with average crustal shear-wave speed Vs = 3.57±0.2km/s, the upper mantle shear wave speeds lying at a depth of 40±2 km.
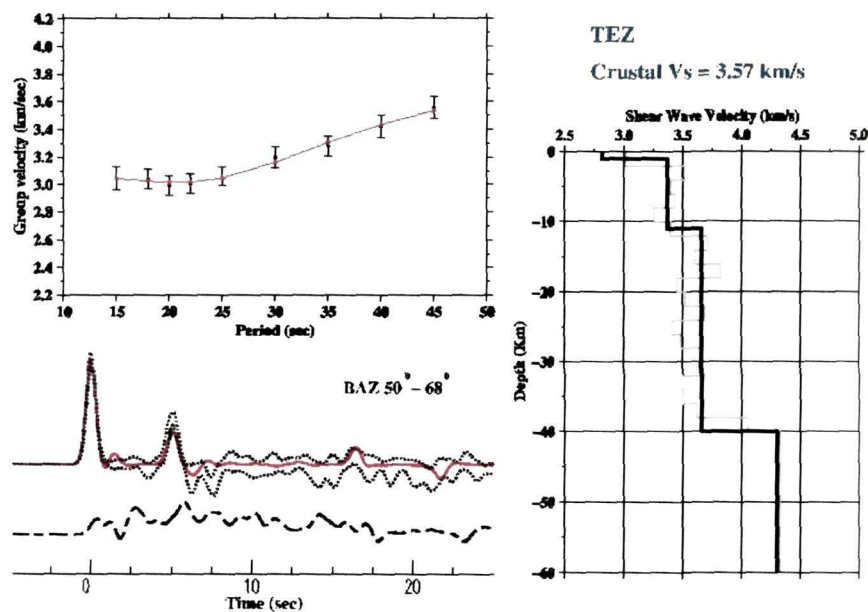
Figure 4.6: Joint inversion results for Tezpur (TEZ). (left) Synthetic dispersion and receiver functions (red) are plotted within the error bounds of dispersion and ±1 SD bounds of Receiver Functions respectively calculated from the model shown on the right.

Joint inversion results for the crustal shear wave structure at other NE India stations were determined in the same fashion as for TEZ described above and the results are synthesized in the next section.

4.4 Synthesis of Crustal Shear Wave Speed Structure in Northeast India

Receiver functions for all other stations along the SN profile, were calculated following an identical procedure as that described above for TEZ and duly corrected for the normal distance move out for the Moho Ps phase with reference to an epicentral distance of 67°. These have been plotted in Figure 4.7, ordered first according to distance from the southernmost site at Agartala and then according to backazimuth to enable direct comparison of the various features of the crust beneath the NE India region. Most of the radial receiver functions show significant coherent intra-crustal P-to-S converted phases arriving between the direct P and Moho converted Ps arrivals indicating a complex, multi-layered crustal structure beneath the region which is corroborated by the presence of significant amounts of seismic energy in the transverse receiver functions at least for the first few seconds. An account of the detailed analysis of the origin of the transverse energy is presented in the later sections.

Whilst the azimuthal distribution of teleseismic events is not good enough to accurately constrain the nature of the sub-receiver lateral heterogeneity at each of the sites, insightful information can yet be gained by making a qualitative trend analysis at each station by examining the migrated receiver functions which duly account for the difference in incidence angles at the base of the crust. The average crustal thickness and shear wave speed obtained from the joint inversion, using an appropriate velocity model were used to perform migrations for a single crustal layer above the Moho. Table 4.1 shows the average crustal velocities and Moho depths for the stations used for migration.

Table 4.1: Crustal thicknesses and shear velocities used for migration

Station	Average crustal thickness (km)	Average crustal velocity Vs (km/s)
AGT	39	3.60
KMG	38	3.56
CHP-S	44	3.58
CHP-N	37	3.49
SHL	35	3.54
BPN	34	3.52
NOG	33	3.52
BOK	35	3.56
TUR	35	3.65
GAU	40	3.55
BAI	40	3.56
TEZ	40	3.57
BOR	32	3.50
BMD	48	3.59
TWG	56	3.70

The thickness H and average Vp/Vs of the crust for each of the stations were estimated using the method explained in the earlier section for the records of Tezpur (TZP). Figure 4.8 shows the estimates of Vp/Vs versus the Moho depth H for five stations of the study area. A crustal Vp speed of 6.1-6.4 km/s, based on the results of previous geophysical studies (De and Kayal, 1990), was used for calculating H and average Vp/Vs. The estimated error in the Vp/Vs and crustal thickness over the range of the chosen P-wave speeds is ~0.02 and ~2 km respectively. The ±1 standard deviation bounds for the crustal thickness and Vp/Vs are 0.5 km and 0.03 respectively. In general, the results indicate a relatively thinner crust (~ 4 km) beneath the Shillong Plateau compared with those across its southern and northern margins both beneath the Bengal Basin and the Brahmaputra Valley.

RECEIVER FUNCTION PROFILE
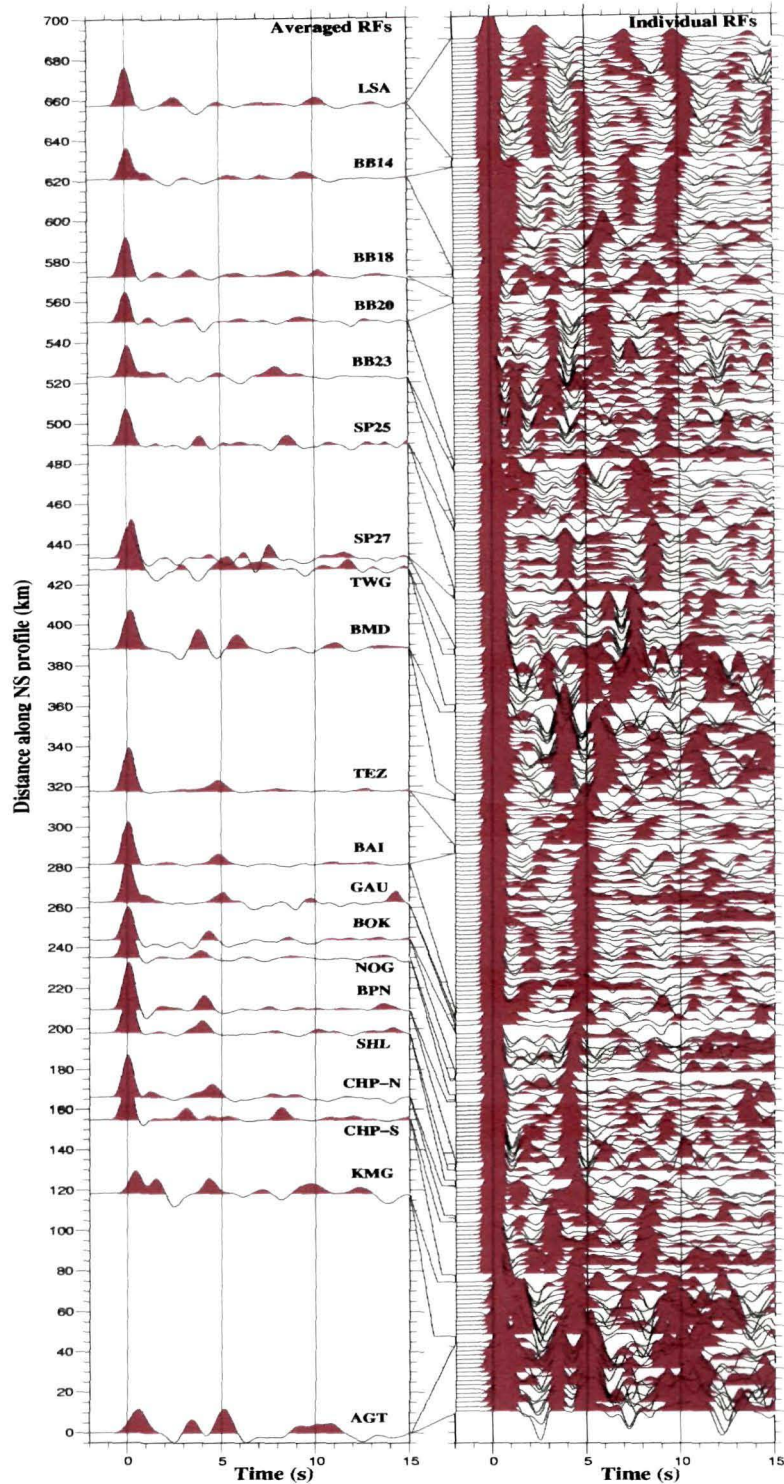
Figure 4.7: (Right column) Calculated Radial Receiver Functions (Ligorria & Ammon, 1999), duly corrected for the move out reference distance of 67° for each station are projected onto the N-S profile 91.7°E, and plotted first according to distance from Agartala and then according to azimuth. The average of the summed receiver functions are plotted on the left.
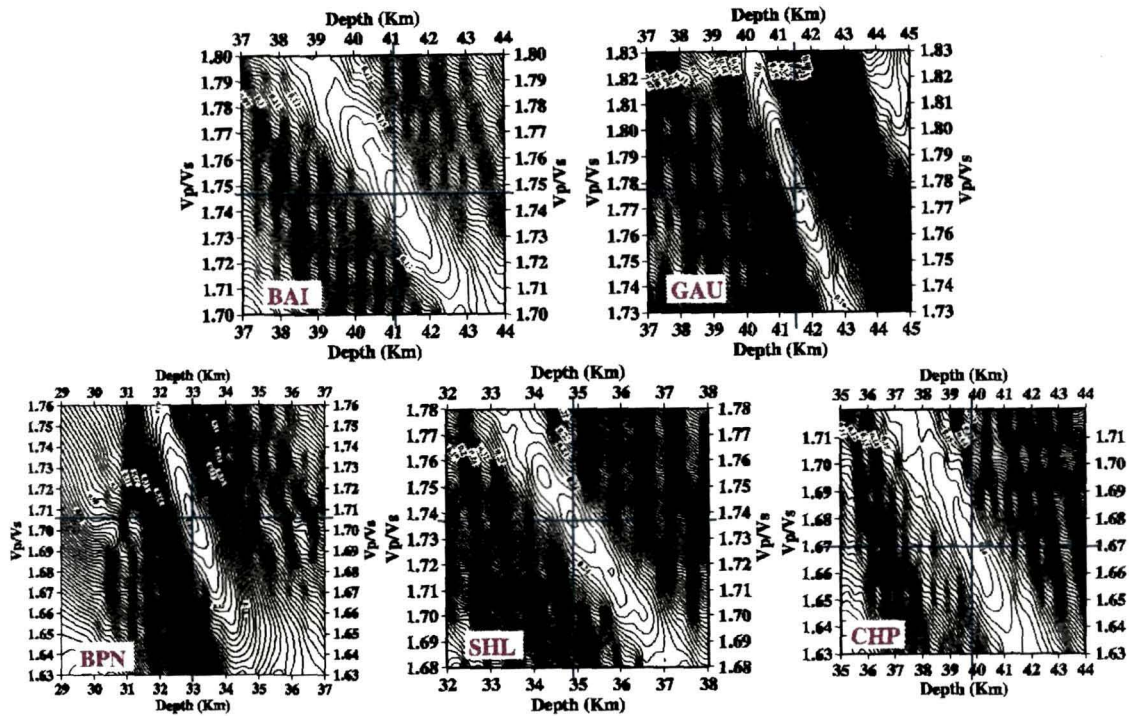
Figure 4.8: Vp/Vs ratio vs crustal thickness H for sites on the Shillong Plateau (BPN, SHL), the Brahmaputra Valley (BAI, GAU) and the Bangladesh Plains (CHP). Values of Vp/Vs-H are marked on the contour plots by blue lines.

To enhance the signal-to-noise ratio of radial receiver functions for each station, the higher quality radial receiver functions of similar back azimuth and epicentral distances were stacked and these were then inverted jointly with the surface wave group velocity dispersion data as in the case of TEZ. The inversion results for each of the stations are presented in Figures 4.9 to 4.22, with a summary in Figure 4.23 and Figure 4.24.
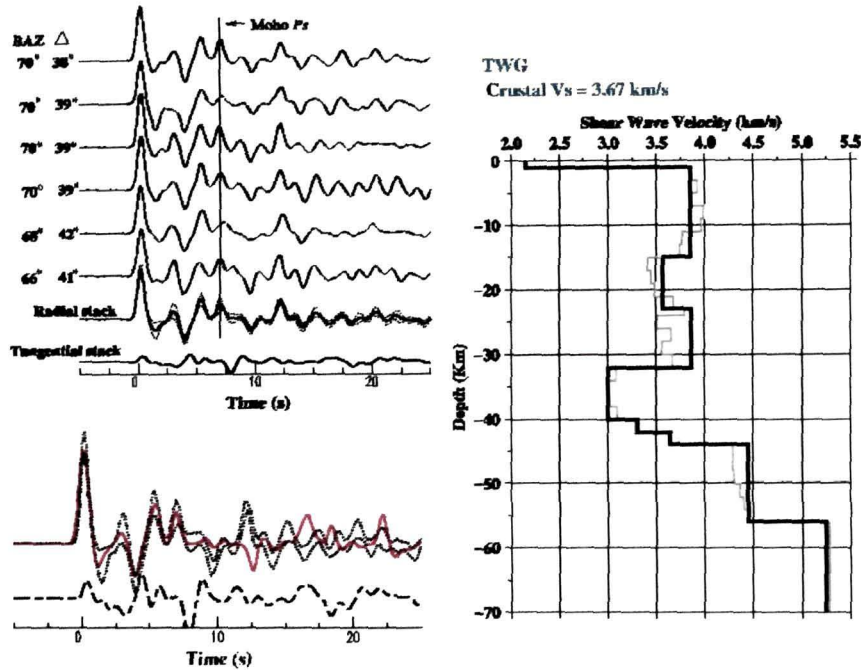
Figure 4.9: Inversion results for TWG. Individual and stacked radial receiver functions with ±1 standard deviation (SD) bounds, stacked tangential receiver function and synthetic receiver function calculated from the thick-layer (bold line) model (right), plotted within ±1 SD bounds of data.
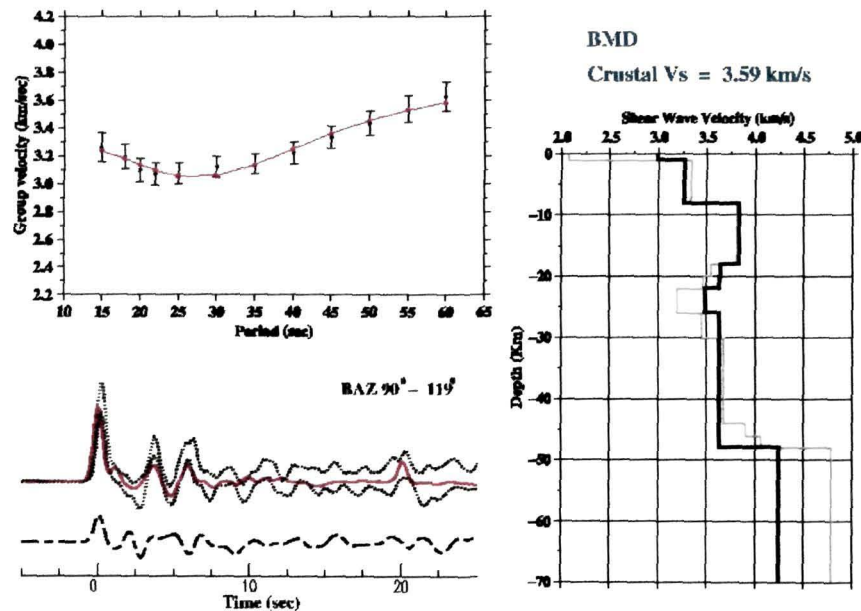
Figure 4.10: Joint inversion results for BMD. (left) synthetic dispersion and receiver functions (red) are plotted within the error bounds of dispersion and ±1 SD bounds of Receiver Functions respectively calculated from the thick-layer (bold line) model shown on the right.
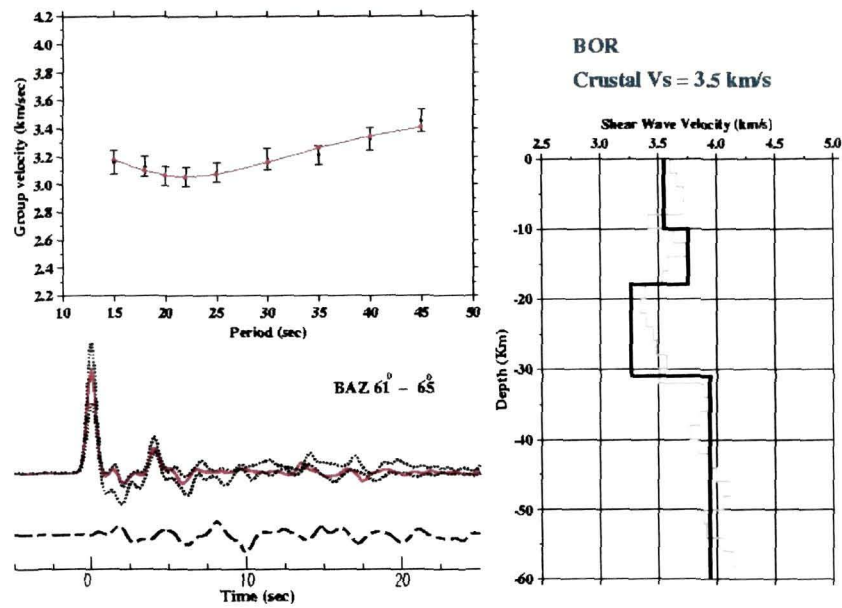
Figure 4.11: Joint inversion results for BOR. The figure format is the same as for Figure 4.10.
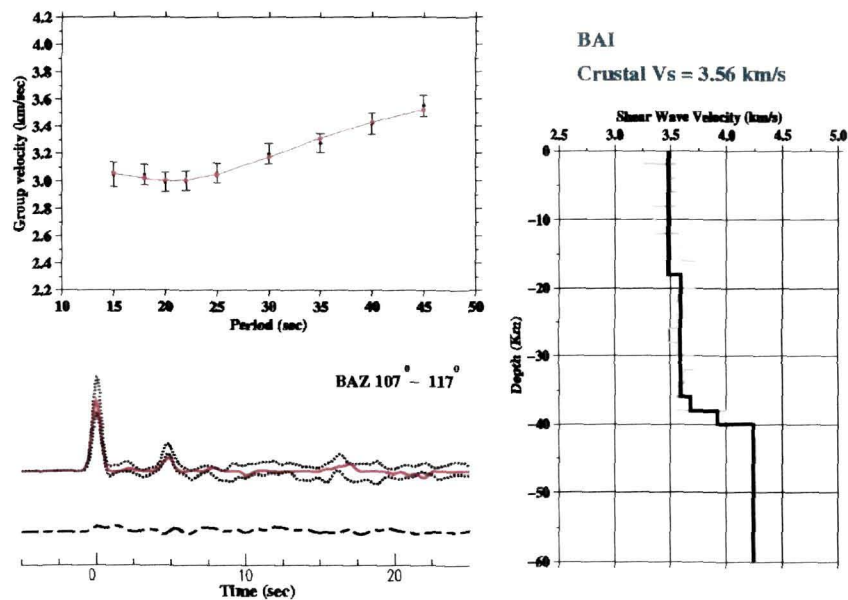
Figure 4.12: Joint inversion results for BAI. The figure format is the same as for Figure 4.10.
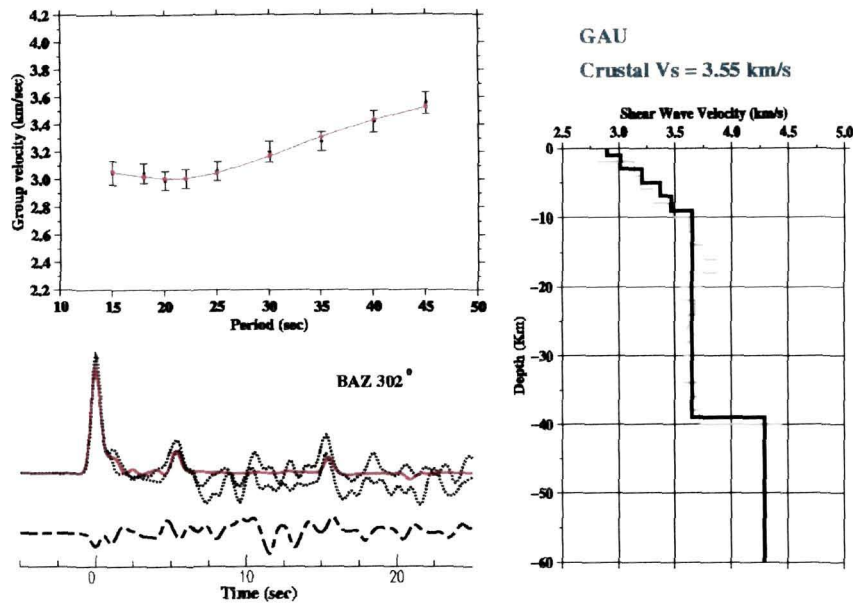
Figure 4.13: Joint inversion results for GAU. The figure format is the same as for Figure 4.10.
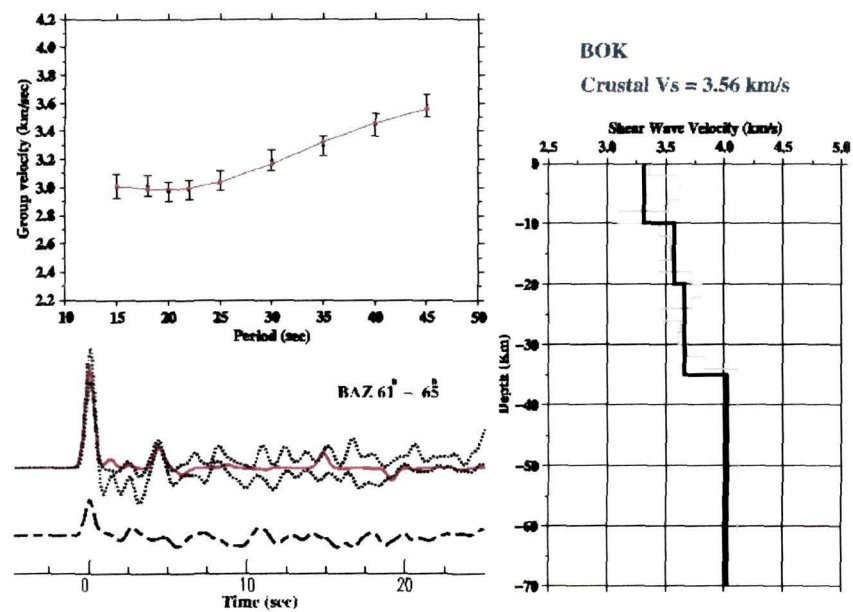
Figure 4.14: Joint inversion results for BOK. The figure format is the same as for Figure 4.10.
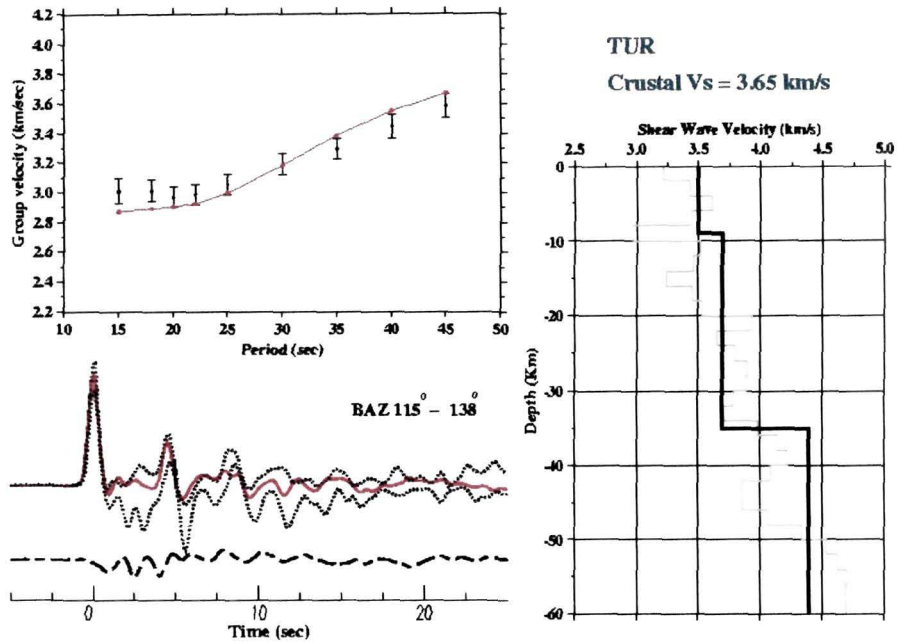
Figure 4.15: Joint inversion results for TUR. The figure format is the same as for Figure 4.10.
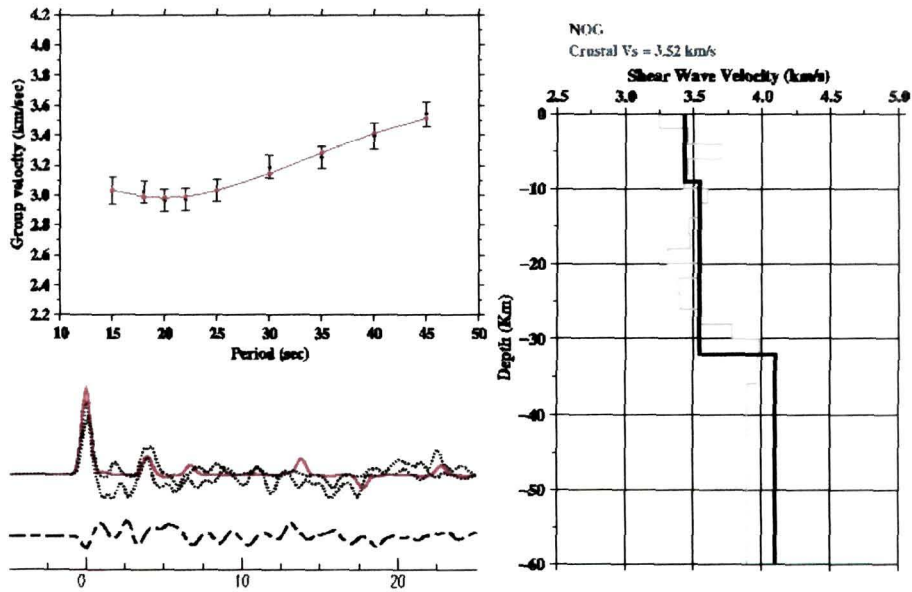
Figure 4.16: Joint inversion results for NOG. The figure format is the same as for Figure 4.10.
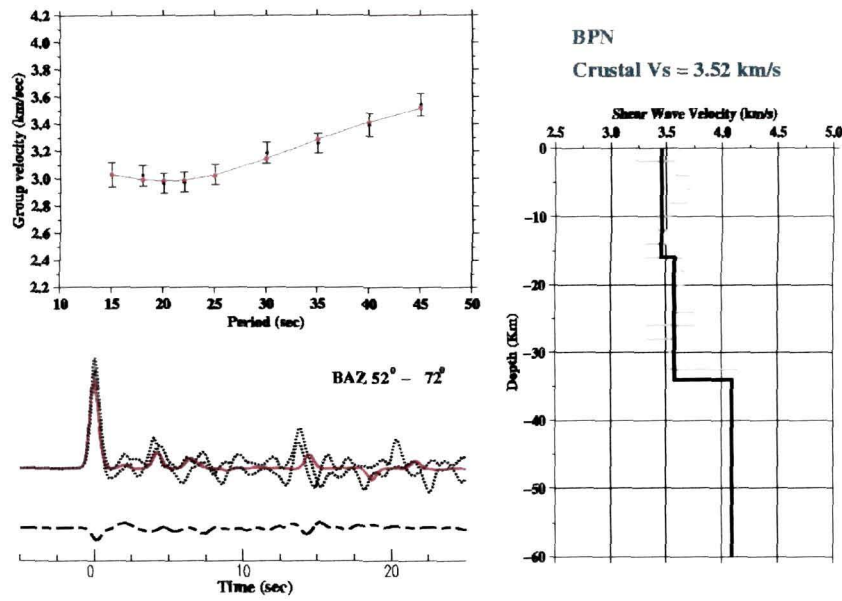
Figure 4.17: Joint inversion results for BPN. The figure format is the same as for Figure 4.10.
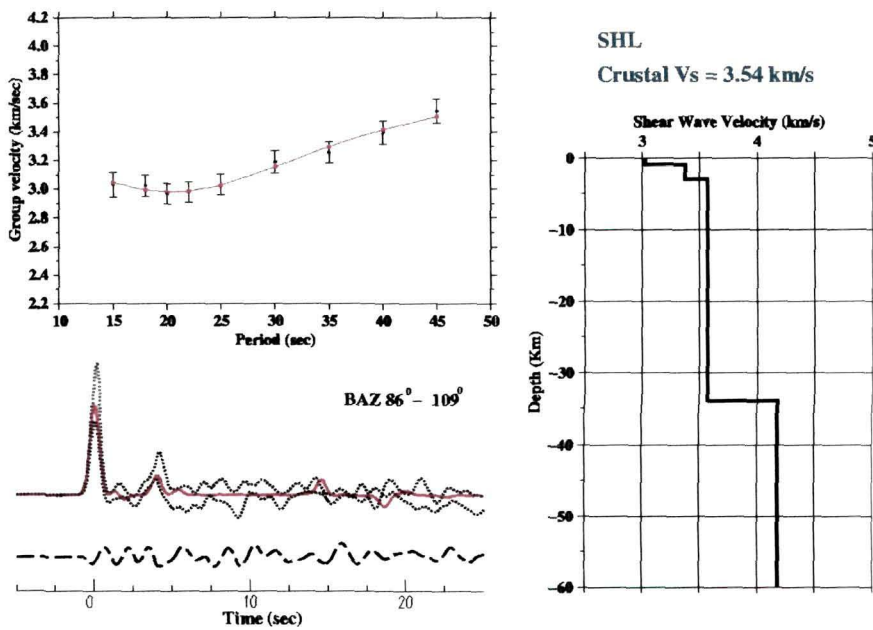
Figure 4.18: Joint inversion results for SHL. The figure format is the same as for Figure 4.10.
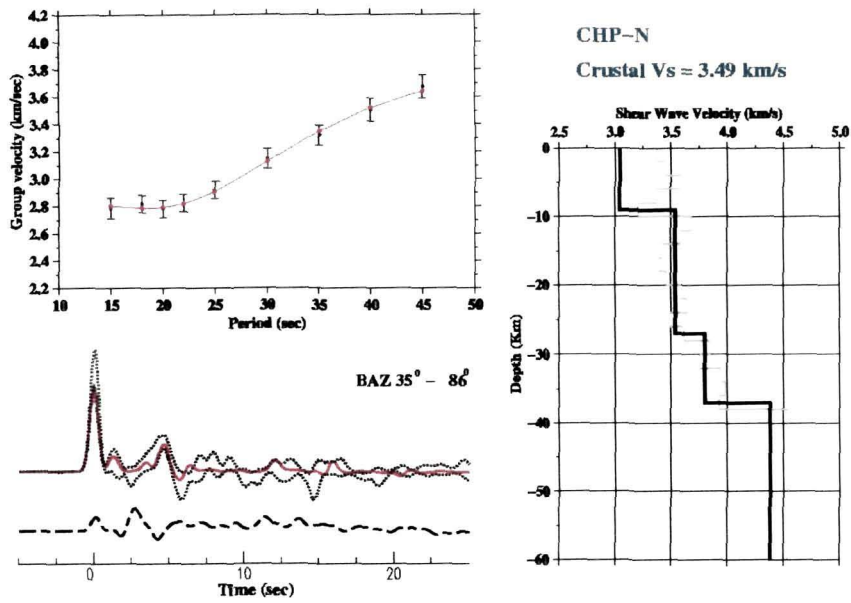
Figure 4.19: Joint inversion results for CHP-N. The figure format is the same as for Figure 4.10.
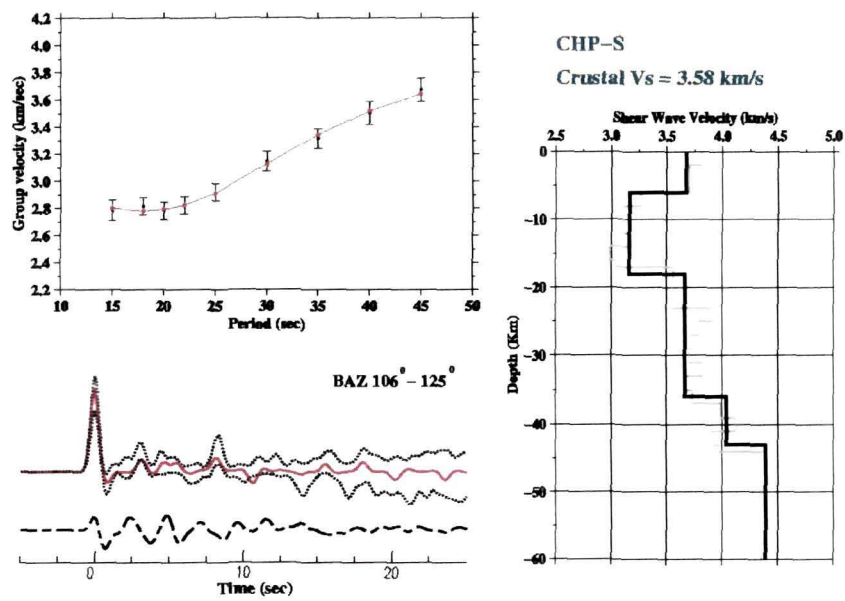
Figure 4.20: Joint inversion results for CHP-S. The figure format is the same as for Figure 4.10.
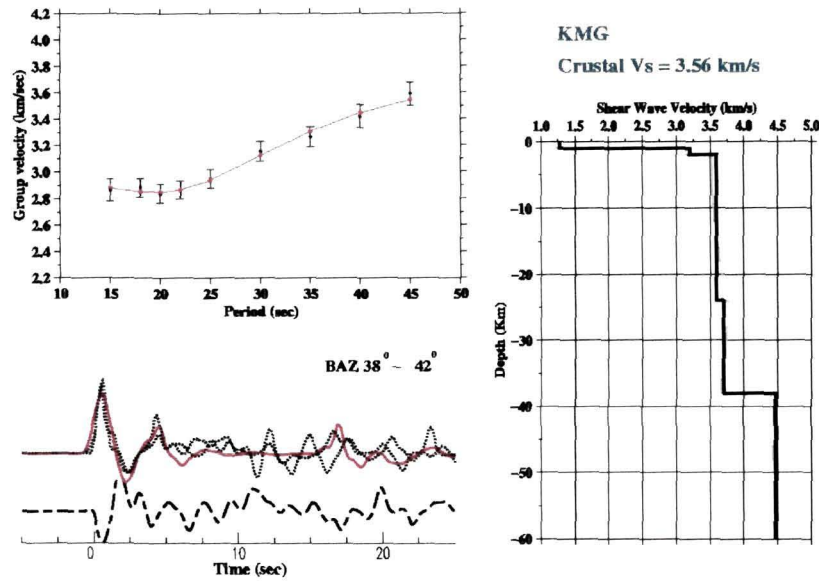
Figure 4.21: Joint inversion results for KMG. The figure format is the same as for Figure 4.10.
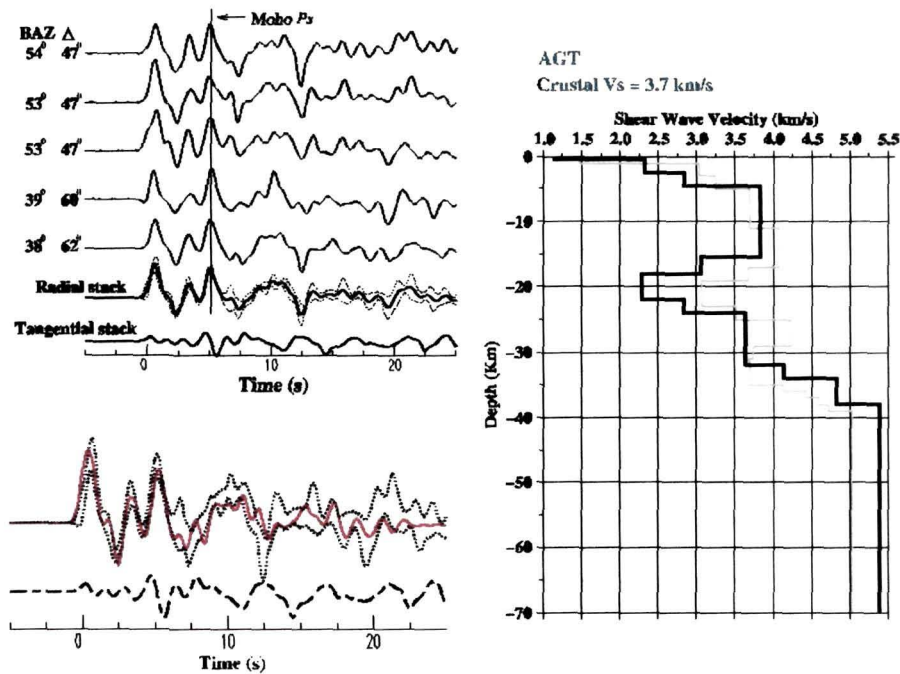
Figure 4.22: Inversion results for AGT. Individual and stacked radial receiver functions with ±1 standard deviation (SD) bounds, stacked tangential receiver function and synthetic receiver function calculated from model (right), plotted within ±1 SD bounds of data.

Crustal structure models determined from joint inversion of receiver functions and surface wave dispersion data (Figure 4.23 and Figure 4.24), along the S-N profile, from Agartala in the south to Tawang in the north, point to the existence of a two-layered crust. These results show a crustal thickness of 38-40 km beneath the southernmost site located at Agartala close to the Bay of Bengal, with a 5 km thick very high velocity layer (S-wave velocity 4.9 km/s) immediately above the Moho, most likely indicating the existence of the oceanic crust south of the Bengal Basin hinge zone. The Moho beneath the Shillong Plateau is 34-36 km deep with a crustal structure typical of the Indian shield. To the north of the plateau, the crust thickens to 40-42 km beneath the Brahmaputra Valley with an average crustal shear wave speed of 3.56 km/s, and to 48-50 km beneath the Lesser Himalaya with crustal shear wave speed of 3.59 km/s, and 55-57 km beneath Tawang in the Great Himalaya with average crustal shear velocity 3.7 km/s. To the north of the Great Himalaya beneath the southern Tibetan Plateau, the Indian Moho continues to dip northward at 6° reaching a depth of ~90 km beneath Lhasa.
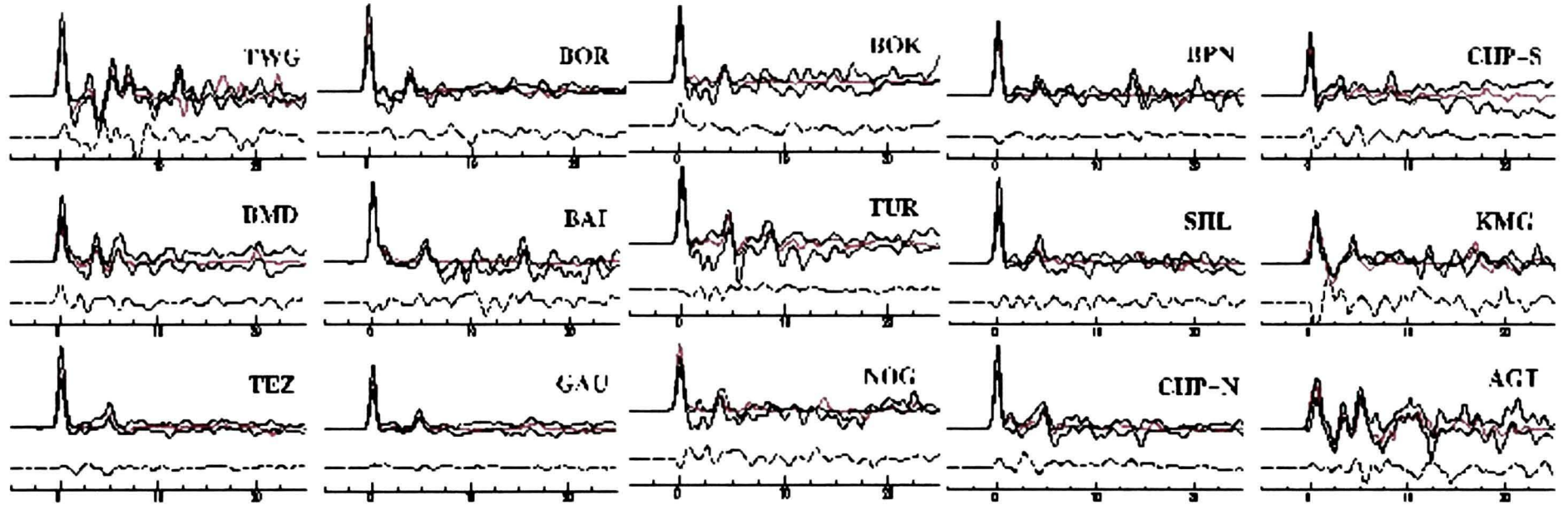
Figure 4.23: The dotted lines in the receiver function plots are the ±1 SD bounds of the stacked receiver functions of real data and the solid red lines are the synthetic receiver functions corresponding to the velocity models obtained from the joint inversions of receiver function and surface wave dispersion measurements which are shown in Figure 4.24.
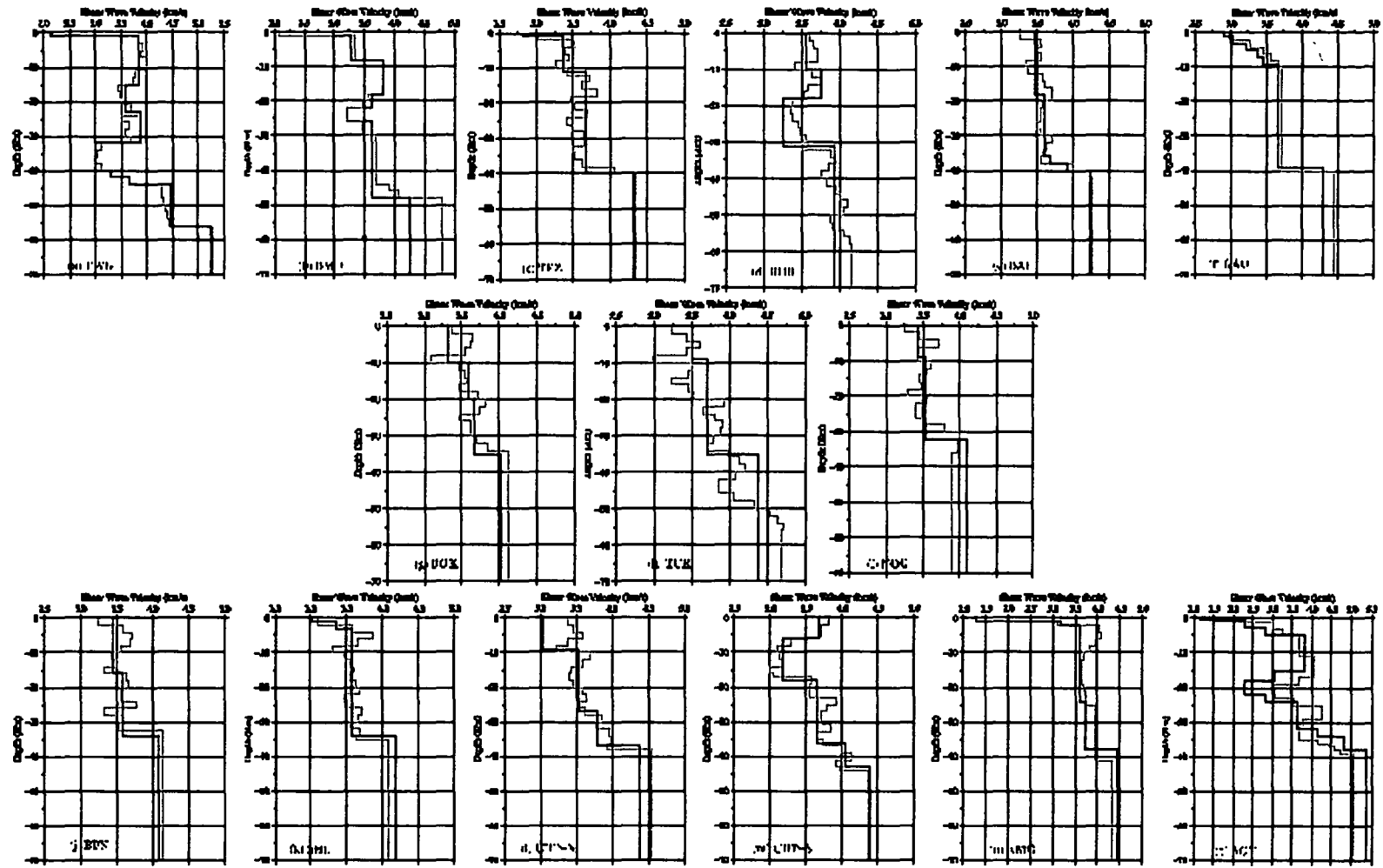
Figure 4.24: Seismic structure beneath the stations located along the SN profile (Figure 4.1). Many of the stations show clear mid-crustal velocity jump and thicker crust.

4.5 A Critical Analysis of The Shear Wave Speed Structure of Northeast India Obtained from Inversion of Receiver Functions alone (Mitra et al. 2005) and from Joint Inversion (section 4.4 above), and Discussion of Uncertainties

Figure 4.24 summarizes the one-dimensional crustal models beneath various stations in northeast India. The two stations (AGT and TWG) located at the southernmost and northernmost margins of the SN profile (Figure 4.1) have Moho depths at ~38-40 km and 55-57 km respectively. At AGT a pile of ~6 km sediments overlie a high velocity crystalline crust and' the sediments - basement interface generates large amplitude reverberations which dominate the early part of the receiver functions whereas at TWG only a thin veneer of sediment overlies a rather low velocity crystalline crust. The surface wave group velocity data at the greater Himalayan station TWG was found to be incompatible with information in the receiver functions. This is understandable because the site is expected to be amidst significant heterogeneity and the 1° resolution limit of the group velocity information, does not allow clear resolution of the different crustal types sampled in the region.

At KMG in the northernmost Bengal Basin the crustal thickness of 38±2 km obtained from joint inversion is somewhat smaller than that obtained by Mitra et al (2005) using receiver functions alone which were rather limited in azimuth and largely sampled the Moho near the southeastern edge of the Shillong Plateau. The marginally lower value obtained from the joint inversion most likely offsets this bias because of being additionally constrained by the surface wave dispersion data.

Similarly, crustal velocity models beneath the stations (CHP-N, SHL, BPN, NOG) derived from joint inversion yielded a significantly shallower Moho

beneath the Shillong plateau (34-36km as against 35-38 km of Mitra et al.) in comparison to its southern and northern limits beneath Bengal Basin (38-40 km) and Brahmaputra Valley (40-42km) respectively.

Joint inversion of the existing and new receiver function dataset with Rayleigh wave dispersion measurements have constrained the vertical averages of shear wave speed structure for the crust and the upper most mantle. This in turn enables a better estimation of the depth to different discontinuities beneath each station. The shear wave velocity models obtained by Mitra et al (2005) had slightly overestimated the velocities and hence produced deeper depth to different discontinuities. The thickness of the crust determined from joint inversion is significantly shallower than the depths quoted by Mitra et al. (2005) for some of these stations (Table 4.2). The current study is a clear improvement in the velocities of the different crustal layers and depth to boundaries but the overall structure across the Shillong plateau and the geometry of the Moho is similar to the findings of Mitra et al. Thus the shallower Moho depth beneath the Shillong Plateau supports the hypothesis that the plateau crust has been upthrust in response to the regional compressive stresses of convergence along mantle reaching faults and that the lower crust beneath it is therefore strong contrary to the inference of Molnar and Pande (1989).

A schematic map of the NS profile (Figure 4.1) from the southern Tibetan Plateau to the Bengal Basin along with the crustal structure of the NE India stations is shown in Figure 4.25.

Table 4.2: Station name, location, average crustal Vs and crustal thickness obtained from the inversion of receiver function alone (Mitra et al., 2005) and from the joint inversion of receiver function with surface wave dispersion data for the stations used in this study.

Station	Lat (°N)	Long (°E)	Mitra et al. (2005) results		Joint Inversion results	
			Crustal Vs (km/s)	Moho depth (km)	Crustal Vs (km/s)	Moho Depth (km)
AGT	23.7874	91.2711	-	-	3.70±0.25	38±2
KMG	24.8466	92.3435	3.53	39	3.56±0.26	38±2
CHP-S	25.2806	91.7235	3.63	44	3.58±0.26	43±2
CHP-N	25.2806	91.7235	3.76	38	3.49±0.25	37±2
SHL	25.5663	91.8558	3.77	35	3.54±0.25	34±2
BPN	25.6698	91.9088	3.76	35	3.52±0.25	34±2
NOG	25.8999	91.8669	-	-	3.52±0.3	33±2
BOK	25.9799	91.2422	-	-	3.56±0.3	35±2
TUR	25.5300	90.2114	-	-	3.65±0.3	35±2
GAU	26.1500	91.6500	3.63	40	3.55±0.25	39±2
BAI	26.3183	91.7399	3.86	42	3.56±0.2	40±2
TEZ	26.6333	92.8333	3.83	42	3.57±0.2	40±2
BOR	26.4112	92.9321	-	-	3.50±0.3	32±2
BMD	27.2713	92.4181	3.58	48	3.59±0.25	48±2
TWG	27.6298	91.8583	-	-	3.67±0.27	57±2
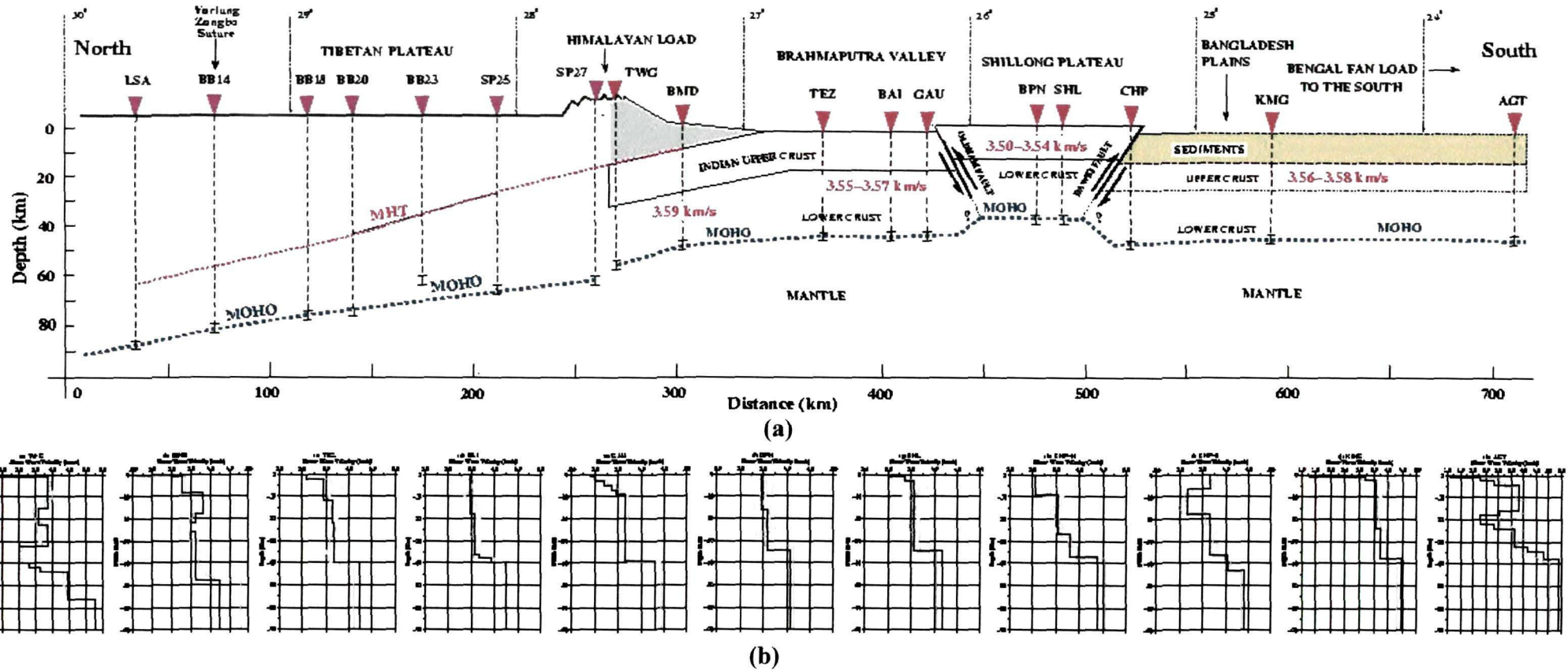
Figure 4.25: (a) A schematic illustration of the NS profile from the southern Tibetan Plateau to the Bengal Basin. The seismograph stations are marked with inverted triangles. Depths to the Moho are shown by vertical dashed lines with error bars beneath each seismic station. MOHO and MHT represent the Moho discontinuity and the Main Himalayan Thrust (MHT) in the figure. The relationship of the faults bounding the Shillong Plateau is taken from Bilham and England 2001. (b) Inversion results for all the stations from Bengal Basin (AGT) to the Higher Himalayas (TWG).

4.6 Crustal Anisotropy

A seismic shear wave entering upon an anisotropic region splits into two orthogonal phases with polarizations and velocities determined by the properties of the anisotropic media. The fast and slow propagating phases, progressively separate in time as they travel forward. The splitting, however, is preserved during their passage through any isotropic segment along the ray path, and can be detected as a time delay between the two horizontal components of motion, its polarity and amplitude being strongly affected by the azimuth of the arriving wave. The existence of such split S-waves, whenever detected, therefore signifies the presence of anisotropy and an analysis of the polarity and amplitudes of the split phases, yields knowledge of the anisotropy characteristics of the subsurface. Receiver functions calculated for all stations whose data have been used in this study were therefore subjected to such an analysis and its theoretical basis is explained in chapter 3.

A cross-correlation analysis (Browman and Ando, 1987; McNamara and Owens, 1993; Tong et al., 1994; Herquel et al., 1995) was used to determine the split-time and the azimuth of the symmetry axis of anisotropy responsible for splitting the Ps phases. This was analysed by incrementally rotating the two orthogonal components of the receiver functions from -90° to 90° in steps of 2° at a time and their cross-correlation coefficients calculated for time lags of -0.5 to +0.5s in steps of 0.01s.

An example of splitting in the Moho converted Ps phase recorded at TEZ and the corresponding particle motions before and after the correction for anisotropy is shown in Figure 4.26.
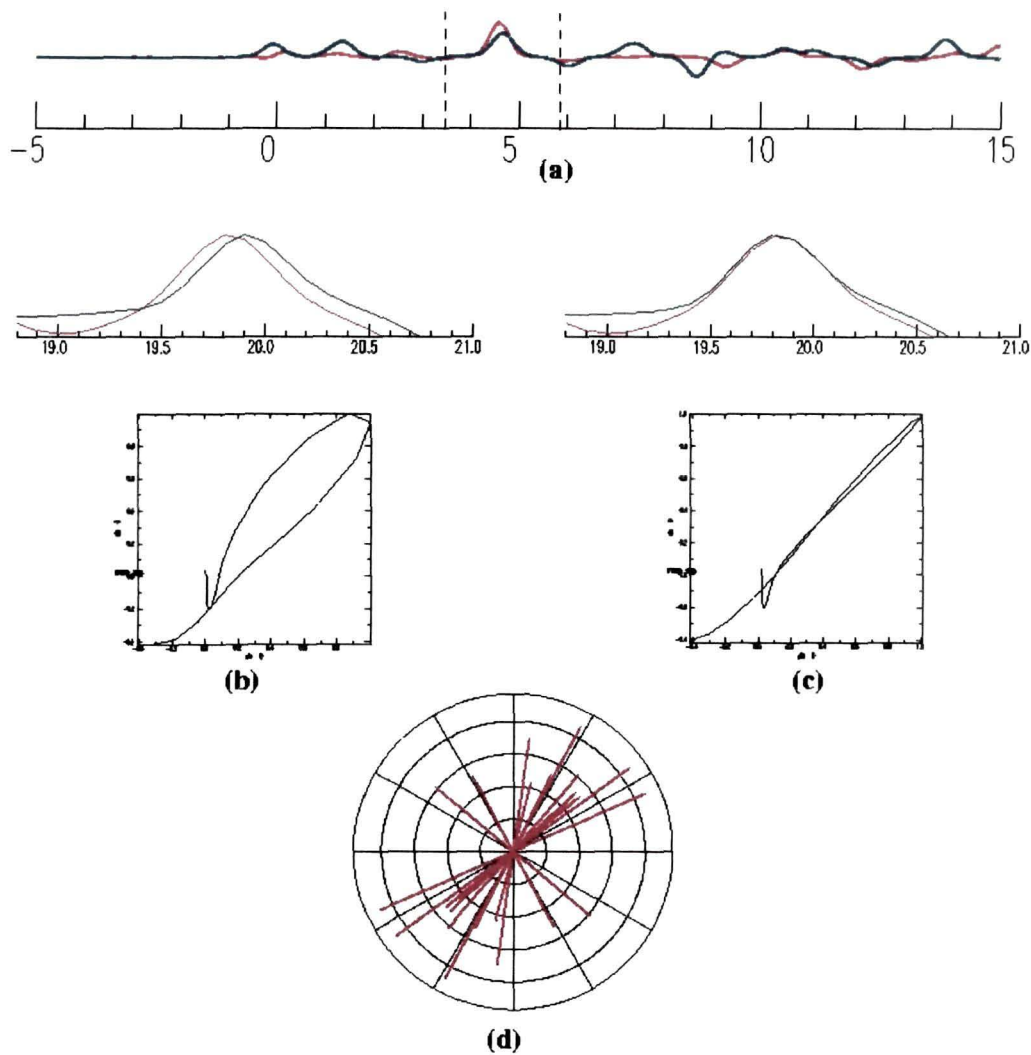
Figure 4.26: (a) Splitting of Moho converted Ps phases observed in the radial and tangential components of the receiver functions recorded at TEZ. (b) Uncorrected and (c) corrected radial and tangential receiver functions respectively with the corresponding particle motion diagram for the window length considered for the analysis. (d) observations of splitting from various directions is shown in the rose diagram.

Results of analyses of the crustal Ps phase splitting, for 10 stations in NE India are summarized in Figure 4.27. The fast velocity direction beneath the stations except on the Shillong Plateau (SHL, BPN) is found to lie along a roughly N-S

direction. On the other hand the azimuths of vertically averaged anisotropy (fast velocity direction) beneath the Shillong Plateau stations are in good correlation with the many E-W directed shear-zones and faults observed in the region.
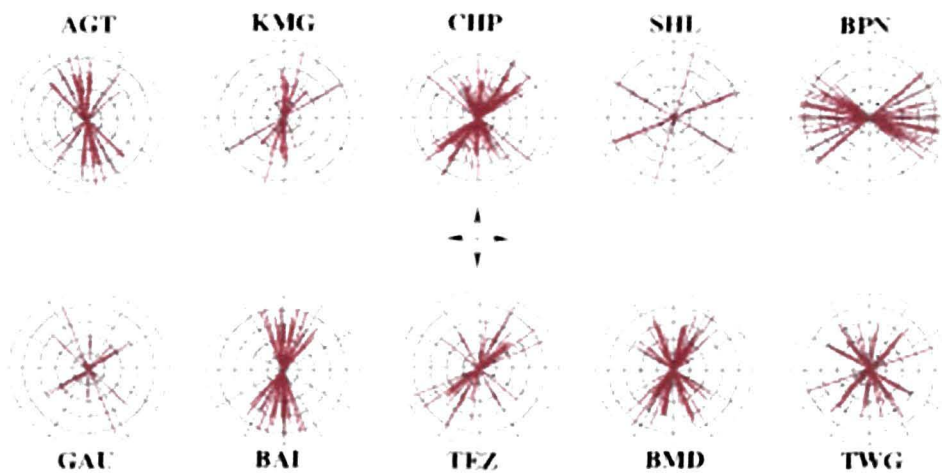
Figure 4.27: Magnitude and azimuth of vertically averaged seismic anisotropy in the crust derived by analysis of the Moho converted Ps phase recorded on radial and transverse components of the receiver functions for the stations in NE India.

Summary

This chapter has described the abstraction and inversion of receiver functions along with surface wave group velocity data to determine the seismic characteristics of northeastern India. A total of 22 stations data were analyzed, fifteen of which involved modified analysis of an earlier work (Mitra et al.

2005, Yuan et al., 1997) and reinterpretation in the light of additional data sets especially the surface wave dispersion data and seven new stations data designed to provide a greater spatial coverage of the region. Significant findings of this experiment are summarized below:

- The results broadly reproduce the findings of Mitra et al. (2005) that the Indian crust Moho progressively deepens northward beneath the Himalaya and Tibet.

- The average shear wave speeds in the crust beneath the various seismic stations in northeast India have been more tightly constrained by joint inversion of both the receiver function and the Rayleigh wave dispersion data. These bring out the remarkable unity of the Indian crust (Vs = 3.49 – 3.67 km/s) structure right from the Shillong plateau northward up to the great Himalaya, and lend credence to the interpretation that the entire crust of the Shillong plateau including the lower has been up-thrust along mantle reaching faults (Figure 4.25), and that the lower crust beneath it is strong contrary to the conclusion made by Molnar & Pandey, 1989.

- An oceanic type crust (Vs=4.2 – 4.8 km/s) most likely underlies a thick pile of Bengal basin sediments (22 km vide Hiller, 1988) with a relatively undisturbed Moho at a depth of ~38 km.

- Lastly they provide a test of the hypotheses that the entire Shillong Plateau crust has been uplifted along mantle reaching faults and that its ~1 km high uncompensated topography is maintained dynamically by the stress field provided by the ongoing Indo-Eurasian collision.

The crustal structure of the NE India is also characterized by the presence of strong seismic anisotropy in the crust. The azimuth of anisotropy is well correlated with the orientation of the geological grain in the region.

Chapter 5

Moho Topography beneath the Shillong Plateau and Mikir Hills

5.1 Perspective

Mitra et al. (2005) described an experiment exploiting the absence of the expected large negative Bouguer gravity anomaly (Verma & Mukhopadhyaya) over the ~1 km high Shillong plateau, to test the hypothesis whether the lower crust beneath the plateau was strong as would be required by the calculated ~30 km thickness of the elastic layer (Mckenzie – personal discussion), or weak as taught by the jelly sandwich model (Chen and Molnar, 1983). An earlier determination of Shillong plateau earthquakes by Chen and Molnar (1990) had placed them all in the upper mantle below the crust implying that the lower crust of the plateau was too weak to sustain long term strain storage. On the other hand, a strong lower crust was required by the mantle reaching fault model advanced by Bilham and England (2001) to fit the shear strain field determined from three epochs of geodetic data across the Shillong plateau that had been first generated by the survey of India in 1862 before the M=8.1, 1897 Shillong plateau earthquake and resurveyed in 1898 and 1936. Mitra et al. (2005) reduced the problem of testing the above mentioned hypothesis to an experimental test to determine whether the crustal thickness beneath the Shillong plateau compared with those of the terranes to its north and south was less or greater. For, they argued that the plateau with manifestly no crustal root in the mantle would

respond to an ambient compressive regime by thickening of its lower crust if it was weak, or by up-thrusting of the entire crust along faults that cut through the lower crust in case it was at least as strong as the underlying mantle. The first scenario would after erosion (Figure 5.1), leave the crust beneath the elevated Shillong plateau a little thicker than those beneath the adjoining terranes whilst the second would thin it in comparison. They argued further that the Receiver Function approach to be adopted for determining the crustal thickness of the various terranes of the region would also yield a more reliable shear wave structure underneath them which could be used to re-determine the earthquake focal depths of the events that had been earlier investigated by Chen and Molnar (1990) to check as to where exactly they lay, in the lower crust or in the upper mantle.
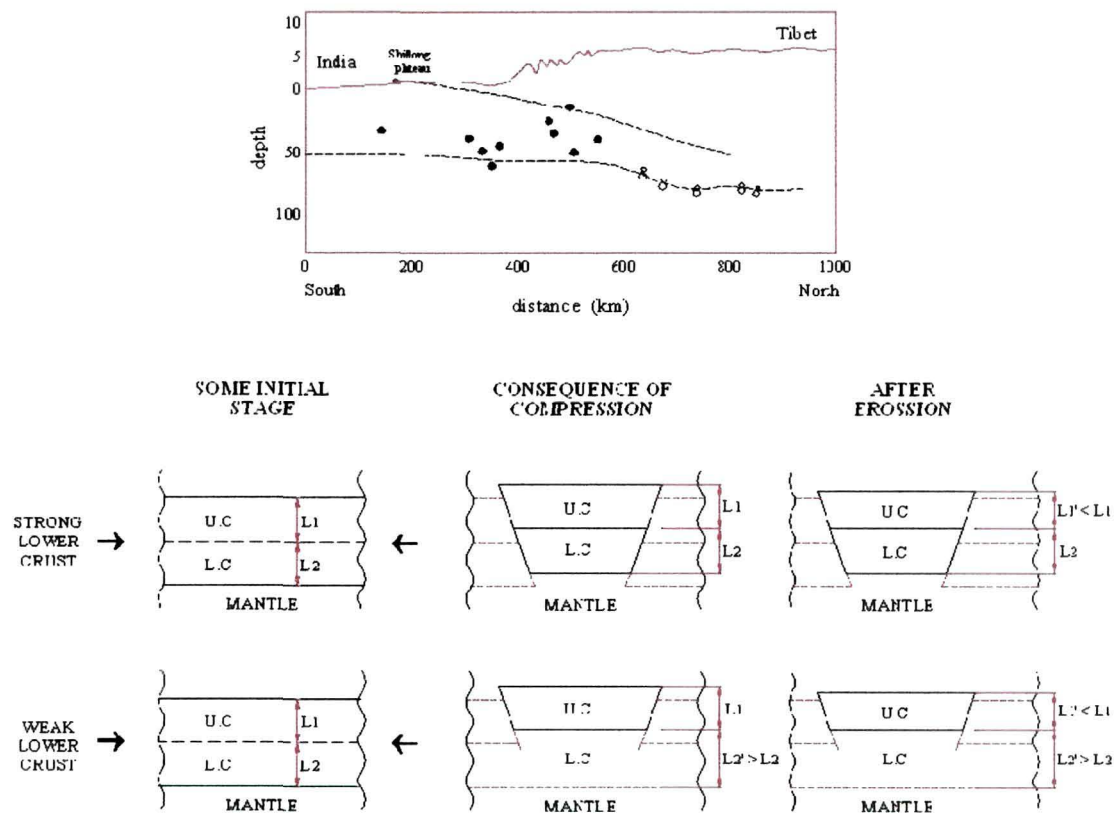
Figure 5.1: Shows schematic cross sections of two possible states of the Shillong plateau both under compression and without crustal roots in the mantle to account for near zero Bouguer anomaly over the plateau.

Mitra et al. (2005) inverted receiver functions calculated at 7 stations (Figure 5.2) along a ~500 km long S-N profile from Karimganj, south of the Shillong plateau, northward through the Brhmaputra valley to Bomdilla in the Lesser Himalaya to show that the Shillong plateau crust was thinner by at least ~4 km compared with that beneath the Brhmaputra valley immediately to its north. They explained this result by requiring the entire plateau crust to have been uplifted by reverse faults cutting right through the lower crust. They also showed that re-determination of the earthquake focal depths beneath the Shillong plateau using their receiver function inverted shear wave speed structure placed these events at the base of the lower crust reversing their implications to its hitherto assumed strength. Their work, however, left two important questions un-answered: i) whether the thinner Shillong crust found beneath the 3 stations along their S-N profile was representative of the whole plateau, and ii) whether a similar situation existed beneath the less elevated Mikir Hills of yet undetermined state of compensation, which by virtue of identical surface exposures of Proterozoic formations, has long been regarded as the north-northeastern extension of the plateau. And, if such were to be the case how the apparently easily explained model of the Shillong plateau uplift against the Oldham fault, would need to be reconsidered to explain a thinner crust beneath the Mikir Hills. Resolution of these two questions by attempting to construct a 3-dimensional image of the Moho beneath the plateau and the Mikir Hills, provided the rationale for the work whose results are presented in this chapter.
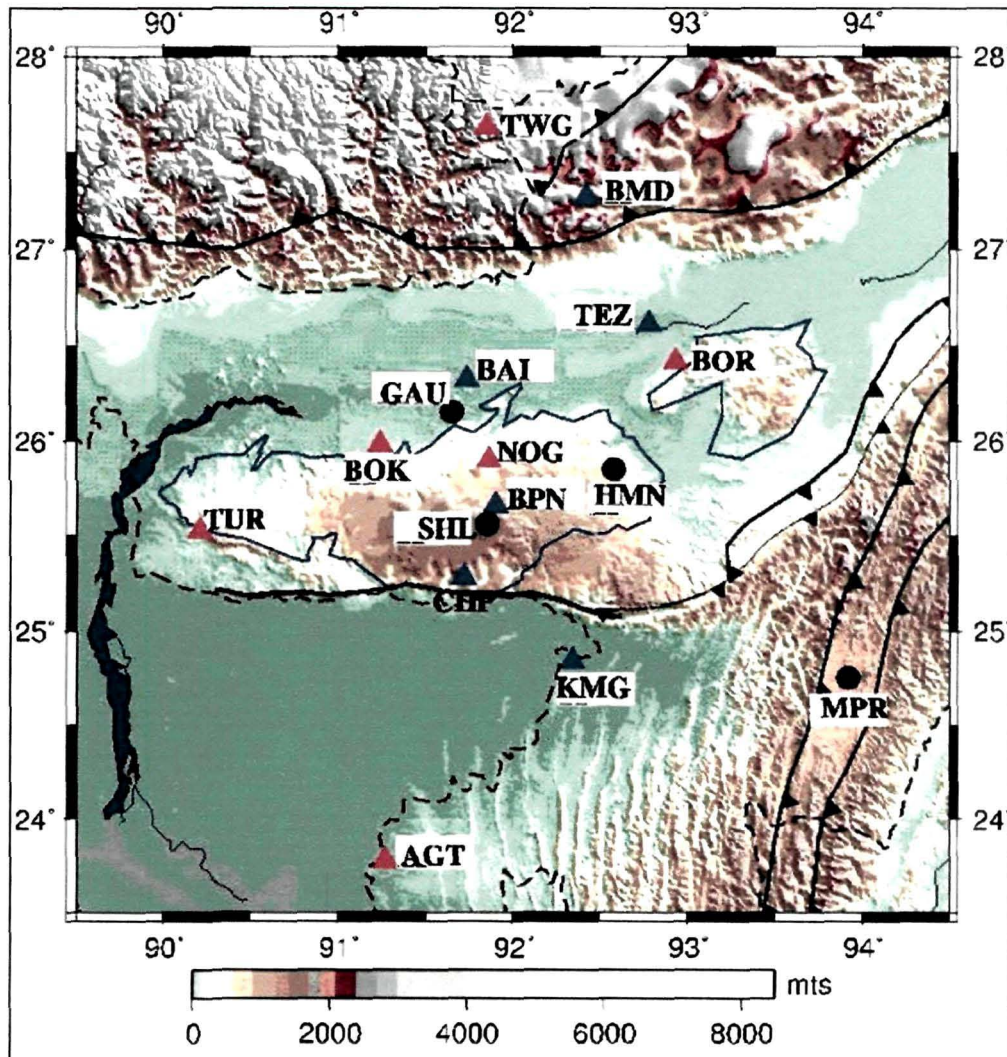
Figure 5.2: Map showing the Shillong Plateau and the Mikir Hills in the tectonic framework of northeastern India. Triangles mark the locations of broadband seismic stations where data were generated for analysis contained in this work; blue denote the stations set up by Mitra et al. (2005) and red by the present author. The 4 stations operated by other organizations, whose data were used in the present analyis are marked by dark circles.

5.2 Data

Three component broadband seismic data from 14 sites located on the Bengal basin, the Shillong Plateau, the Mikir Hills, the low lying foreland spurs of

basement outcrops in the Brahmaputra valley and the Arakan Yomas (MPR), were used to construct a 3D image of the crust beneath the plateau and the Mikir Hills. The latter on account of their similarities in relief and surface exposures are generally regarded as the north-northeastern extension of the plateau. 10 of these stations were jointly operated by the Tezpur University under a collaborative project with the Indian Institute of Astrophysics at Bangalore, the Indian Institute of Technology at Kharagpur and the University of Cambridge (UK). Data from the remaining 4 stations were obtained from DST sponsored stations operated by NGRI, IMD, the Gauhati University and the Manipur University. Seismographs at Agartala (AGT) and Karimganj (KMG) were located on the sediments of the Bengal Basin south of the Shillong Plateau; those at Cherapunji (CHP), Shillong (SHL), Barapani (BPN), Tura (TUR), Nongpoh (NOG), Hamren (HMN) on the exposed Precambrian crystalline basement of the Shillong Plateau, at Borjuri (BOR) in the Mikir Hills, at Baihata (BAI), Guwahati (GAU), Boko (BOK) and Tezpur (TEZ) on the low-lying basement ridges (foreland spur) in the Brahmaputra Valley, and at Manipur (MPR) on the Eocene Disang formations of the Arakan Yomas (Figure 5.2).

5.3 Methodology and Results

5.3.1 Polarisation Analysis of the Teleseismic Data Recorded at the various Stations on and around the Shillong Plateau and Mikir Hills for Quality appraisal

Deviations in the direction of approach of seismic waves from their expected azimuth, if detected, point to contamination of seismic signals from off-azimuth arrivals or misalignment of the seismic receiver or both, thereby providing a measure of the data quality. A polarization analysis of all

available data selected for analysis was accordingly made to screen out those data sets which did not fulfill these quality criteria.

All available teleseismic earthquake data from the 14 stations in northeastern India (Figure 5.2), selected for analysis, were first subjected to a polarization analysis to weed out those that could not be trusted for freedom from mis-orientation errors or those arising from contamination by scattered signals (Samson, 1983a). The results for various stations on and around the Plateau and the Mikir Hills are shown in figure 5.3, illustrating the co-linearity of the P-waveform polarization axes and the back-azimuths as a function of azimuth and epicentral distance. The data were filtered using a band pass filter set at 0.5 to 2.0 Hz before being subjected to the Principal Component analysis, to highlight their sensitivity to smaller scale structural features as the filter wavelengths ranged from ~12 to 3 kilometers. For example, the data from BPN station with high signal to noise ratio shows how well the direct P waveform arrivals conform to the back azimuth. These close coincidences confirm that the horizontal components of the instrument were correctly aligned with respect to the geographic north and that no significant scatterers existed in the vicinity of the seismic station to adversely degrade the records. Results of principal component analysis for the other stations across the Shillong Plateau and Mikir Hills also showed no significant deviation in the azimuths of arriving waves, again testifying to satisfactory alignment and siting of these stations. These results instill confidence in the validity of our assumption that the data at all the stations represent uncontaminated and substantially plane wave arrivals coming from the true azimuth, within the frequency band of interest.
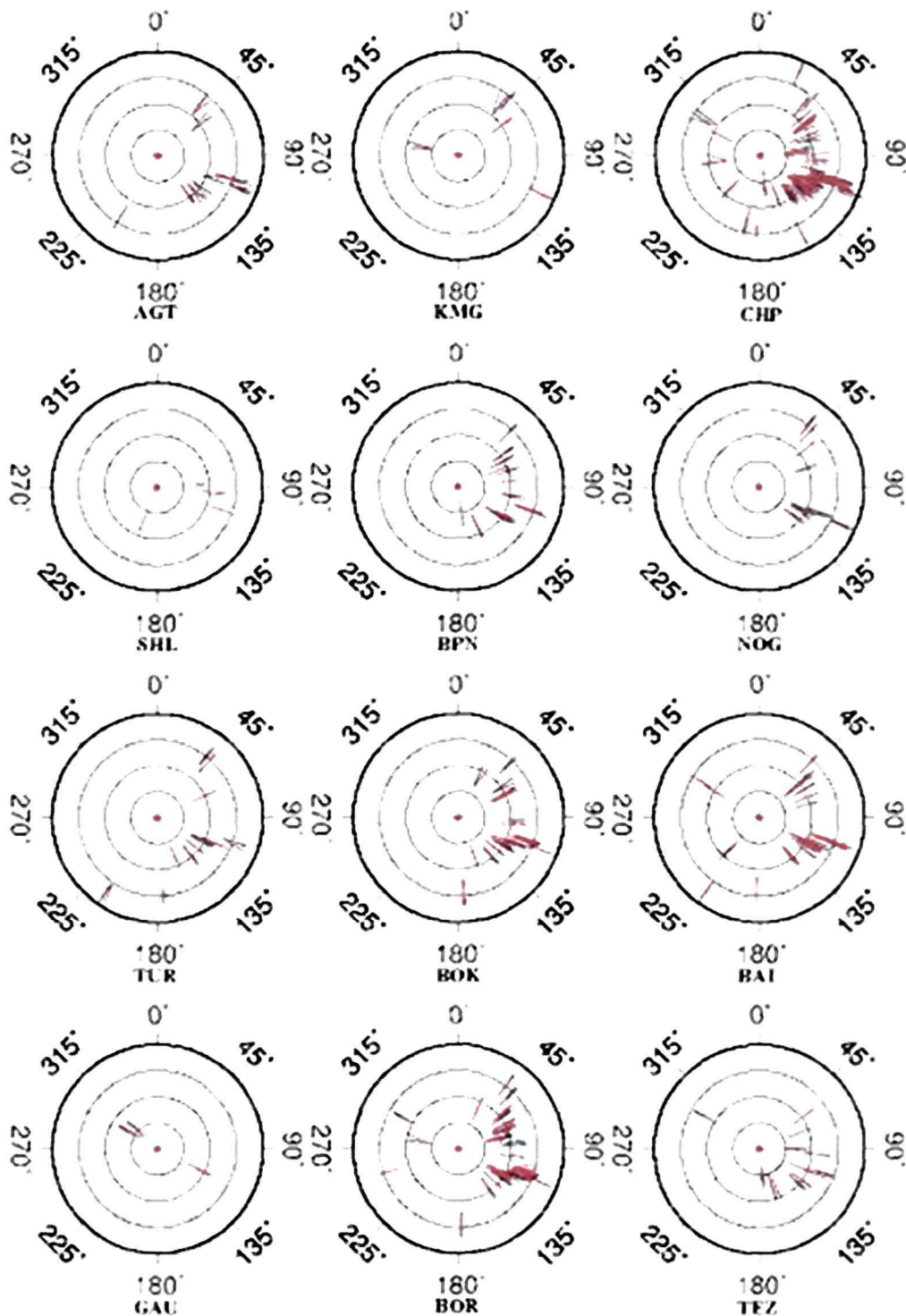
Figure 5.3: Shows the result of polarization analysis made at each station; the blue and red lines denote the back azimuth directions of individual events derived respectively from the known event-station location and from the event record by covariance analysis of the first few cycles of the P-waveform. Great circle arc lengths between source and receiver are indicated by the position of the arrows on the polar plots (0° at the center with 45° increments).

5.3.2 Seismic characteristics of the crust beneath the Shillong Plateau and the Mikir Hills and their adjoining terranes

Receiver functions were calculated for each event-station pair that passed the quality test. Those corresponding to epicentral distances and azimuths lying within narrow bins were then stacked to obtain a higher signal-to-noise representative receiver functions for each station. These were then analyzed to abstract the crustal thickness and Poisson's ratio as well as the inverted shear wave speed structure using the methods described in the previous chapter. We present below the results of our analysis of the seismological characteristics of the crust beneath all the 14 stations marked in Figure 5.2 including those already presented in chapter IV, to facilitate comparison and synthesis of results.

Figure 5.4 shows typical radial receiver functions alongwith their respective summation traces for all stations located on the Shillong Plateau and Mikir Hills, and the Bengal Basin, the Brahmaputra valley and the Arakan Yomas to its south, north and east respectively. This plot enables comparison of various features of the crust underneath the seismic stations in the region. Receiver functions for the Shillong Plateau and Mikir Hills stations (CHP, SHL, BPN, TUR, NOG, HMN, BOR) show clear Moho converted Ps arrival at about 4.0±0.5 s after the direct P-wave arrival while the Brahmaputra Valley (GAU, BAI, TEZ) and Bengal Basin stations (AGT, KMG) show the arrival times of the Ps at about 5.0±0.5 s after the direct P-wave arrival. At the station MPR in the Arakan Yomas, the Moho converted Ps phase arrives at about 7.5±0.5 s after the direct P arrival.
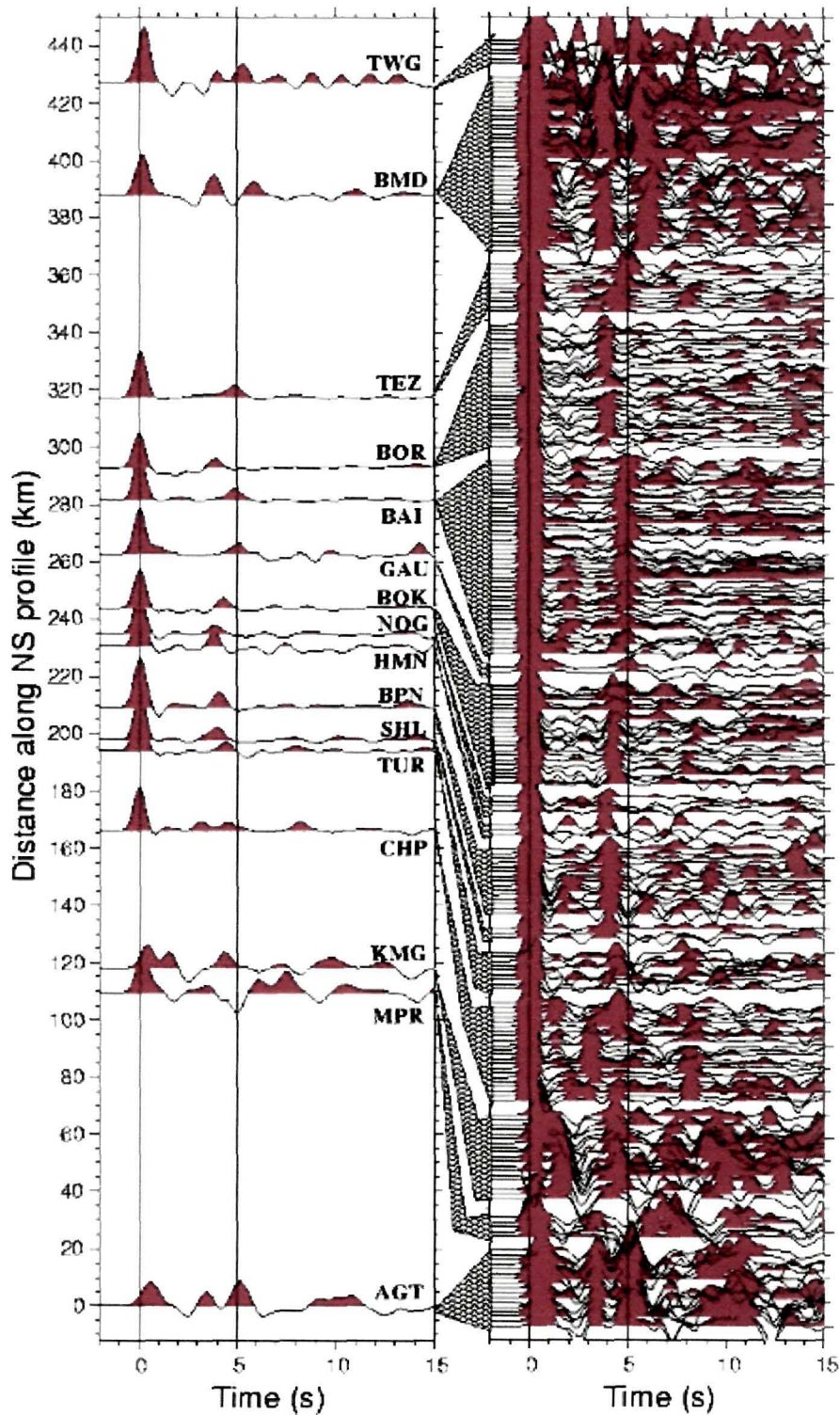
Figure 5.4: Plot of all receiver functions from the stations across the Shillong Plateau and Mikir Hills. Individual receiver functions are distance moveout corrected (67°) and plotted equally spaced from south to north sorted first by the distance along the profile and then by backazimuth. The respective summation traces are plotted on the left panel for each of the stations.

The depth to the Moho and average crustal Poisson's ratio beneath each station was obtained by converting the time series Receiver Functions into the H-Vp/Vs domain (Zandt, et al. 1995, Zhu and Kanamori, 2000), by weighting the Ps, PpPms and PpSms+PsPms phases as 0.7, 0.2 and 0.1 respectively.

Figure 5.5 shows estimates of the Vp/Vs values versus the Moho depth for six stations across the Shillong Plateau and Mikir Hills. The crustal thickness H and Vp/Vs yielded by the analysis is presented in Table 5.1. The results indicate a relatively thinner crust (~4 km) beneath the Shillong Plateau compared with that beyond its southern margin in the Bengal basin as well that beyond its northern margin beneath the Brahmaputra Valley.
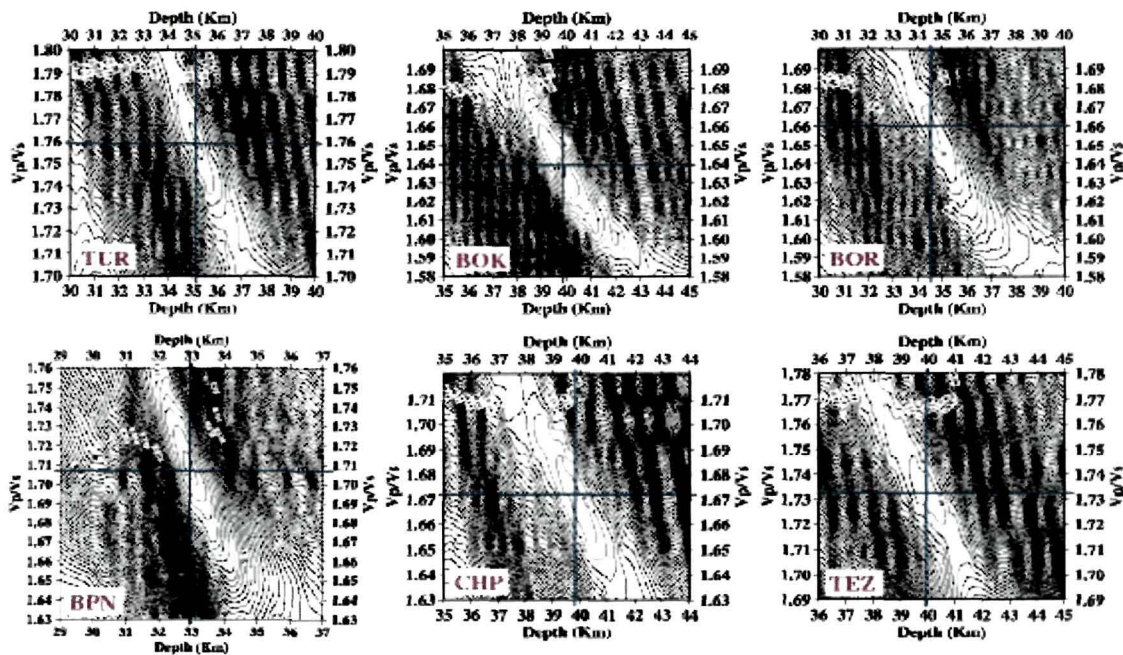
Figure 5.5: Vp/Vs values vs crustal thickness H for the Shillong Plateau (BPN, TUR), the Mikir Hills (BOR), the Brahmaputra Valley (BOK, TEZ) and the Bangladesh Plains (CHP). Best estimated values of Vp/Vs and H are marked on the contour plots by blue lines.

Table 5.1: Crustal thickness and average Vp/Vs values for six stations over the Shillong Plateau and Mikir Hills

Station	Crustal thickness H (km)	Average crustal Vp/Vs
TUR	35	1.76
BOK	40	1.64
BOR	34	1.66
BPN	34	1.71
CHP	40	1.67
TEZ	40	1.73

Crustal structure beneath the seismic stations over the Shillong Plateau and Mikir Hills were determined by jointly inverting the P-wave receiver functions and Rayleigh wave group velocity data, using a stochastic least squares approach (Hermann, 2002). The theoretical basis of the technique is described in chapter 3 and the analysis procedure is detailed in the previous chapter.

Fundamental mode Rayleigh wave group velocity dispersion data for the stations were taken from Mitra et al. (2005b) between 15 and 45s period where they are most sensitive to crustal S-wave velocities. Representative Rayleigh wave group velocity dispersion curves for the four regions in NE India are shown in Figure 5.6.
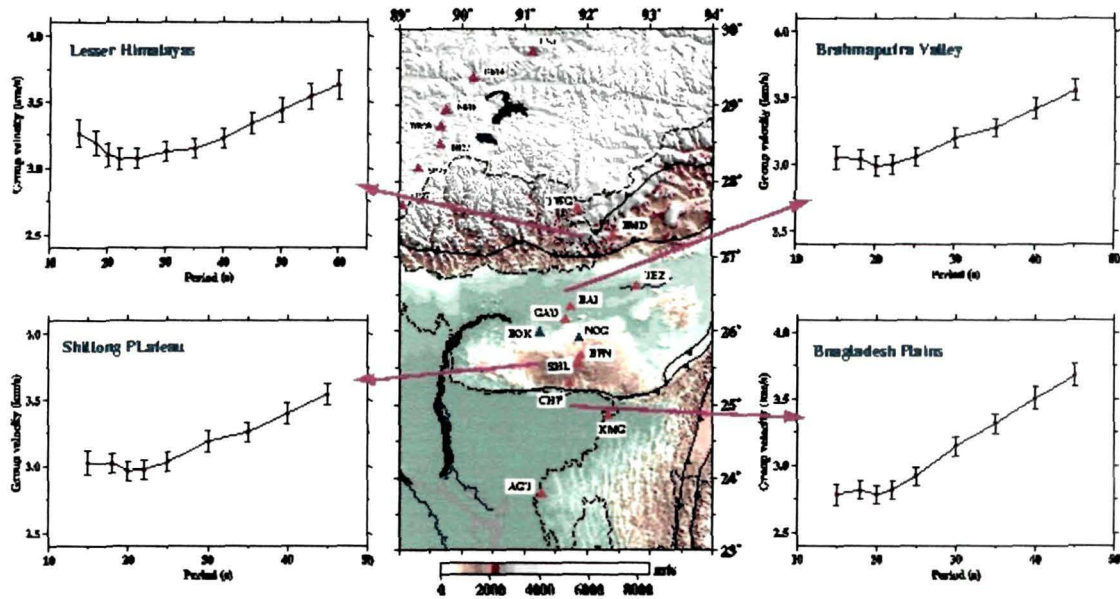
Figure 5.6: Fundamental mode Rayleigh Wave Group velocity dispersion for the four different regions across NE India.

A summary of the joint inversion results for the crustal speed structure beneath stations across the Shillong plateau and Mikir Hills, determined in the same fashion as described for TEZ in the previous chapter, is presented in Figure 5.7. These show that the crust beneath the Shillong plateau as well as the Mikir Hills is at least ~5 km thinner compared with that beneath the Brahmaputra valley to the north and Bangadesh Plains to the south.
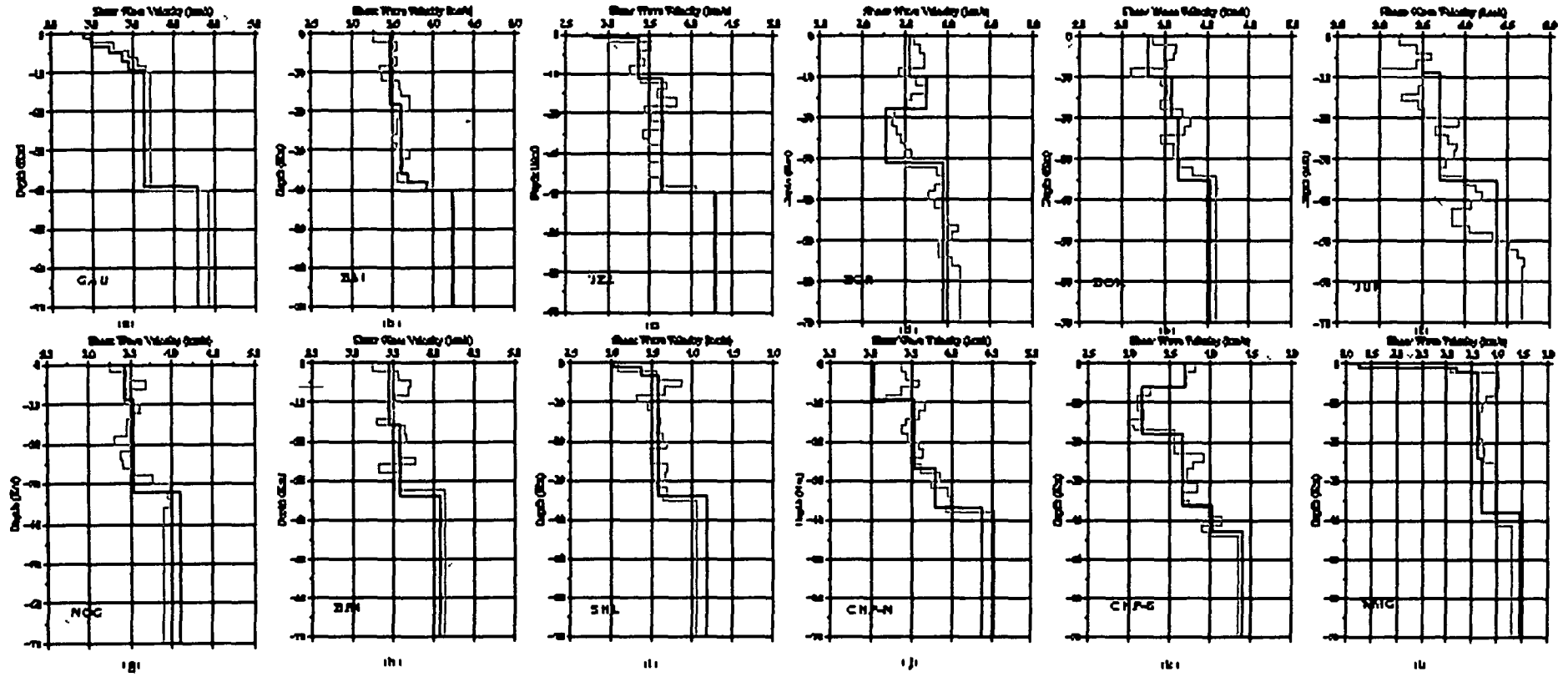
Figure 5.6: Summary of crustal structure beneath the seismic stations located on and around the Shillong Plateau and Mikir Hills. (a) GAU, (b) BAI, (c) TEZ, (d) BOR, (e) BOK, (f) TUR, (g) NOG, (h) BPN, (i) SHL, (j) CHP-N, (k) CHP-S and (l) KMG.

5.3.3 Four Profiles across the Shillong Plateau and Mikir Hills

In order to make a systematic comparison of the crustal structure underneath the Shillong plateau and the Mikir Hills with those beneath the adjoining terranes, it was thought instructive to study their dispositions across a few non parallel profiles traversing the entire region, allowed by the limited data. Four profiles (Figure 5.8), were thus selected for such a comparison across the Plateau and the Mikir Hills and Receiver Functions calculated from data screened by the polarisation analysis projected onto appropriate profiles. Profile-1 of azimuth 69°, traces the northern margin of the Shillong Plateau and crossing the Brahmaputra Valley ends over the Mikir Hills. Profile-2 of azimuth 102°, traces the southern margin of the Plateau and crossing into Bangladesh Plains ends in the Arakan Yomas. Profile-3 of azimuth 36° spans the central Shillong Plateau and the Mikir Hills including a fringe of the Brahmaputra valley (Kopili Lineament), whilst Profile-4 of azimuth 339° is a south- north traverse from the southeastern margin of the Bengal Basin, to the northern Brahmaputra valley, as of Mitra et al. (2005) with the additional inclusion of the NOG station on the northern Shillong Plateau.

Profile-1 TUR–BOK–NOG–BAL–BOR   Profile-3 CHP–BPN–NOG–BAL–BOR–TEZ
Profile-2 TUR–CHP–KMG–MPR   Profile-4 KMG–CHP–SHL–BPN–NOG–GAU–BAI
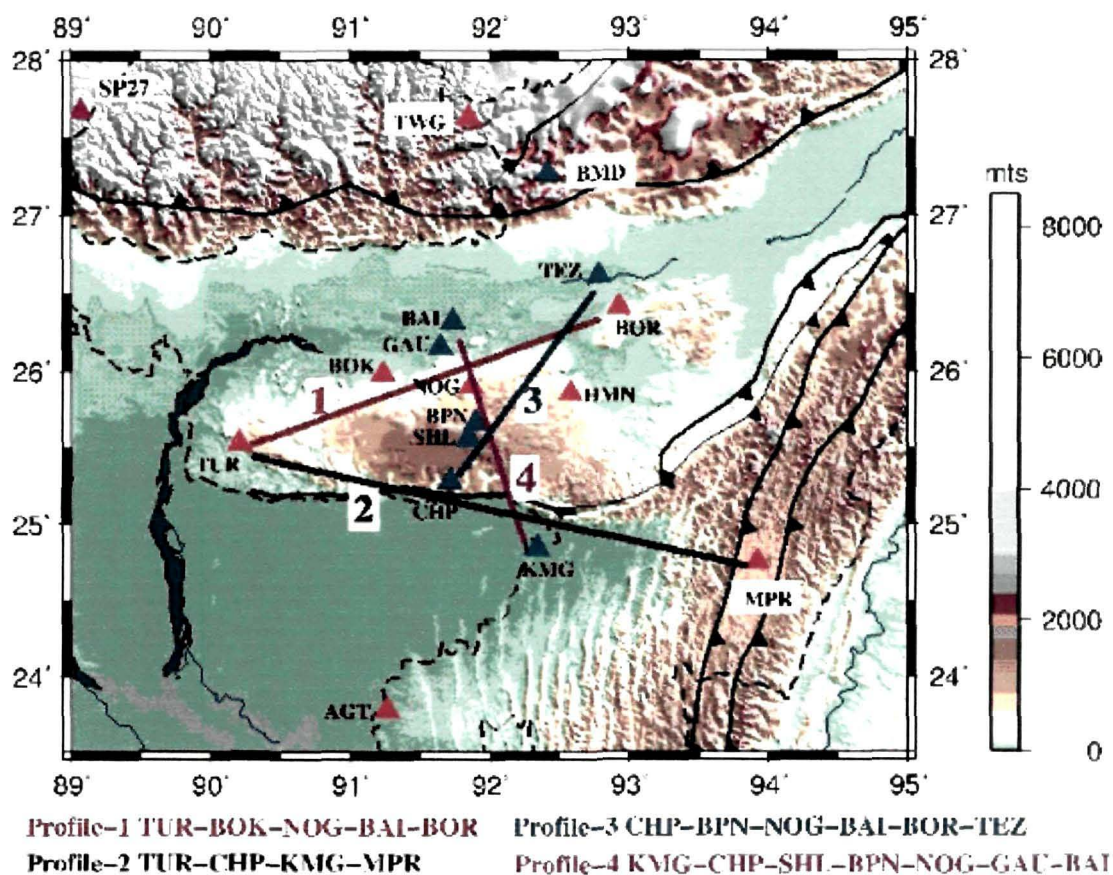
Figure 5.8: Map showing the four profiles through the Shillong Plateau and Mikir Hills, numbered in the text, selected for highlighting the comparative crustal structure of the Shillong plateau with respect to their adjoining regions. Stations along each of the profiles are listed below the map.

As the receiver functions from different back-azimuths have very different path lengths mainly influenced by their great circle arc (GCARC) distances, we eliminated this effect using a simple migration technique to assess the similarities between those pertaining to different back-azimuths. This is accomplished by transforming the various Receiver Functions to a common datum by applying a time stretch factor and an amplitude scale factor with respect to a reference ray parameter. Migrations were performed assuming a single layer crust of average thickness and shear wave speed (Table 5.3)

derived from the results of joint inversions of the receiver functions and surface wave dispersion data. The migrated receiver functions were then plotted as a function of equidistance so that direct comparison of the Moho converted Ps phases could be made for various stations along a particular profile.

Table 5.2: Crustal thickness and shear wave speeds in respect of the various sites, used for performing the migration of Receiver Functions

Station	Average crustal thickness (km)	Average crustal velocity Vs (km/s)
AGT	39	3.60
KMG	38	3.56
CHP-S	44	3.58
CHP-N	37	3.49
SHL	35	3.54
BPN	34	3.52
NOG	33	3.52
BOK	35	3.56
TUR	35	3.65
GAU	40	3.55
BAI	40	3.56
TEZ	40	3.57
BOR	32	3.50

RECEIVER FUNCTION PROFILES
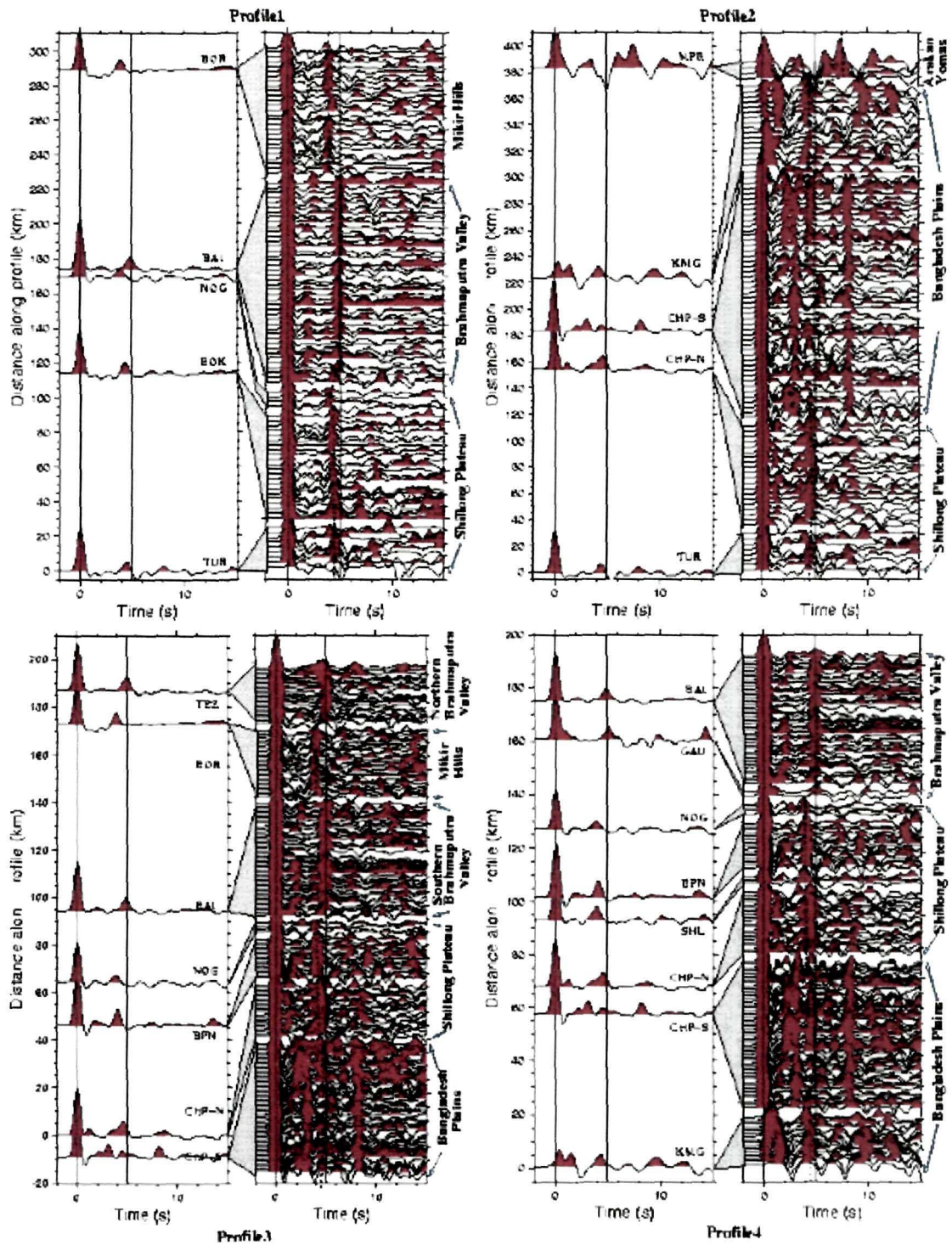
Figure 5.9: Migrated Radial Receiver Functions calculated from teleseismic data generated at stations across the Shillong Plateau and the Mikir Hills are projected onto the respective profiles shown in figure 5.8. Averaged radial receiver functions for the respective profiles are shown on the left on a relative distance scale.

Migrated receiver functions along the four profiles (Figure 5.8) are shown in Figure 5.9 to facilitate comparison of the Moho converted Ps phase arrivals across the Shillong Plateau and the Mikir Hills. Along Profile-1 (azimuth – 69°), the Moho converted Ps phase arrival at the Mikir Hill station is similar to that for the northern Shillong plateau but is demonstrably less than those for the stations in the Brahmaputra Valley. The Moho Ps arrival time along Profile-2 (azimuth - 102°) traversing the southern edge of the plateau is also longer indicating a greater depth for the Moho beneath the Bangladesh plains, which deepens considerably more beneath the Arakan Yomas further east. Along Profile-3 (azimuth - 36°), the longer Ps arrival times at Brahmaputra valley stations implying deeper Moho underneath are flanked by faster arrivals both at the Plateau stations as well as the Mikir Hills- a story reiterated along Profile 4.

Locations of piercing points on the Moho where the Ps conversions of incoming rays take place, provide an insightful view of the Moho geometry. Accordingly, these were also calculated for various event-station pairs and are marked along with the respective stations in Figure 5.10. These locations together with the Moho Ps arrival times for each event and the inverted depths were then used to construct a three dimensional image of the Moho beneath the Shillong Plateau and the Mikir Hills.
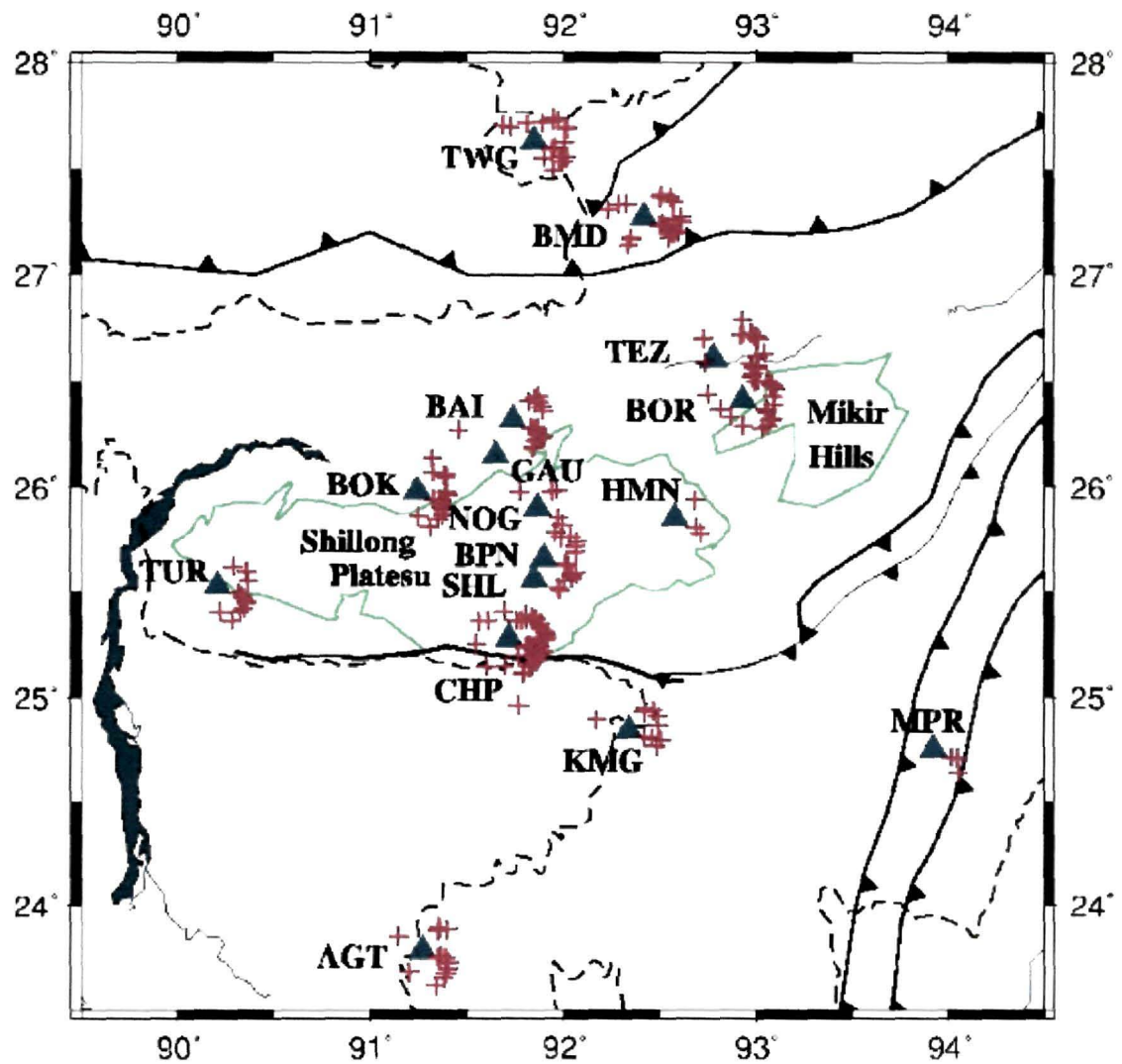
Figure 5.10: Map showing the locations of broadband stations (blue triangles) that provided data for the seismic experiment as well as those of the Moho Ps phase conversion points (red) interfaces for all events used for the study.

5.3.4 Moho Geometry

Figure 5.11 shows the Moho depth beneath the Shillong plateau and the Mikir Hills in relation to its disposition beneath the adjoining terranes. This has

been constructed by combining the variations in the Moho Ps arrival times across the region, the crustal thickness obtained from the joint inversion results and locations of the Moho 'piercing' points. Whilst indications of a shallower Moho in the lower half of the figure on the extreme right is obviously an artifact of the computational scheme, the shallower disposition of the Moho beneath both the Shillong plateau and the Mikir Hills as required by the data, clearly demonstrates that the northeastern Indian shield south of the Himalayan convergence suffered a unique style of deformation not found elsewhere along the collision front. But, even as the exact definition of the causative fault systems that brought this about still remains in being, these results make a very strong case for the existence of mantle reaching faults that mediated the plateau's uplift and continue to absorb some of the Indo-Eurasian convergence with obvious implications to future earthquake hazard potential of the region .
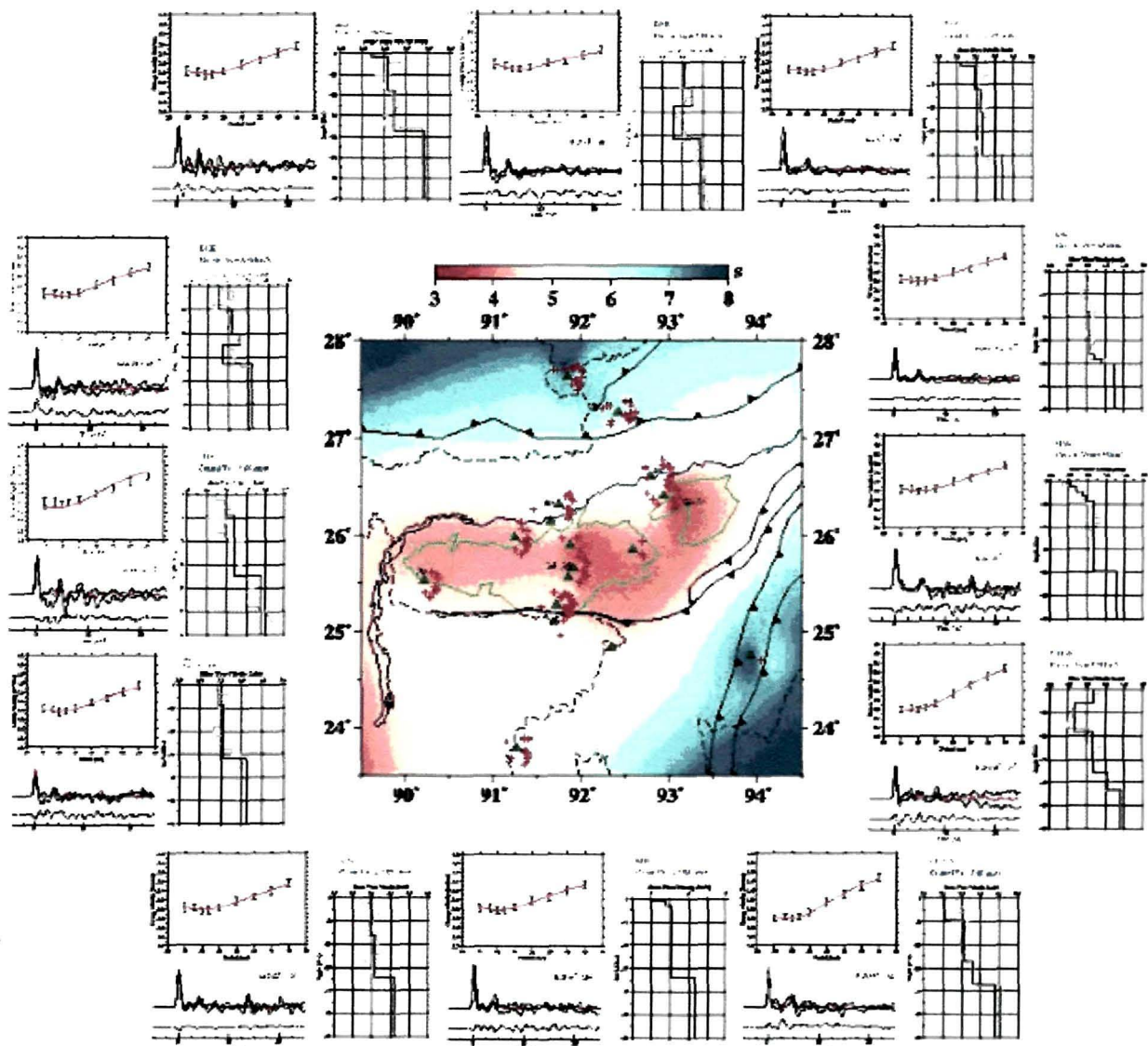
Figure 5.11: Map shows the lateral extent of upwarped Moho beneath the Shillong Plateau and the Mikir Hills (centre). Joint inversion results for each station are also shown together with the receiver function and the surface wave dispersion data used for their determinations. The colour codes represent the Moho converted Ps arrival times of the individual receiver functions used for generating the map.

5.4 Summary and Discussions

Figure 5.11 shows the Moho topography in 3 dimensions beneath two unique tectonic elements of northeastern India: the Shillong Plateau and the Mikir

Hills. The figure also shows the shear wave speed structure beneath different seismic stations in the region obtained from the joint inversion of the receiver functions and Rayleigh wave phase velocity dispersion data calculated for these station sites. The results show a thinner crust beneath the Shillong Plateau and the Mikir Hills (34-35 km) compared with that of the Brahmaputra Valley (40-42 km) to the north and the Bangladesh Plains (40 km) to the south; the maximum Moho depth being observed beneath the Arakan Yomas. The 3-Dimensional image of the Moho beneath the Shillong Plateau shows the lateral extent of the uplifted but a virtually upwarped Plateau. Interestingly, both the crustal shear wave speed structure and the Moho topography beneath the Mikir Hills are quite similar to those of the main Shillong plateau and as distinctly demarcated from the adjoining regions as the main plateau. This clearly demonstrates that not only do these terranes of similar surface petrology and crustal Poisson's ratio have a shared geology and undercarriage but a shared deformation process even as it remains to be defined. Unfortunately, for want of data, these results do not shed any light on a rather significant feature that has long been known to incise the Shillong plateau-Mikir Hills terrain by a north-northwest striking Kopili lineament which is currently highlighted as the seat of the most active seismicity of strike slip and normal fault origin (Kayal et al., 2006) in the wedge between the two fold and thrust belts.

It will be recalled that the relative thickness of the crust beneath the Shillong plateau compared with that of its adjoining regions was argued (Mitra et al., 2005) as being the test bed for discriminating between the hypotheses as to whether the elevation of the plateau was caused and maintained by the thickening of a weak lower crust or by the entire crust being upthrust against mantle reaching faults cutting right through a strong lower crust. Their finding of a thinner crust beneath Shillong was thus interpreted as the result of the uplift of the entire Shillong plateau crust relative to the adjoining

terranes, along mantle reaching faults, whose subsequent erosion had reduced its original thickness.

Although we do not yet know of the degree of isostatic compensation of the Mikir Hills, the distinct identity of its shear wave speed structure and Moho depth strongly suggests that it too was uplifted against mantle reaching faults. This, however, raises new questions about the possible disposition of such a fault system that would in one shot explain the uplift of the northern edge of the Shillong plateau as well as of its north-northeastern extension in the Mikir Hills. The existence of the NNW Kopili lineament that ensues from the inflexion in the Dauki fault-Naga thrust system that bound the plateau on the south and the Mikir Hills on the east, and which is the seat of the most active current seismicity in the wedge between the Himalayan and the Indo-Burman arcs, appears to mark an important mechanical discontinuity in the crust that may connect the two fault systems bounding the plateau and the Mikir Hills on the north, that have uplifted and possibly continue to support both the plateau and the Mikir Hills on their northern boundaries.

Chapter 6

Upper Mantle Structure beneath NE India

This chapter presents the results of our analysis to model the upper mantle and transition zone discontinuities beneath northeastern India using sub-Moho P-to-S converted phases gleaned from 600 broadband seismograms recorded at 15 stations in the region (Figure 6.1). We accomplish this by examining stacked average receiver function traces collected over 1° bins according to their conversion (piercing) point locations calculated at each level of a 2 km discreetly layered earth model. These results are discussed in the light of the regional tectonic framework described in chapter 1.

6.1 Motivation, Aims and Objectives

The upper mantle seismic structure of planet earth is largely characterized by a gradual increase in seismic speeds up to a depth of about 410 km. Thereafter, it is followed by an anomalously high velocity gradient up to the base of the upper mantle at ~660 km. Differential travel times of the converted Ps phases from the 410 and 660 km discontinuities, relative to P, are found to be broadly correlated with surface geology. For example, stations on old shields generally register early arrivals by ~4 seconds, from both the discontinuities compared with those on tectonically younger regions. Gossler and Kind (1996) made a global analysis of SS precursors and suggested that

the upper mantle transition zone underneath the oceans is on average about 14 km thinner than those beneath continents. As petrological phase changes characterize both these discontinuities, this observation is usually interpreted as indicating a cooler transition zone underneath continents compared with those under oceans.   Northeastern India spans a wide range of crustal terranes from its southern oceanic shores to two diverse convergence zones on its north and east with an uncompensated plateau uplift in the middle.   It was therefore suspected that these variously evolved terranes may possibly have distinctive upper mantle seismic expressions and that it may prove instructive to explore and examine their characteristic features, if any, using broadband seismology. Whilst the initiatives through INDEPTH profiles (e.g., Yuan et al., 1997; Kind et al., 2002) provide some insights into the deeper structure and tectonics of the contiguous Tibetan Plateau, few geophysical studies (e.g. Ramesh et al., 2005) have been carried out in the adjoining northeastern India to illuminate the deeper structural make up of this region.

Calculated arrival times of Ps converted phases from the 410 and 660 km discontinuities at an epicentral distance of 67°, for global Earth reference models such as the IASP91, are on average found to be ~41.1s and 68.0s respectively after the direct P-wave arrivals. However, each of these is known to vary in specific regions by as much as ~7.5 seconds, depending on the presence of swells or depressions at these discontinuities (Cheirot et al., 1999) that are, in turn, thought to reflect variations in the ambient mantle temperature.
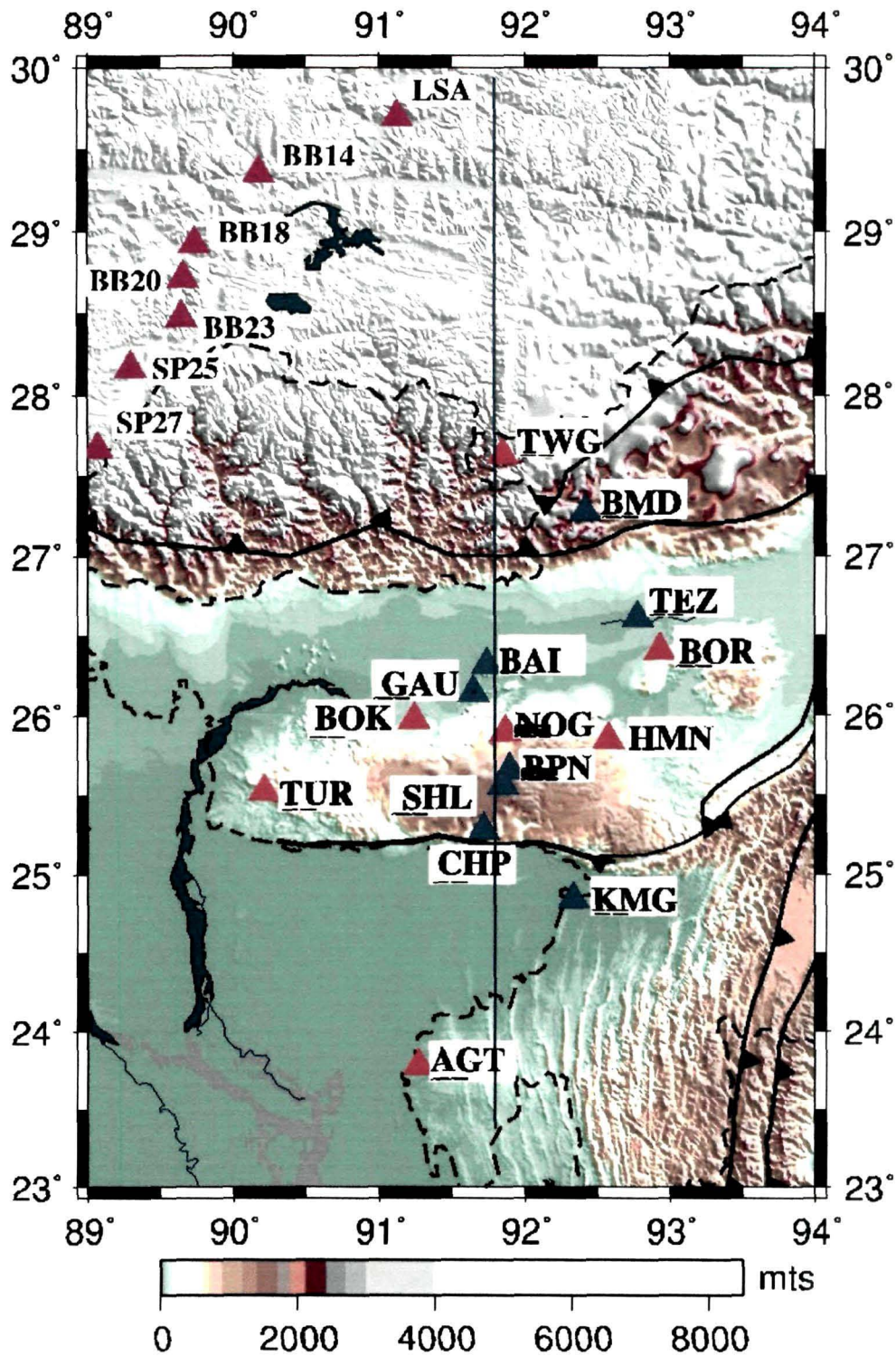
Figure 6.1: Topographic map of Northeastern India and southern Tibet, showing the main tectonic units of the region. Triangles mark the location of broadband seismic stations [blue representing the sites set up by Mitra et al. (2005)., red by the present author, and purple, excluding the Lhasa (LSA) station, by the INDEPTH II group].

600 event-station pairs were used to determine the topography of the 410 and 660 discontinuities beneath NE India and the thickness of the transition zone between them. This chapter presents the results of an analysis of P-to-S converted phases from the upper mantle and transition zone discontinuities using the data generated at 15 sites (Figure 6.1) located in the great Himalya, the Bengal basin as well as sites on the Meghalaya plateau and the Mikir Hills. Converted phases from 410 and 660 discontinuities appearing on the P-wave receiver functions along the N-S profile (Figure 6.1) were analyzed to study the nature of these features compared with their globally defined positions.

6.2 Upper Mantle Seismic Discontinuities

It is generally recognized that mineralogical variations associated with pressure induced phase transformations and/or chemical layering in the upper mantle, determine the radial distribution of seismic velocities and densities of the mantle. Fortunately, their discontinuous variation also marked by acoustic impedance interfaces at depth render them amenable to detection by seismic analysis. The most prominent seismic discontinuities in the upper mantle are constituted by a sequence of phase transformations of olivine to higher-pressure forms at depths of 410 and 660 km producing sharp gradients in the density and velocity of the Earth (Bina and Helffrich, 1994). Another less distinct discontinuity resulting from some combination of β to γ olivine phase transformation and/or transformation of garnet and pyroxene to calcic-perovskite (Revenaugh and Jordan, 1991b) is found to exist at 520 km (Shearer, 1996). Even some less sharp mantle discontinuities above the 410 km discontinuity have also been reported and are of particular interest in understanding the evolution of the upper mantle and its implications to the dynamics of the lithosphere. These, known as the Hales, Gutenberg and Lehmann discontinuities (Green and Hales, 1968; Priestly et al., 1994;

Revenaugh and Jordan, 1991a,b; Revenaugh and Sipkin, 1994; Baumgardt and Alexander, 1984) are briefly outlined below:

6.2.1 The Hales Discontinuity

The Hales discontinuity lies at a depth of ~60 to 90 km and is related to the phase transition from spinel to garnet (Hales, 1969). This discontinuity has been reported by several investigators who found the P-wave velocity to increase by about 3.2% across this discontinuity (Green and Hales, 1968; Hales, 1969; Green and Libermann, 1976; Webb and Wood, 1986).

6.2.2 The Gutenberg Discontinuity

The transition from the uppermost mantle beneath the Moho to the low-velocity-zone (LVZ) is known as the Gutenberg discontinuity. It characterizes the transition from the conductive part of the mantle to its convective regime and specifies the kinematically defined lower boundary of the tectonic plates (Kanamori and Press, 1970; Knopoff, 1983).

6.2.3 The Lehmann Discontinuity

An impedance contrast has also been found to exist near ~220 km depth, called the Lehmann discontinuity and is thought to be related to the compositional change from harzburgite to garnet lherzolite, or the change from garnet lherzolite to elcogite. It is also reported that this discontinuity might be the result of lattice preferred orientation of highly anisotropic olivine crystals in a deformation zone responsible for the mechanical decoupling of the lithosphere from the underlying mantle and thus separates the highly anisotropic lithosphere from a relatively isotropic asthenosphere (Revenaugh and Jordan, 1987). The P- and S- wave velocity increase across

this discontinuity has been found to be about 2% to 4.5% (Anderson, 1989; Gaherty and Jordan, 1995).

6.2.4 The 410 Discontinuity

The seismic discontinuity at ~410 km depth is the most prominent feature in the upper mantle. Its existence is generally attributed to the pressure determined phase transition from the α- olivine to β- wadsleyite of $(Mg,Fe)_2SiO_4$ (Ito and Takahashi, 1989; Bina and Helffrich, 1994). The P-T diagram of the positive slope of the transition indicates that a depression of the discontinuity results from increased temperatures and a swell from colder conditions. The depth disposition of this discontinuity has therefore important implications to our understanding of the nature of subducting slabs and of rising plumes within the Earth's mantle. In the earth reference model IASP91, this seismic discontinuity is marked by an increase in the P- and S-wave speeds of 5%-6% and 4% respectively (Kennett and Engdahl, 1991).

6.2.5 The 520 Discontinuity

The discontinuity at a depth of 520 km (520) is a less prominent feature of the upper mantle. Its existence has been reported by a few authors (e.g. Revenaugh and Jordan, 1991; Dueker and Sheehan, 1998; Deuss and Woodhouse, 2001), but no definitive physical or chemical interpretation has been found to satisfactorily explain its existence.

6.2.6 The 660 Discontinuity

The seismic discontinuity at a depth of approximately 660 km (the 660) is considered by many geologists to constitute a boundary that isolates the upper mantle convection from the lower, forming a veritable barrier to whole mantle convection. Its existence is attributed to an isochemical phase

transformation of ringwoodite (the γ-phase of $((Mg,Fe)_2SiO_4)$ to perovskite $((Mg,Fe)SiO_3)$ and magnesiowusite $((Mg,Fe)O)$ (Anderson, 1967; Ito and Takahashi, 1989; Bina and Helffrich, 1994). It has also been suggested that the discontinuity is associated with a change in chemical composition from an overlying upper mantle dominated by $(Mg,Fe)_2SiO_4$ olivine and spinel materials to a relatively silica-rich lower mantle composed essentially of perovskite (Ringwood and Irifune, 1988). The pressure and temperature conditions of these two transitions are slightly different and therefore occur at different depths. Phase change models suggest density and seismic velocity changes across this discontinuity of about 6%-11% (Christensen, 1995).

6.3 Data

Three component broadband seismic data were generated at 12 sites in northeastern India by the Tezpur University under a collaborative project with the Indian Institute of Astrophysics at Bangalore, Indian Institute of Technology at Kharagpur and the University of Cambridge (UK). Additionally, data generated by DST sponsored stations operated by the NGRI, IMD and Gauhati University, were also used. Seismographs at Agartala (AGT) and Karimganj (KMG) were located on the sediments of the Bengal Basin south of the Shillong Plateau; those at Cherapunji (CHP), Shillong (SHL), Barapani (BPN), Tura (TUR), Nongpoh (NOG), Hamren (HMN) on the exposed Precambrian crystalline basement of the Shillong Plateau, and at Baihata (BAI), Guwahati (GAU), Boko (BOK) and Tezpur (TEZ) on the low-lying basement ridges (foreland spur) in the Brahmaputra Valley, and at Borjuri (BOR) on the Mikir Hills. The Bomdila (BMD) site is located on bedrock in the Lesser Himalayas a few kilometers south of the MCT, and Tawang (TWG) in the Greater Himalayas north of the MCT (Figure 6.1).

6.4 Results

6.4.1 The 410 and 660 km Discontinuities beneath NE India: Receiver Function Analysis of Teleseismic Earthquake Data Recorded at 15 NE Indian Stations

Analysis of P-to-S converted waves at upper mantle discontinuities that appear in the P-wave coda, is a well-known approach to investigate these discontinuities beneath a seismic station (Vinnik, 1977). Receiver functions are calculated from three-component seismograms (Ammon, 1991) as described in an earlier chapter. The observed waveform is a composite of P-to-S converted waves that reverberate beneath the seismometer. These conversions occur when an advancing wave is transmitted or reflected at an acoustic impedance boundary in the earth's interior. Receiver functions are thus marked by an arrival time peak corresponding to the direct P-wave, that is, its horizontal component, followed by peaks and troughs marking the Ps and other multiply reflected arrivals.

Broadband seismograms corresponding to 600 event-station pairs were used to determine the topography of the 410 and 660 discontinuities beneath NE India and the thickness of the transition zone between them. Accordingly, we isolated all high signal-to-noise ratio seismograms at each of the 15 sites pertaining to M ≥ 5.5 earthquakes located within the 30°-90° distance range and abstracted therefrom a 160 seconds long signal, 30 seconds before the direct P arrival and 130 seconds after it. Receiver functions were calculated from all such pre-selected 3-component seismogram segments using the iterative, time-domain deconvolution approach (Ligorria and Ammon, 1999). The technique and the analysis procedure are detailed in chapter 3. The Gaussian width employed in this study was set to 0.6.

In order to stack the data coherently, one needs to correct for variations in the arrival times or normal move outs associated with the different source-receiver separations. Ideally, these are calculated by ray tracing through a three-dimensional velocity model of the shear and compressional velocity structure. But in practice, these corrections can be predicted accurately enough by assuming a one-dimensional reference model such as the IASP91.

However, since the travel time curves of the converted phases in the P-wave coda originating at different depths are not parallel to that of the direct P wave and their slowness decreases with increasing conversion depths, the distance move-out correction is made with reference to a fixed epicentral distance, which has the effect of rendering all these travel time curves parallel to the P curve. The fixed distance chosen for this study was set at 67°. Time scales of seismograms from larger distances were therefore stretched and those from shorter distances, compressed. This results in producing images similar to those in the seismic reflection processing, making it possible to display conversions from all depths in a single figure with all conversions paralleling the P-wave trajectory as in a flat-layered earth. In this study, the distance move-out corrections were made using the IASP91 Earth reference model.

Figure 6.2 and Figure 6.3 show all the processed traces plotted at equal spacing from south to north beginning from the station at Agartala (AGT) and ordered first according to station location and then according to back-azimuth running clockwise from north at the top. The summation trace is also displayed above the individual traces in Figure 6.2 to highlight the main phases which are consistent over the entire NS profile (Figure 6.1), the timescale being the delay time with respect to the P-phase at the 67° epicentral distance. Amongst all the traces so constructed, hardly any clear signal is observed other than those from the 410 and 660 km discontinuities in the upper mantle which are both quite clear over the entire profile. The

theoretical travel times of the IASP91 reference Earth model for 410 and 660 km discontinuities are marked in the figure by thin black lines.
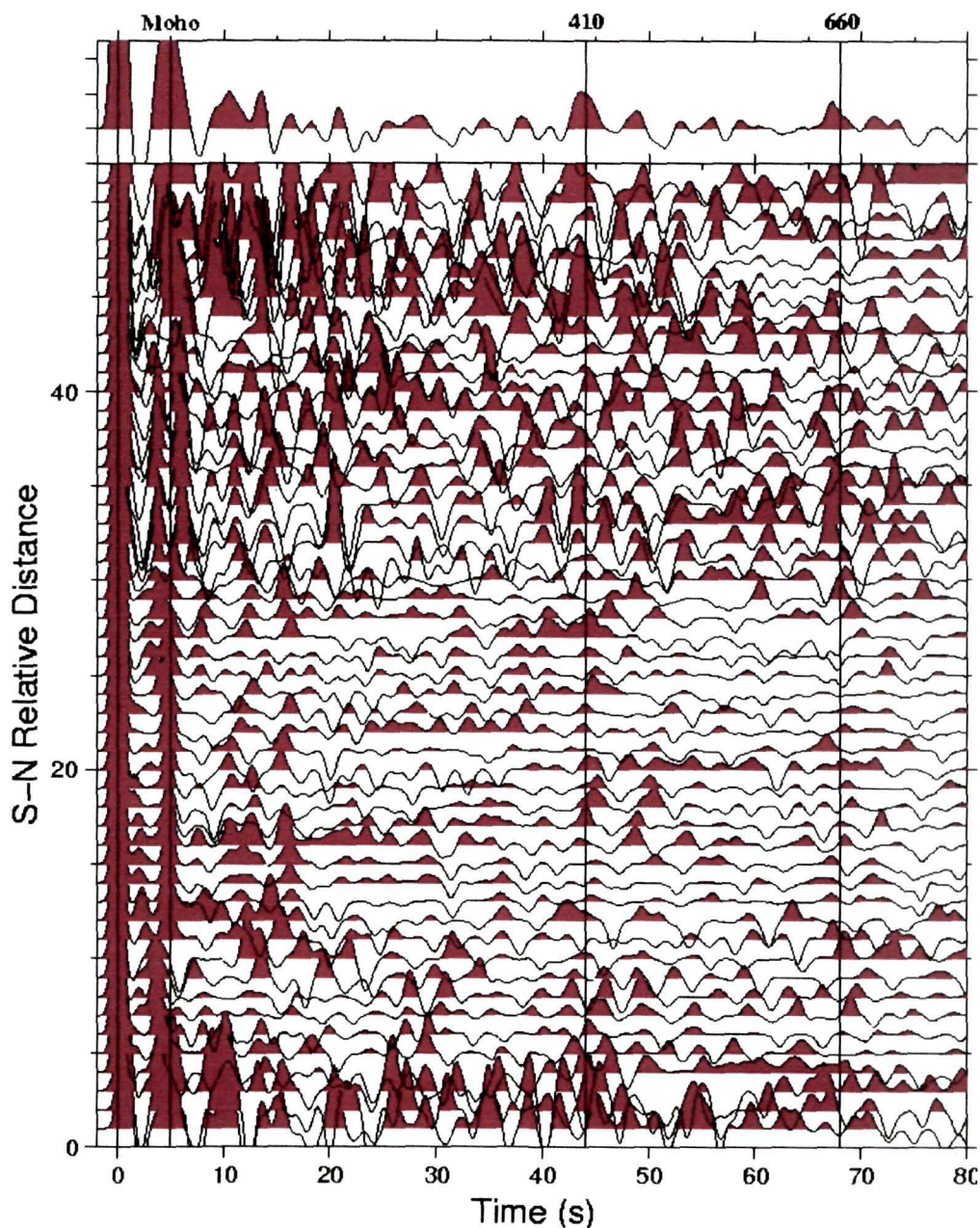
Figure 6.2: Plot of the receiver functions recorded at seismic stations in NE India. Receiver functions are distance move-out (67°) corrected for P-to-S converted waves underneath the stations and plotted equally spaced from south to north sorted by station distance from the southern-most station at Agartala, and then by backazimuth. The summation of all traces is shown at the top. The black lines around the 410 and 660 km conversions belong to the IASP91 global reference model.
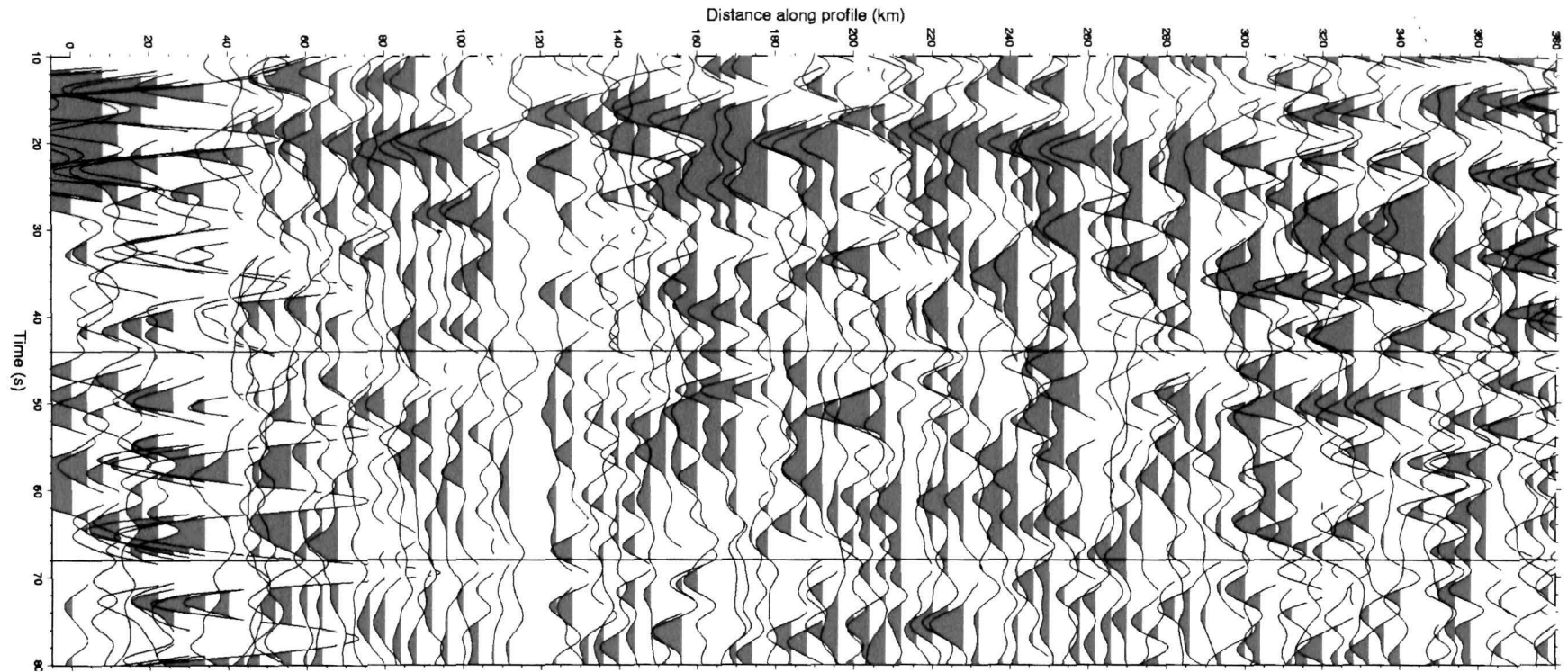
Figure 6.3: Plot of 20 to 80 seconds of the receiver functions of the broadband seismic data of NE India. The traces are moveout corrected to a distance of 67° and plotted equally spaced from south to north sorted by station distance. The converted phases from 410 and 660 discontinuities are labeled according to the IASP91 global reference model. The vertical axis shows the delay time of the various conversions while the horizontal axis represents the relative distance scale along the south-north profile (Figure 6.1) starting from Agartala (AGT).

Further, a ray tracing of the receiver functions was also performed to image lateral variations, if any, in the depths to significant velocity discontinuities in the region, using the ray parameter of the P wave through the IASP91 reference model to different depths (i.e. 410 and 660 km). The conversions from the 410 and 660 km discontinuities seen in the ray-tracing plot are shown in Figure 6.4.
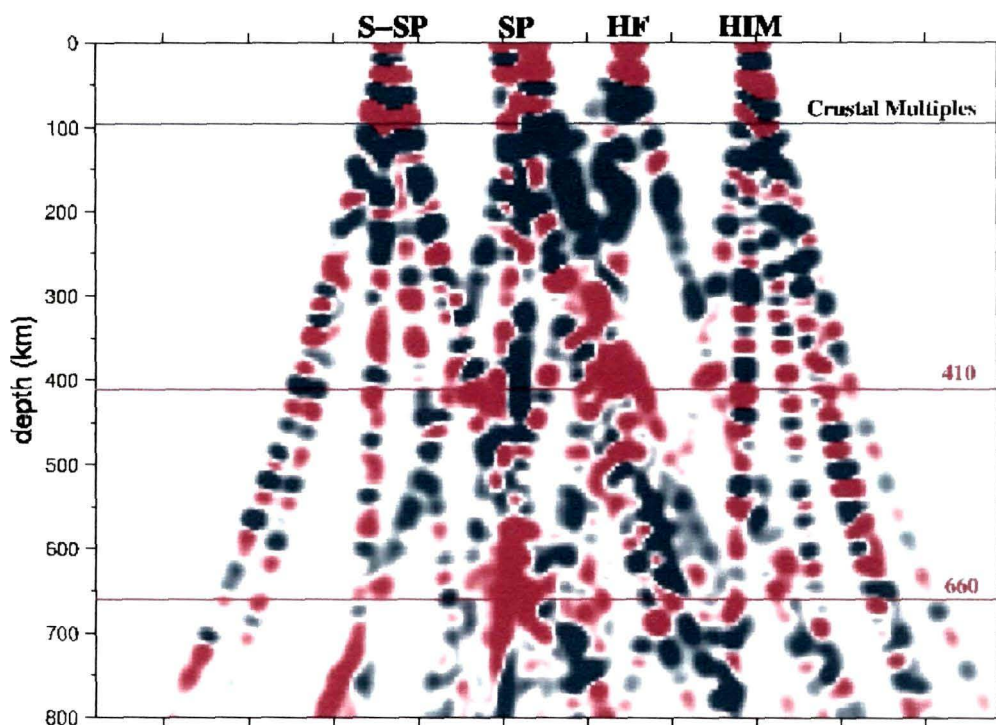
Figure 6.4: Converted S-wave ray set. The rays are traced through the one-dimensional reference model IASP91 and projected onto the plane beneath the SN profile (Figure 6.1). The 410 and 660 discontinuity marked in the figure (thin red lines) are taken from the IASP91 reference model. The vertical axis denotes depths in km below the surface and the horizontal axis shows the four clusters, such as S-SP (south of Shillong Plateau), SP (Shillong Plateau), HF (Himalayan Foredeep/Brahmaputra Valley) and HIM (Himalayas), of stations in the four significant geologic terranes of the NE India region. The positive and negative arrivals of the traces are denoted by red and blue colour respectively in the figure.

6.4.2 Transition Zone Thickness: Three-dimensional Stacking of Receiver Functions to determine lateral Variations in the thickness of the Mantle Transition Zone beneath NE India

There is a significant problem to be obviated in stacking the records of converted phases produced by different events because local disruptions or inclination of these discontinuities would have the effect of highlighting apparent rather than actual depths depending on the location of these events. Therefore, we adopted a 3-D stacking method to enhance the P-to-S converted phases contained in the coda of the teleseismic P and PP phases, that enables one to identify lateral variations in the depth levels of the 410 and 660 km discontinuities in the upper mantle.

The main objective of the 3-D approach is to stack rays to enhance the ratio of signal to noise and thereby to improve their resolving power for distinguishing lateral variations in the structures of mantle discontinuities. Accordingly, the travel times of P to S converted phase(s) corresponding to each station-event pair and its piercing point were calculated for each depth level every 2.5 km from 40 to 800 km depth. Further, corresponding theoretical Ps-P arrival times were also calculated assuming a single P ray converted to-S in the standard IASP91 reference earth model which associate a given time instant in each receiver function with a specific corresponding point in the subsurface. Binning of rays by their piercing points at each depth level is performed using variable radius (0.5-1.0°) circular bins. Their amplitudes at the appropriate (Ps-P) time for each receiver function piercing a particular bin are then summed to produce the stack.
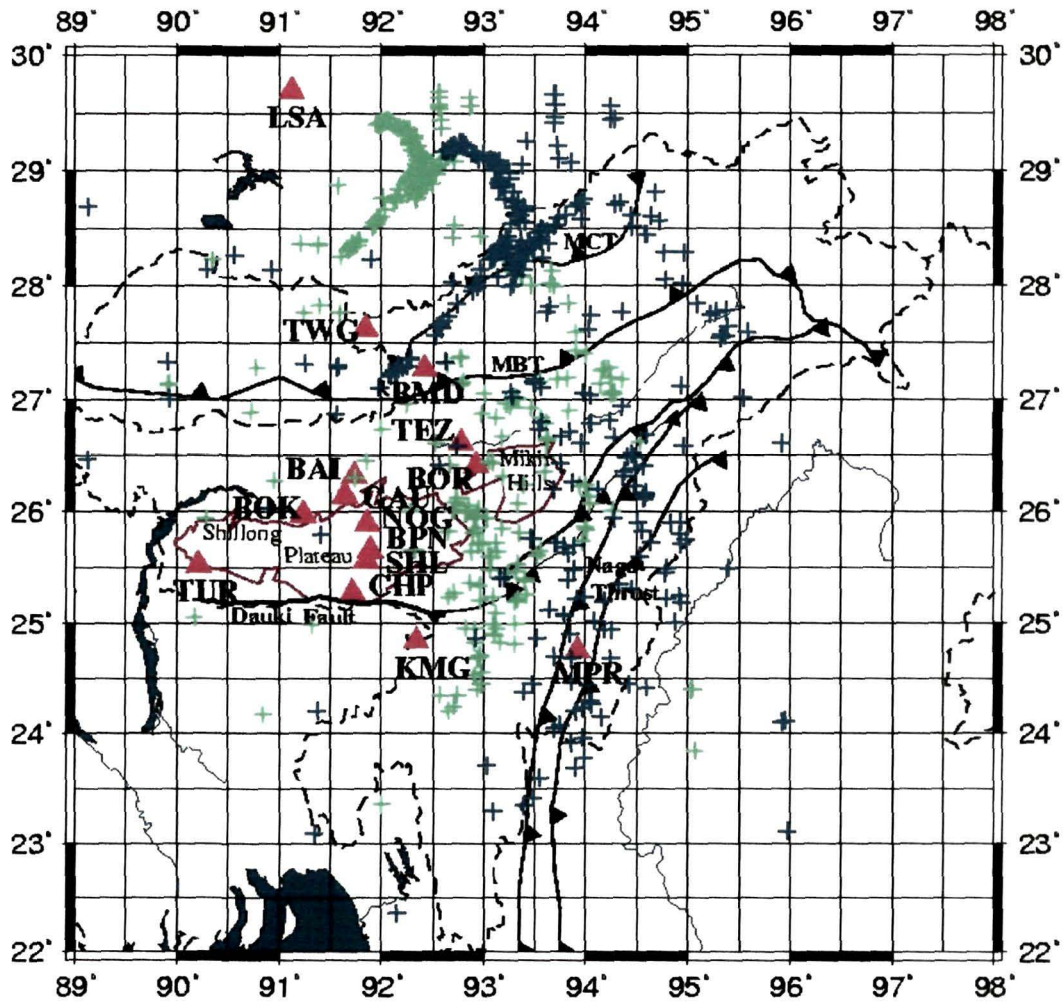
Figure 6.5: Location map of broadband stations of the seismic experiment also showing the distribution of piercing points at 410 km (green crosses) and 660 km (blue crosses) interfaces for all events used for this study. Major tectonic features of the region are also marked in the figure.

The 410 and 660 km discontinuities produced strong Ps conversions across the study area and were easily traceable. The differences between the depths of the maximum amplitude stack with respect to the 410 and 660 discontinuities across the entire region were calculated to study the lateral variations in the underlying transition zone thickness (TZT).

The depth of the 410 km discontinuity underneath the eastern Himalayas was found to be the shallowest. It appeared to deepen by 10-15 km beneath the southern parts of the region. In contrast, the 660 km discontinuity across the whole region was found to lie quite close to its designated depth as in the IASP91 reference model, a feature more consistent beneath the N-S profile. Little evidence was found of the existence of the 520 km discontinuity in the region.
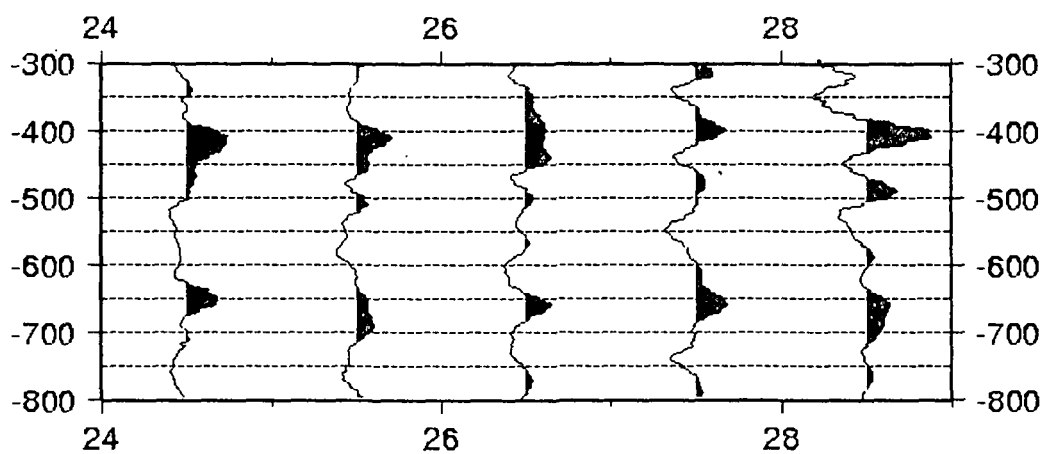
Figure 6.6: 3D-stacked traces of receiver functions averaged over 1° latitude intervals according to their piercing point locations at 410 and 660 km depth interfaces. The depths, in km, are shown along the Y-axis whilst the X-axis represents latitudes considered as the bin center.

Clapeyron slopes of the phase transformations at 410 and 660 km depth are inversely correlated: lower (higher) than average temperatures elevate (depress) the 410 while the opposite is expected for the 660 as suggested by experimental results (Ito and Takahashi, 1989; Bina and Helffrich, 1994). Consequently, the thickness of the transition zone between these discontinuities will depend on the mantle temperature of the region so that the transition zone is expected to be thinner in warmer regions than in cooler

ones. Accurate determinations of the depth to these discontinuities thus enables one to estimate the thermal state of the transition zone in the region.

Figure 6.7 presents estimated variations in the depths of the 410 and 660 discontinuities in the NE India region with respect to their globally average depths. Variations in the Ps arrival times from 410 and 660 discontinuities in combination with the locations of the piercing points at these interfaces were used to determine the three-dimensional topography of the 410 and 660 discontinuities in the upper mantle across the study region. The thickness of the transition zone beneath the study region was determined by simply calculating the differences between the depths of the 410 and 660 discontinuities. It was observed that the thickness of the transition zone beneath the region varies within a ±25 km range of the standard global average of ~250 km. On the other hand, Figure 6.8 indicates that the transition zone is thickest beneath the Himalaya, implying that the mantle beneath the region is colder than in other parts of the region.
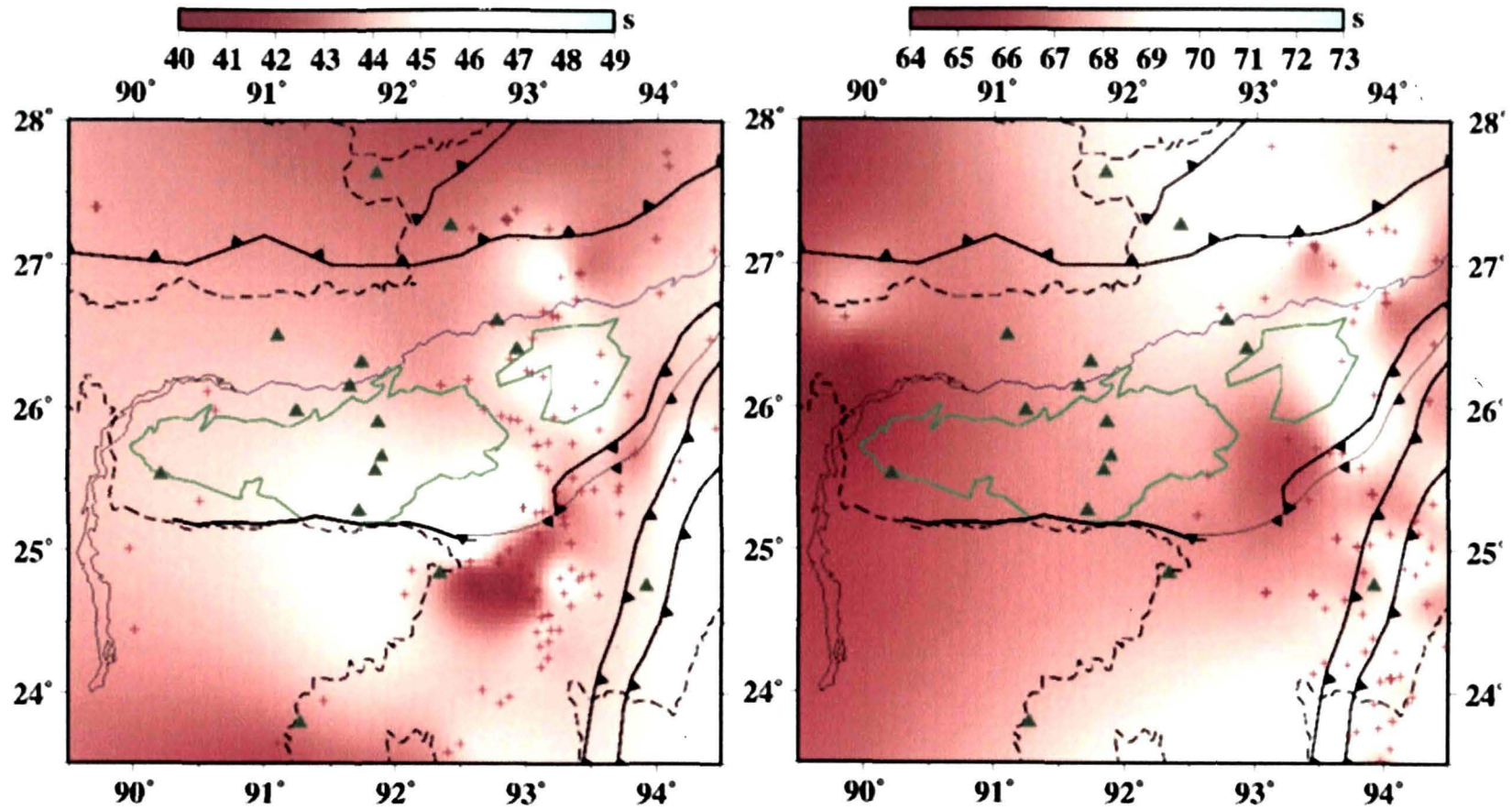
Figure 6.7: Topography at 410 (left) and 660 (right) discontinuities beneath the NE India region. Colour patterns towards the blue denote relatively later arrival time of the converted Ps phase from 410 and 660 discontinuities. Red crosses on the plates denote the locations of piercing points sampling the 410 and 660 discontinuities, whilst the triangles denote the location of seismic stations. Latitudes and longitudes of the region are shown in the Y- and X-axis respectively.
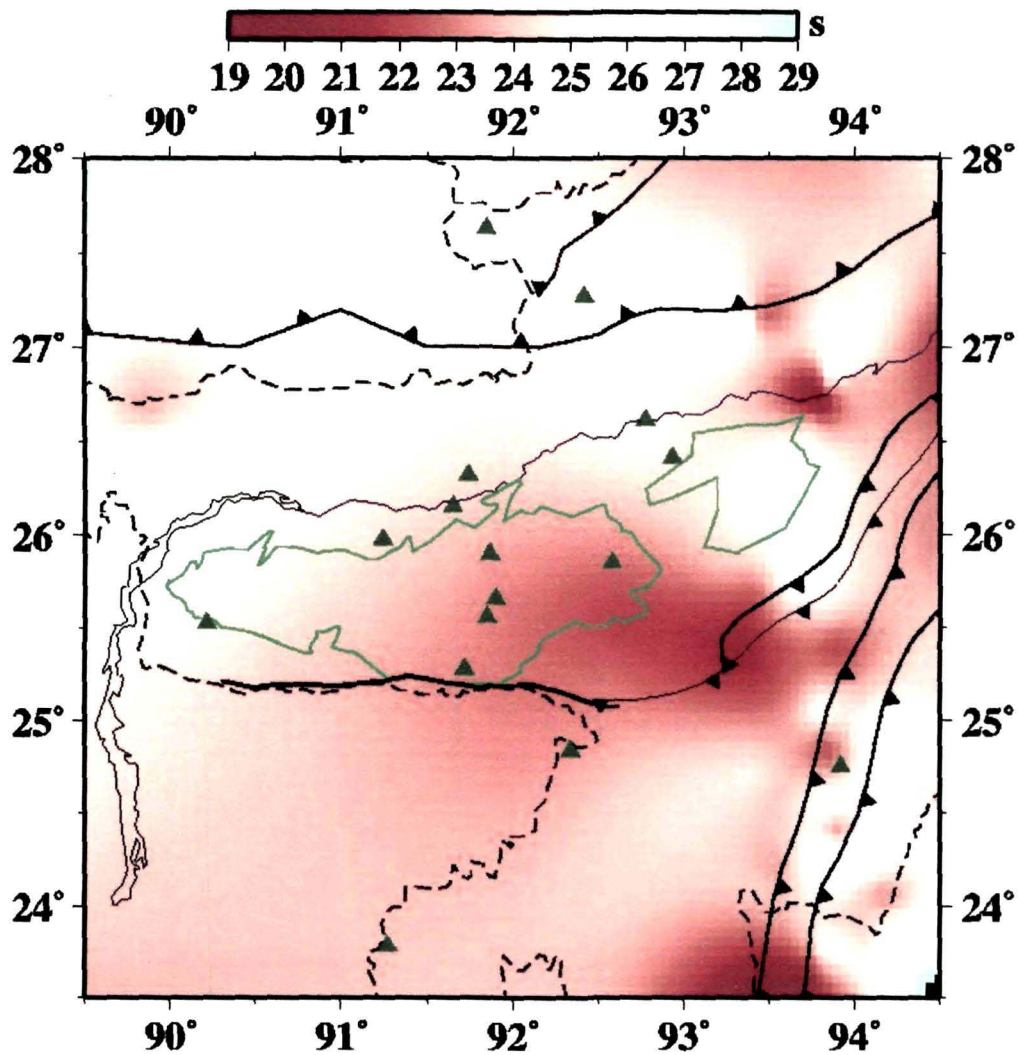
Figure 6.8: Thickness of the transition zone between 410 and 660 discontinuities. The thickest transition zone is observed beneath the Himalayas, indicating a relatively   colder transition zone beneath the Himalayas. The X and Y - axes denote the longitudes and latitudes respectively.

6.5 The Upper Mantle Structure beneath NE India- a summary

The foregoing analysis of converted phases from mantle discontinuities beneath NE India, clearly bring out the existence of the 410 and 660 km

discontinuities in the upper mantle of the region and their congruence with the globally averaged depths, with occasional local swerves in the 410 km discontinuity.

The near constancy of the mantle transition zone thickness throughout the region, by implication, suggest that no significant anomalous structures exist beneath the region and that it is similar to that as found further north in Tibet (Yuan et al., 1997).

Our results, thus, affirm that the lithospheric mantle of the region does not have significant thermal anomalies either within or above the transition zone, testifying to the s olid nature of the Indian lithosphere even in the region of the Indo-Tibetan collision zone.

Chapter 7

Discussion and Conclusions

Availability of broadband seismic data from northeast India region have made it possible to investigate the major seismic characteristics such as the shear wave speed structure, Moho depth, upper mantle discontinuity and seismic anisotropy in the crust beneath i) the ~1 km high Archaean Shillong plateau and its northeastern extension in the Mikir Hills, ii) the Himalaya, iii) the intervening plains including the foreland spur of exposed archaeans in the Brhmaputra valley, and iv) the Bengal basin. In this work I analysed the P-to-S converted phases and shear-wave splitting observations to constrain the crust and upper mantle structure and anisotropic parameters beneath the various geomorphic features in NE India region.

A total of 14 stations of NE India were modeled, six of them for the first time and the eight others were modeled based on much expanded data set as compared to the earlier Mitra et al. (2005) study. Data from the CDSN station at Lhasa (LSA) and six INDEPTHII (Yuan et al., 1997) seismographs were also used to determine the crustal structure beneath the great Himalaya and southern Tibet and an attempt was made to make a comparison with the crustal structure in NE India.

Accordingly, this chapter begins by summarising the results presented in chapters 4, 5 and 6. These findings are then integrated with other geophysical studies carried out in the region to improve our understanding of the deep structure beneath the region. As highlighted in the chapter one,

there were several questions to be answered: (i) the unusual structural feature constituted by the Shillong plateau in the compressive regime of Indo-Eurasian collision and its deeper (greater than ~20 km) seismic activity, (ii) the tectonic response of NE India to Indo-Eurasian collision as exhibited by its geomorphic and seismic expressions which is significantly different from that of the more western segments of the Himalayan arc, and (iii) unlike Himalayan foredeeps and river valleys in the west which are bordered by undeformed Precambrian terranes of the Indian shield, NE India region is bordered by a ~100 km wide and 1 km high plateau of the Indian shield rocks apparently uplifted and dynamically sustained by reverse faults, the southern of which also marks a transition to a more oceanic type crust underlain by the Bengal basin. The following discussion attempts to address these problems, identifies questions for future work, and concludes with a possible construction of the lithospheric structure beneath NE India in light of the latest research.

7.1 Summary of findings

- ## Chapter 4

  - The result shows a crustal thickness of 38-40 km beneath the southernmost site located at Agartala close to the Bay of Bengal, with a 5 km thick very high velocity layer (S-wave velocity 4.9 km/s) immediately above the Moho, most likely indicating the existence of the oceanic crust south of the Bengal Basin hinge zone.

  - The Moho beneath the Shillong Plateau is 34-36 km deep with a crustal structure typical of the Indian shield.

- To the north of the plateau the crust thickens to 42-44 km beneath the Brahmaputra Valley, to 48-50 km beneath the Lesser Himalaya, and 55-57 km below the site located at Tawang in the Great Himalaya.

- To the north of the Great Himalaya beneath the southern Tibetan Plateau, the Indian Moho continues to dip northward at 6° reaching a depth of ~90 km beneath Lhasa.

- The crustal structure of the NE India is also characterized by the presence of strong seismic anisotropy in the crust. The azimuth of anisotropy is well correlated with the direction of the geological trend in the region.

• **Chapter 5**

- The results show a thinner crust beneath the Shillong Plateau and the Mikir Hills (34-35 km) compared to the Brahmaputra Valley (40-42 km) to the north and Bangladesh Plains (40 km) to the south. Maximum Moho depth is observed beneath the Arakan Yomas. The 3-Dimensional image of the Moho beneath the Shillong Plateau enables in constraining the lateral extent of the upwarp of the Plateau, which had been observed only along a NS profile by Mitra et al (2005).

- There is a close match between the upwarped Moho and the topography across the Shillong Plateau and Mikir Hills. This further substantiates the fact that the Plateau is popped-up due to the continued collision between the Indian Plate and the Tibetan Plate (Bilham and England 2001).

- The similarity in crustal thickness and close spatial positions of the Shillong Plateau and Mikir Hills do suggest similar fault generated uplift for both regions. Observations of Moho depths (piercing points) between the two regions are therefore required to understand the role of the seismically active Kopili lineament in the plateau uplift process.

• Chapter 6

- The analysis of converted phases from mantle discontinuities beneath NE India, clearly bring out the existence of the 410 and 660 km discontinuities in the upper mantle of the region and their congruence with the globally averaged depths, with occasional local swerves in the 410 km discontinuity.

- The near constancy of the mantle transition zone thickness throughout the region, by implication, suggest that no significant anomalous structures exist beneath the region and that it is similar to that as found further north in Tibet (Yuan et al., 1997).

- Our results, thus, affirm that the lithospheric mantle of the region does not have significant thermal anomalies either within or above the transition zone, testifying to the stolid nature of the Indian lithosphere even in the region of the Indo-Tibetan collision zone.

7.2 Final Conclusions

By considering all of the research presented in this thesis together with other geological and geophysical considerations it is possible to make the following statements:

- The findings provide evidence of a progressive northward deepening of the Indian crust Moho beneath Himalaya and Tibet.

- There exists an oceanic type structure of the Bengal basin crust.

- The findings provide evidence of a relatively undisturbed Moho beneath this extraordinary geomorphic feature of the globe.

- They provide a test of the hypotheses that the entire Shillong Plateau crust has been uplifted along mantle reaching faults and that its ~1 km high uncompensated topography is maintained dynamically by reversed faults (Bilham & England, 2001) engineered by the India-Eurasian collision.

- The findings also suggest that the lithospheric mantle of the region does not have significant anomalous structure even in the vicinity of an ongoing collision of India into Eurasia.

7.3 Future Scope of Work

The results of this thesis have helped to improve our understanding of the nature of the lithospheric structure beneath the NE India region. The remaining questions about the seismically active Kopili lineament could be

best addressed by the collection of more data on and around the Shillong Plateau and Mikir Hills. This would improve our understanding of the structure of the less elevated Mikir Hills and the role of the seismically active Kopili lineament in the plateau uplift process. Achievements of much tighter constraints on the quantities than obtained here would remain a continuing research goal as more homogeneous data with better azimuthal coverage becomes available in the future to develop unambiguous petrological and geodynamic models of the evolution of the various tectonic features in the NE India.

References

Ammon, C. J., The isolation of receiver effects from teleseismic P waveforms, *Bull. Seismol. Soc. Am.*, *81*, 2504-2510, 1991.

Ammon, C., Randall, G. & Zandt, G., On the nonuniqueness of receiver function inversions, *J. Geophys. Res.*, *95*, 15 303-15 318, 1990.

Anderson, D., *Theory of the Earth*, Blackwell Scientific Publications, 1989.

Babuska, V. and Cara, M., *Seismic Anisotropy in the Earth*, Kluwer Academic Publishers.

Babuska, V., Plomerova, J. and Sileny, J., Models of seismic anisotropy in the deep continental lithosphere, *Phys. Earth Planet. In.*, *78*, 167-191, 1993.

Baranowski, J., Armbruster, J., Seeber, L. & Molnar, P., Focal depths and fault plane solutions of earthquakes and active tectonics of the Himalaya, *J. Geophys. Res.*, *89*, 6918-6928, 1984.

Benz, H. and Vidale, J., Sharpness of upper-mantle discontinuities determined from high-frequency reflections, *Nature*, *365*, 147-150, 1993.

Bilham, R., and England, P., Plateau pop-up in the 1897 Assam earthquake, *Nature*, *410*, 806-809, 2001.

Bilham, R. *et al.*, GPS measurements of present-day convergence across the Nepal Himalaya, *Nature*, *386(6620)*, 61-64, 1997.

Bina, C. and Helffrich, G., Phase transition clapeyron slopes and transition zone seismic discontinuity topography, *J. Geophys. Res.*, *99*, 15853-15860, 1994.

Bina, C. R., Mantle Discontinuities, *Review of Geophysics, Supplement*, pages 1987-1990.

Birch, F., The velocity of compressional waves in rocks to 10 kilobars, *J. Geophys. Res.*, *66*, 2199-2224, 1961.

Bock, G. and Kind, R., A global study of S-to-P and P-to-S conversions from the upper mantle transition zone, *Geophys. J. Int.*, *107*, 117-129, 1991.

Bokelmann, G., P-wave array polarisation analysis and effective anisotropy of the brittle crust, *Geophys. J. Int.*, *120*, 145-162, 1995.

Bowman, J. R. and Ando, M., Shear-wave splitting in the upper mantle wedge above the Tonga subduction zone, *Geophys. J. R. Astr. Soc.*, *88*, 25-41, 1987.

Chen, W. P. & Molnar, P., Seismic moments of major earthquakes and the average rate of slip in Central Asia, *J. Geophys. Res.*, *82*, 2945-2969, 1977.

Chen, W. P. & Molnar, P., Focal depths of intracontinental and intraplate earthquakes and their implications for the thermal and mechanical properties of the lithosphere, *J. Geophys. Res.*, *88*, 4183-4214, 1983.

Chen, W. P. & Molnar, P., Source parameters of earthquakes and intraplate deformation beneath the Shillong Plateau and northern Indoburman ranges, *J. Geophys. Res.*, *95*, 12527-12552, 1990.

Chen, W. P. and Ozalaybey, S., Correlation between seismic anisotropy and Bouguer gravity anomalies in Tibet and its implications for lithospheric structures, *Geophys. J. Int.*, *135*, 93-101, 1998.

Chevrot, S. and Hilst, R., The Poisson ratio of the Australian crust: Geological and Geophysical implications, *Earth Planet. Sc. Lett.*, *1-2*, 121-132, 2000.

Chevrot, S., Vinnik, L. and Montagner, J., Global scale analysis of the mantle Pds phases, *J. Geophys. Res.*, *104*, 20203-20219, 1999.

Christensen, M., Poisson's ratio and crustal seismology, *J. Geophys. Res.*, *101*, 3139-3156, 1996.

Christensen, M. and Mooney, W., Seismic velocity structure and composition of the continental crust – A global view, *J. Geophys. Res.*, *100*, 9761-9788, 1995.

Christensen, U., Effects of phase transitions on mantle convection, *Annu. Rev. Earth Planet. Sci.*, *23*, 65-87, 1995.

Crampin, S., The dispersion of surface waves in multilayered anisotropic media, *Geophys. J. R. Astr. Soc.*, *21*, 387-402, 1970.

Crampin, S., Evaluation of anisotropy by shear wave splitting, *Geophysics*, *50*, 142-152, 1985.

Crampin, S., Stephen, R. and McGonigle, R., The polarisation of P-waves in anisotropic media, *Geophys. J. R. Astr. Soc., 68,* 477-485, 1982.

Das Gupta, A. & Biswas, A., *Geology of Assam,* Geological Society of India, Bangalore, 2000.

De, R. & Kayal, J., Crustal *P*-wave velocity and velocity ratio study in northeast India by a microearthquake survey, *Pure Appl. Geophys., 134(1),* 93-108, 1990.

Deuss, A. and Woodhouse, J., Seismic observations of splitting of mid-transition zone discontinuity in Earth's mantle, *Science, 294,* 354-357, 2001.

Du, Z. J. and Foulger, G. R., The crustal structure of northwest Fjords, Iceland, from receiver functions and surface waves, *Geophys. J. Int., 139,* 419-432, 1999.

Dziewonski, A. M. and Anderson, D., Preliminary Reference Earth Model, *Phys. Earth Planet. In., 25 (4),* 297-356, 1981.

Dziewonski, A. M. and Anderson, D., Travel Times and Station Corrections for P waves at Teleseismic Distances, *J. Geophys. Res., 88,* 3295-3314, 1983.

Ekström, G., A broad band method of earthquake analysis, *PhD thesis,* Harvard University, Cambridge, MA, 1987.

Farra, V. and Begat, S., Sensitivity of qP-wave traveltimes and polarisation vectors to heterogeneity, anisotropy and interfaces, *Geophys. J. Int., 121,* 371-384, 1995.

Farra, V. and Vinnik, L., Upper mantle stratification by P and S receiver functions, *Geophys. J. Int., 141,* 699-712, 2000.

Gaherty, J. and Jordan, T., Lehmann discontinuity as the base of an anisotropic layer beneath continents, *Science,* pages 1468-1471, 1995.

Gansser, A., *Geology of the Himalayas,* InterScience, London, 1964.

Gaur, V. & Bhattacharji, J., *Gravimetric Determination of the Shape of Moho in Peninsular and NE India,* IUGG, XVIII General Assembly, Hamburg, Germany, 15-27 August 1983, 936p, 1983.

Goldberg, D. E., Genetic *Algorithm in Search, Optimization, and Machine Learning,* Addison-Wesley Publishing Company, Inc, 1989.

Goodwin, A., *Precambrian Geology: The Dynamic evolution of the continental crust*, Academic Press, London, 1991.

Gowd, T., Rao, S. and Gaur, V., Tectonic stress field in the Subcontinent, *J. Geophys. Res.*, 97, 11879-11888, 1992.

Green, D. and Hales, A., The traveltime of p waves to 30° in central united states and upper mantle structure, *B. Seismol. Soc. Am.*, 58, 267-289, 1968.

Green, D. and Libermann, R., Phase equilibria and elastic properties of a pyrolite model for the oceanic upper mantle, *Tectonophysics*, 32, 61-92, 1976.

Gupta, S., Rai, S, Prakasham, K., Srinagesh, D., Bansal, B., Chanda, R., Priestly, K. and Gaur, V., The nature of South Indian crust: Implications for Precambrian crustal evolution, *Geophy. Res, Lett.*, 1, 2003.

Gurrola, H., Baker, G. and Minster, J. B., Simultaneous time-domain deconvolution with application to the computation of receiver function, *Geophys. J. Int*, 120, 537-543, 1995.

Hallet, B. & Molnar, P., Distorted drainage basins as markers of crustal strain east of Himalaya, *J. Geophys. Res.*, 106(B7), 13 697–13 709, 2001.

Hales, A., A seismic discontinuity in the lithosphere, *Earth Planet. Sc. Lett.*, 7, 44-46, 1969.

Hart, P., *The Earth's Crust and Upper Mantle, volume II*, American Geophysical Union, Washington, D. C., 1969.

Hauck, M., Nelson, K., Brown, L., Zhao, W. & Ross, A., Crustal structure of the Himalayan orogen at similar to 90 degrees east longitude from Project INDEPTH deep reflection profiles, *Tectonics*, 17, 481–500, 1998.

Herquel, K., Wittlinger, G. and Guilbert, J., Anisotropy and crustal thickness of northern Tibet new constraints for tectonic modeling, *Geophy. Res. Lett.*, 22, 1925-1928, 1995.

Hermann, R., *Computer Programs in Seismology, volume VI*, USA, 2002.

Herrmann, R.B., *Computer Programs in Seismology*, p. 110, St Louis University, MO, USA, 2003.

Hiller, K., *On the Petroleum Geology of Bangladesh*, Bundesanstalt fur Geowissenschaften und Rohstoffe und Geologische Landesamter in der Bundesrepublic Deutsch, Hannover, 1988.

Hirn, A. & Sapin, M., The Himalayan zone of crustal interaction: suggestions from explosion seismology, *Ann. Geophys.*, *2(2)*, 123–130, 1984.

Hirn, A. et al., Crustal structure and variability of the Himalayan border of Tibet, *Nature*, *307(5946)*, 23–25, 1984a.

Hirn, A., Wittlinger, G., Zhong-Xin, X. & En-Yuan, G., Main features of the upper lithosphere in the unit between the High Himalayas and the Yarlung Zangbo Jiang suture, *Ann. Geophys.*, *2(2)*, 113–118, 1984b.

Holt, W., The active tectonics and structure of the Eastern Himalayan Syntaxis and surrounding regions, *PhD thesis*, University of Arizona, Tucson, AZ, 1989.

Holt, W., Ni, J., Wallace, T. & Haines, J., The active tectonics of the eastern Himalayan syntaxis and surrounding regions, *J. Geophys. Res.*, *96*, *(B9)*,14 595–14 632, 1991.

Hu, G. and Menke, W., Polarisation tomography for P wave velocity structure in southern California, *J. Geophys. Res.*, *99*, 15245-15256, 1994.

Jackson, I., *The Earth's Mantle, volume 1*, Cambridge University Press, 2000.

Jenkins, D. and Newton, R., Experimental determination of the spinel peridotite to garnet peridotite inversion at 900°C and 1000°C in the system CaO-MgO-AlO-SiO and at 900°C with natural garnet and olivine, *Earth Planet. Sc. Lett.*, *64*, 407-419, 1979.

Jordan, T. and Frazer, L., Crustal and upper mantle structure from Sp phases, *J. Geophys. Res.*, *80*, 1504-1518, 1975.

Julia, J., Ammon, C., Herrmann, R. and Correig, A., Joint inversion of receiver function and surface wave dispersion observations, *Geophys. J. Int.*, *143*, 99-112, 2000.

Jurkevics, A., Polarisation analysis of three-component array data, *B. Seismol. Soc. Am.*, *78*, 1725-1743, 1988.

Kaila, K., Reddy, P., Mall, D., Venkateswarul, N., Krishna, V. & Prasad, A., Crustal structure of the West Bengal basin, India from deep seismic-sounding investigations, *Geophys. J. Int.*, *111*, *(1)*,45–66, 1992.

Kanamori, H. and Press, F., How thick is the lithosphere, *Nature*, *226*, 330, 1970.

Kanamori, H., and D. Hadley, Crustal structure and temporal velocity change in southern California, *Pure Appl. Geophys.*, *113*, 257-280, 1975.

Kanasewich, E. R., *Time sequence Analysis in Geophysics*, The University of Alberta Press, 1975.

Kaneshima, S., Origin of crustal anisotropy: Shear wave splitting studies in Japan, *J. Geophys. Res.*, *95*, 11121-11133, 1990.

Karato, S., On the Lehmann discontinuity, *Geophy. Res. Lett.*, *22*, 2255-2258, 1992.

Kayal, J. & Zhao, D., Three-dimensional seismic structure beneath Shillong Plateau and Assam Valley, northeast India, *Bull. Seism. Soc. Am.*, *88*, 667–676, 1988.

Kayal, J., De, R. & Chakraborty, P., Microearthquakes at the Main Boundary Thrust in eastern Himalaya and the present-day tectonic model, *Tectonophysics*, *218*, *(4)*,375–381, 1993.

Kayal, J. R. & Arefiev, S. S., Shillong plateau earthquakes in northeast India region: complex tectonic model, 2006.

Kennet, B. and Engdahl, E., Travel times for global earthquake location and phase identification, *Geophys. J. Int.*, *105*, 429-465, 1991.

Khattri, K., Chander, R., Gaur, V., Sarkar, I. & Kumar, S., New seismological results on the tectonics of the Garhwal Himalaya, *Earth planet. Sci. Lett.*, *98*, 91–109, 1989.

Kind, R., Kosarev, G. & Petersen, N., Receiver functions at the stations of the German Regional Seismic Network (GRSN), *Geophys. J. Int.*, *121*, 191–202, 1995.

Kind, T. et al., Evidence from earthquake data for a partially molten crustal layer in Tibet, *Science*, *274*, 1692-1694, 1996.

Knopoff, L., The thickness of the lithosphere from the dispersion of surface waves, *Geophys. J. R. Astr. Soc.*, *76*, 55-81, 1983.

Kono, M., Gravity anomalies in east Nepal and their implications to the crustal structure of the Himalayas, *Geophys. J. R. Astr. Soc.*, *39*, 283–300, 1974.

Kumar, M., Saul, J., Sarkar, D., Kind, R. and K.Sukla, A., Crustal structure of the Indian shield: New constraints from teleseismic receiver functions, *Geophy. Res. Lett.*, *28*, 1339-1342, 2001.

Kumar, M., Saul, J., Sarkar, D., Kind, R. and K.Sukla, A., Lithospheric and upper mantle structure of the Indian shield, from teleseismic receiver functions, *Geophy. Res. Lett.*, *27(16)*, 2357-2360, 2000.

Langston, C. A., The effect of planar dipping structure on source and receiver responses for constant ray parameter, *Bull. Seismol. Soc. Am.*, *67*, 1029-1050, 1977.

Langston, C., Structure under Mt. Rainier, Washington, inferred from teleseismic body waves, *J. Geophys. Res.*, *84*, 4749-4762, 1979.

Le Fort, P., Himalayas: the collided range, present knowledge of the continental arc, *Am. J. Sci.*, *275A*, 1-44, 1975.

Leary, P., Crampin, S. and McEvilly, T., Seismic fracture anisotropy in the Earth,s crust: An Overview, *J. Geophys. Res.*, *95*, 11105-11114, 1990.

Lepine, J., Hirn, A., Pandey, M. & Tater, J., Features of the P-waves propagated in the crust of the Himalayas, *Ann. Geophys.*, *2(2)*,119–122, 1984.

Levin, V. and Park, J., P-SH conversions in a flat-layered medium with anisotropy of arbitrary orientation, *Geophys. J. Int.*, *131*, 253-266, 1997.

Levin, V., Park, J., Brandon, M., Jonathan, L., Peyton, V., Gordeev, E. and Ozerov, A., Crust and upper mantle of Kamchatka from teleseismic receiver functions, *Tectonophysics*, *358*, 133-265, 2001.

Lewis, J. L., S. M. Day, H. Magistrale, J. Eakins, and F. Vernon, Crustal thickenss of the Peninsular Ranges, Southern California, from teleseismic receiver functions, *Geology, in press*, 1999.

Li, X., Kind, R., Priestley, K., Sobolev, S., Tilmann, F., Yuan, X. and Weber, M., Mapping the Hawaiian plume conduit with converted seismic waves, Lett. Nature, 405, 938-941, 2000.

Ligorria, J. & Ammon, C., Iterative deconvolution and receiver-function estimation, Bull. Seism. Soc. Am., 89, 1395-1400, 1999.

Mackwell, S., Zimmerman, M. & Kohlstedt, D., High-temperature deformation of dry diabase with application to tectonics on Venus, J. Geophys. Res., 103, 975-985, 1998.

Maggi, A., Jackson, J., McKenzie, D. & Priestley, K., Earthquake focal depths, effective elastic thickness, and the strength of the continental lithosphere, Geology, 28, 495-498, 2000.

Maggi, A., Jackson, J., Priestley, K. & Baker, C., A re-assessment of focal depth distribution in southern Iran, the Tien Shan and northern India: do earthquakes really occur in the continental mantle?, Geophys. J. Int., 143, 629-661, 2000.

McCaffrey, R. & Abers, J., SYN3: a Program for Inversion of Teleseismic Body Wave Form on Microcomputers, Technical Report AFGL-TR-0099, Air Force Geophysical Laboratory, Hanscomb Air Force Base, MA, 1988.

McCaffrey, R. & Nabelek, F., Earthquakes, gravity and the origin of the Bali Basin: an example of a nascent continental fold-and-thrust belt, J. Geophys. Res., 92, 441-460, 1987.

McKenzie, D. & Fairhead, D., Estimates of the effective elastic thickness of the continental lithosphere from Bouguer and free air gravity anomalies, J. Geophys. Res., 102, 27 523-27 552, 1997.

McKenzie, D. & Jackson, J., Conditions for flow in the continental crust, Tectonics, 21(6), doi: 10.1029/2002TC001394, 2002.

McNamara, D. E. and Owens, T. J., Azimuthal shear wave velocity anisotropy in the Basin and Range Province using Moho Ps converted phases, J. Geophys. Res., 98, 12003-12017, 1993.

Mitra, S., Priestley, K., Bhattacharyya, A. K. and Gaur, V. K., Crustal structure and earthquake focal depths beneath northeastern India and southern Tibet, *Geophys. J. Int., 160,* 227-248, 2005.

Molnar, P. & Chen, W. P., Focal depths and fault plane solutions of earthquakes under the Tibetan Plateau, *J. Geophys. Res., 88,* 1180–1196, 1983.

Molnar, P. & Lyon-Caen, H., Fault plane solutions of earthquakes and active tectonics of the Tibetan Plateau and its margins, *Geophys. J. Int., 99,* 123–153, 1989.

Molnar, P. & Pandey, M., Rupture zones of great earthquakes in the Himalayan region, *Proc. Indian Acad. Sci. (Earth Planet. Sci.), 98,* 61–70, 1989.

Molnar, P., Chen, W. P., Fitch, T. J., Tapponnier, P., Warsi, W. E. K. & Wu, F., Structure and tectonics of the Himalaya: a brief summary of relevant geophysical observations, in *Himalaya: Sciences de la Terre,* Colloque Internationaux du CNRS no 268, pp. 269–294, Editions du Centre Nationale de la Recherche Scientifique, Paris, 1977.

Mukhopadhyay, S., Chander, R. & Khattri, K., Crustal properties in the epicentral tract of the great 1897 Assam earthquake, northeast India, *Tectonics, 283,* 311–330, 1997.

Marson-Pdgeon, K. and Savage, M., Frequency-dependent anisotropy in Wellington, New Zealand, *Geophy. Res. Lett., 24,* 3297-3300, 1997.

Melbourne, T. and Helmberger, D., Fine structure of the 410-km discontinuity, *J. Geophys. Res., 103,* 10091-10102, 1998.

Melosh, J., Shear stress on the base of lithospheric plate, *PAGEOPH, 115,* 429-438, 1977.

Nabelek, J., Determination of earthquake source parameters from inversion of body waves, *PhD thesis,* Massachusetts Institute of Technology, Cambridge, MA, 1984.

Nandy, D. & Das Gupta, S., Application of remote sensing in regional geological studies - a case study in northeastern part of India, in

Proceedings of the International Seminar on Photogrammetry and Remote Sensing for Developing Countries, pp. T.4-P./6.1-T.4-P/6.4. Survey of India, New Delhi, India, 1986.

Nelson, K. *et al.*, 1996. Partially molten middle crust beneath southern Tibet: synthesis of project INDEPTH results, *Science, 274*, 1684-1688, 1996.

Ni, J. & Barazangi, M., Seismotectonics of the Himalayan collision zone — geometry of the underthrusting Indian plate, *J. Geophys. Res., 89*, 1147-1163, 1984.

Nolet, G. and Dahlen, F., Wave front healing and the evolution of seismic delay times, *J. Geophys. Res., 105*, 19043-19054, 2000.

Oreshin, S., Vinnik, L. and Peregoudov, D., Lithosphere and asthenosphere of the Tien Shan imaged by S receiver functions, *Geophy. Res. Lett., 29*, 1029-1032, 2002.

Owens, T.J., Zandt, G. & Taylor, S.R., Seismic evidence for an ancient rift beneath the Cumberland Plateau, Tennessee: a detailed analysis of broadband teleseismic P-waveforms, *J. Geophys. Res., 89*, 7783-7795, 1984.

Pandey, M., Tandukar, R., Avouac, J., Lave, J. & Massot, J., Interseismic strain accumulation on the Himalayan crustal ramp (Nepal), *Geophys. Res. Lett., 22*, 751-754, 1995.

Park, J., Multitaper Spectral Analysis of High-Frequency Seismogram, *J. Geophys. Res., 92*, 12675-12684, 1987.

Park, J. and Levin, V., Receiver functions from multi-taper spectral correlation estimates, *B. Seismol. Soc. Am., 90(6)*, 1507-1520, 2000.

Park, J., Vernon, F. and Lindberg, C., Frequency Dependent Polarisation Analysis of High-Frequency Seismogram, *J. Geophys. Res., 92*, 12664-12674, 1987.

Peng, X. and Humphreys, E. D., Moho dip and Crustal Anisotropy in Northwestern Nevada from Teleseismic Receiver Functions, *B. Seismol. Soc., Am., 87(3)*, 745-754, 1997.

Powell, C., Roots, S. and Veevers, J., pre-breakup continental extension in East Gondwana and the early opening of the eastern Indian Ocean, *Tectonophysics, 155,* 261-283, 1988.

Priestley, K. F., Cipar, J., Egorkin, A. and Pavlenkova, N., Upper-mantle velocity structure beneath the Siberian platform, *Geophys. J. Int.,* pages 369-378, 1994.

Priestley, K., Zandt, G. & Randal, G., Crustal structure in eastern Kazakh, U.S.S.R. from teleseismic receiver functions, *Geophys. Res. Lett., 15,* 613-616, 1988.

Priestley, K., Baker, C. & Jackson, J., Implications of earthquake focal mechanism data for the active tectonics of the south Caspian Basin and surrounding regions, *Geophys. J. Int., 118,* 111-141, 1994.

Rai, S., Priestley, K., Suryaprakasham, K., Srinagesh, D., Gaur, V. and Du, Z., Crustal shear velocity structure of the south Indian shield, *J. Geophys. Res., 108,* 2088-2099, 2003.

Rai, S., Prakasam, K. & Agrawal, N., *Pn* wave velocity and Moho geometry in northeastern India, *Proc. Indian Acad. Sci. (Earth Planet. Sci.), 108(4),* 297-304, 1999.

Rajendran, K., Talwani, P. and Gupta, H., State of Stress in the Indian subcontinent, *Curr. Sci. India, 62,* 86-93, 1992.

Ramachandran, C., P-wave velocity in granulites from South India: Implication for the continental crust, *Tectonophysics, 201,* 187-198, 1992.

Ramesh, D. and Prakasham, K., Shear wave splitting observations from the Indian shield, *Proc. Indian Acad. Sci. (Earth Planet Sci.), 104,* 85-114, 1995.

Ramesh, D., Srinagesh, D., Rai, S. and Prakasham, K., Anomalous granulite crust of South India- signatures from converted teleseismic waves, *Earth Plane. Sc. Lett. 101,* 283-298, 1992.

Reddy, C., Fiky, G., Kato, T., Shimada, S. and Kumar, V., Crustal strain field in the Deccan trap region, western India, derived from GPS measurements, *Earth Planets Space, 52,* 965-969, 2000.

Richards-Dinger, K. B., and P. M. Shearer, Estimating crustal thickness in southern California by stacking PmP arrivals, *J. Geophys. Res.*, *102*, 15,211-15,224, 1997.

Samson, J., Pure states, polarized waves and principal components in the spectra of multiple, geophysical time-series, *Geophys. J. R. Astr. Soc.*, *72*, 647-664, 1983a.

Samson, J., The spectral matrix, eigenvalues and principal components in the analysis of multichannel geophysical data, *Ann. Geophysicae*, *1*, 115-119, 1983b.

Savage, M., Lower crustal anisotropy or dipping boundaries? Effects on receiver functions and a case study in New Zealand, *J. Geophys. Res.*, *103*, 15069-15087, 1998.

Sarkar, D., Reddy, P., Kaila, K. & Prasad, A., Multiple diving waves and high-velocity gradients in the Bengal sedimentary basin, *Geophys. J. Int.*, *121(3)*, 969-974, 1995.

Seeber, L. & Armbruster, J., Great detachment earthquakes along the Himalayan arc and long-term forecasts, in *Earthquake Prediction: an International Review*, Maurice Ewing Series *Vol. 4*, pp. 259-277, eds Simpson, D. & Richards, P., American Geophysical Union, Washington, DC, 1981.

Shamsuddin, A. & Abdullah, S., Geologic evolution of the Bengal Basin and its implication in hydrocarbon exploration in Bangladesh, *Indian J. Geol.*, *69*, 93-121, 1997.

Sheehan, A.F., Abers, G.A., Jones, C.H. & Lerner-Lam, A.L., Crustal thickness variation across the Colorado Rocky Mountains from teleseismic receiver functions, *J. Geophys. Res.*, *100*, 20 391-20 404, 1995.

Singh, D., Shear wave velocity structure over the eastern Indian subcontinent, *Tectonophysics*, *230*, 127-134, 1994.

Tong, C., Gudmundsson, O. and Kennett, B., Shear wave splitting in refracted waves returned from the upper mantle transition zone beneath northern Australia, *J. Geophys. Res.*, *99*, 15783-15797, 1994.

Vergne, J., Wittlinger, G., Farra, V. and Su, H., Evidence for upper crustal anisotropy in the Songpan-Ganze (northern Tibet) terrane, *Geophys. Res. Lett.*, *30*, 1552-1556, 2003.

Verma, R.K. & Mukhopadhyay, M., An analysis of gravity field in northeastern India, *Tectonics*, *42*, 283-317, 1977.

Vinnik, L., Detection of waves converted from P to SV in the mantle, *Phys. Earth Planet. In.*, *15*, 39-45, 1977.

Vinnik, L., Chenet, H., Gagnepain-Beyneix, J. and Lognonne, P., First seismic receiver functions on the Moon, *Geophys. Res. Lett.*, *28*, 3031-3034, 2001.

Wiens, D. & Stein, S., Age dependence of intraplate seismicity and implications for lithospheric evolution, *J. Geophys. Res.*, *88*, 6455-6468, 1983.

Webb, S. and Wood, B., Spinel-pyroxene-garnet relationships and their dependence on cr/al ratio, *Contr. To Mineralogy and Petrology*, *92*, 471-480, 1986.

Weeraratne, D., Donald, W. and Fisher, K., Evidence for an upper mantle plume beneath the Tanzanian craton from Rayleigh wave tomography, *J. Geophys. Res.*, *108*, 2427-2446, 2003.

Woodhouse, J. and Wong, Y., Amplitude, phase and path anomalies of mantle waves, *Geophys. J. R. Astr. Soc.*, *87*, 753-773, 1986.

Yu, Y. and Park, J., Hunting for azimuthal anisotropy beneath the Pacific Ocean region, *J. Geophys. Res.*, *88*, 161-204, 1994.

Yuan, X., Ni, J., Kind, R., Mechie, J. and Sandvol, E., Lithospheric and upper mantle structure of southern Tibet from a seismological passive source experiment, *J. Geophys. Res.*, *102*, 27491-17500, 1997.

Zandt, G., Myers, S. C. and Wallace, T. C., Crust and mantle structure across the Basin and Range – Colorado Plateau boundary at 37°N latitude and implementation for Cenozoic extensional mechanism, *J. Geophys. Res.*, *100*, 10529-10548, 1995.

Zhao, D. P., Kanamori, H. and Humphreys, E., Simultaneous inversion of local and teleseismic data for the crust and mantle structure of southern California, *Phys. Earth Planet. Inter.*, *93*, 191-214, 1996.

Zhu, L., Estimation of crustal thickness and Vp/Vs ratio beneath the Tibetan Plateau from teleseismic converted waves(abstract), *Eos Trans. AGU*, *74(16)*, Spring Meet Suppl., 202, 1993.

Zhu, L. and Kanamori, H., Variation of crustal thickness in southern California from teleseismic receiver functions at TERRAscope stations (abstract), *Eos Trans. AGU*, *75(44)*, Full Meet Suppl., 484, 1994.

Zhu, L. & Helmberger, D., Intermediate depth earthquakes beneath the India–Tibet collision, *Geophys. Res. Lett.*, *23*, 435–438, 1996.

Zhu, L. and Kanamori, H., Moho depth variation in southern California from teleseismic receiver functions, *J. Geophys. Res.*, *105*, 2969-2980, 2000.

Appendix A

Forward Modelling Tests of the Crustal Models Obtained by Joint Inversion Results

It is worthwhile to test the significant features of the crustal model obtained from joint inversion results by forward modelling. Accordingly for the results obtained from joint inversion of receiver functions and surface wave dispersion data of NE India stations, forward modelling were undertaken to test the influence on the fit to the receiver functions of each model feature. Any feature which when removed did not significantly reduce the fit to the data was discarded such that simplest model able to fit the data was found.

Following figures summarise the forward modelling tests for the receiver structure at the NE India stations based on the receiver function stacks used for the joint inversion. During the forward modelling tests it is assumed that the minor changes made to the velocity models will not significantly alter the fit to the group velocity observations, hence the forward modelled dispersion curves are not presented in the figures.
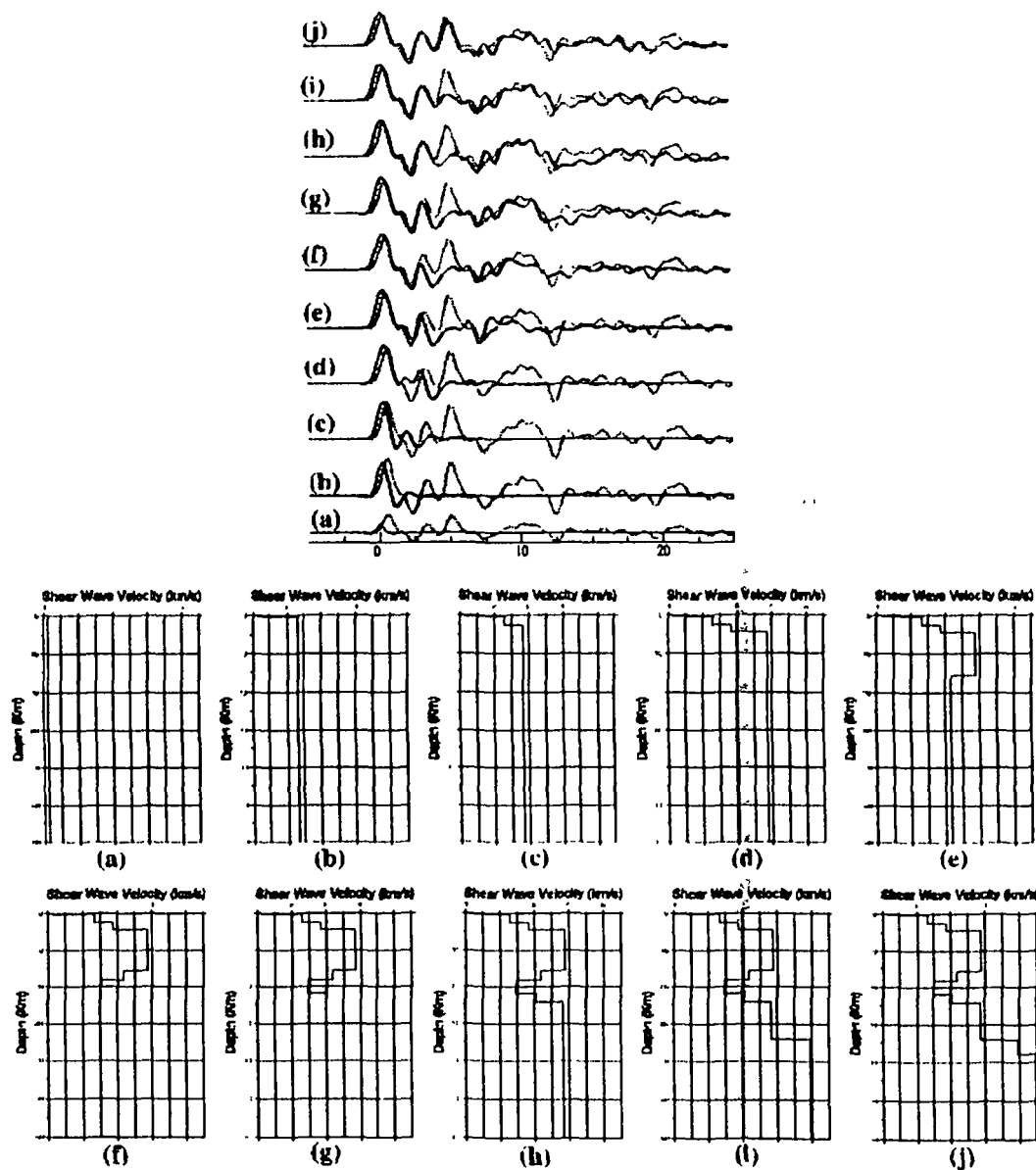
Figure A.1: Forward modelling tests for AGT. (top) Observed radial receiver functions (faint lines) and synthetic receiver functions (solid and thick lines) calculated for the corresponding velocity models (a-a, b-b, c-c etc.) shown in bottom.
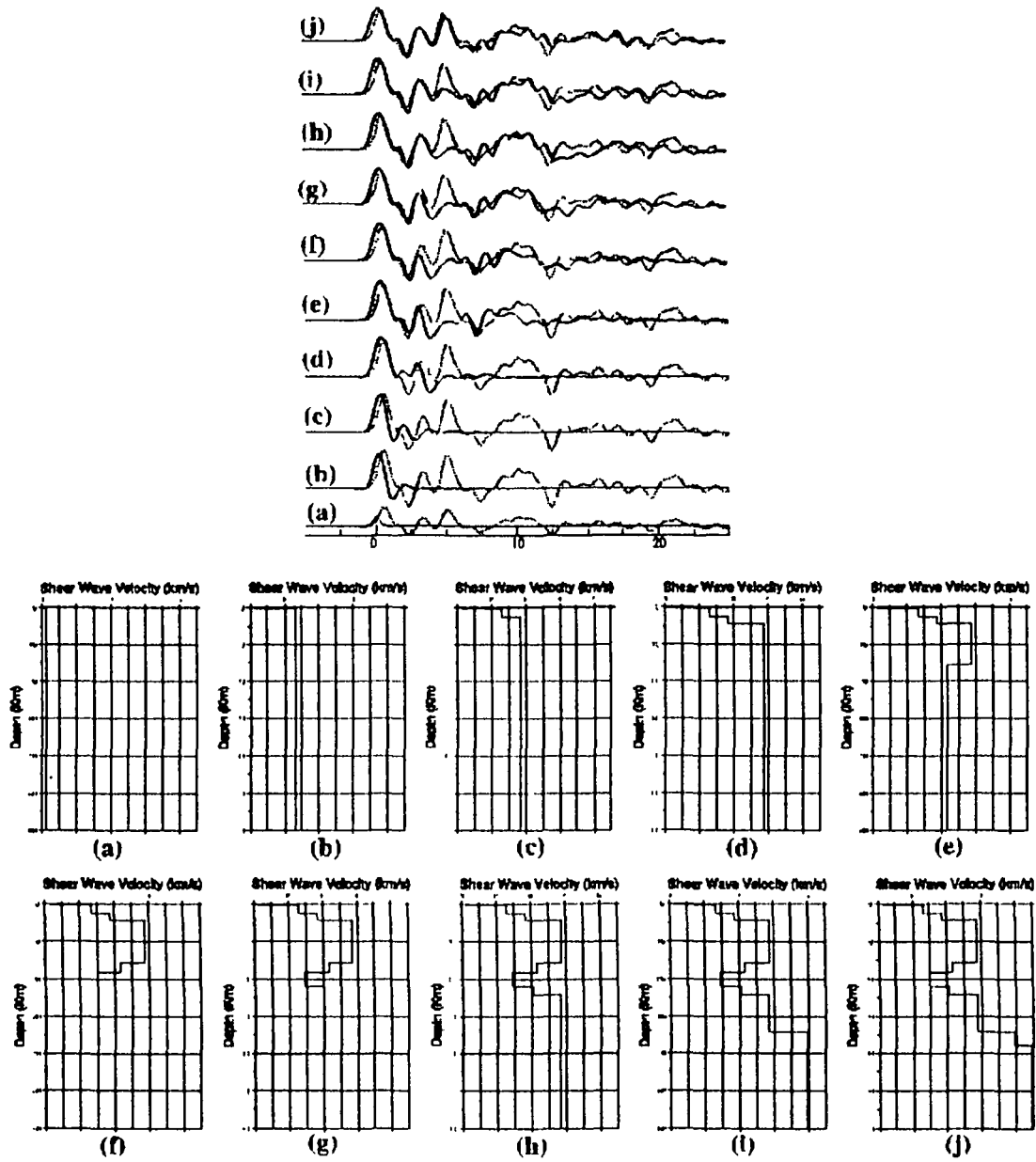
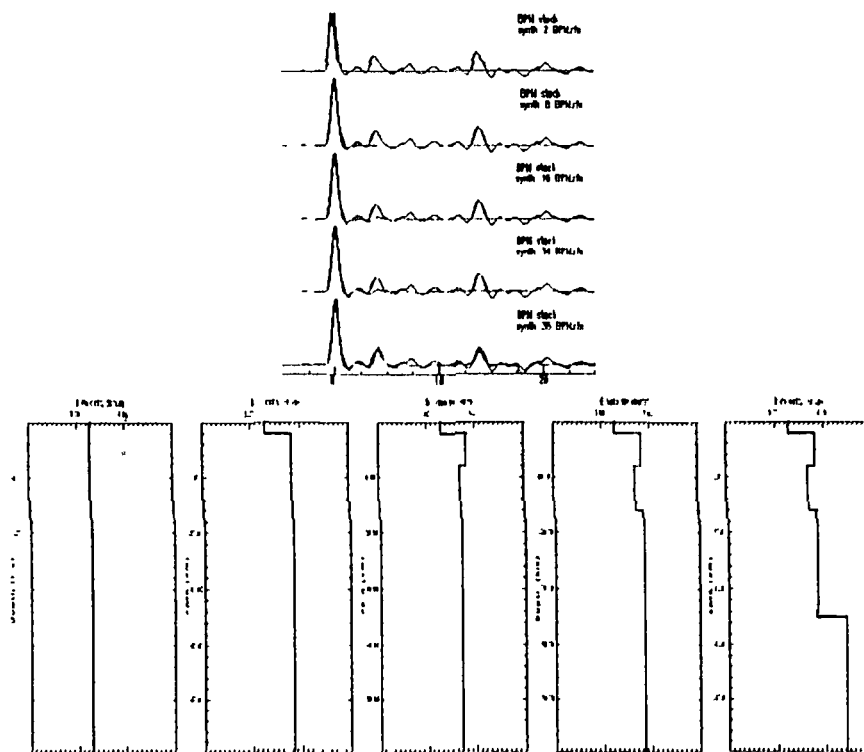Figure A.3: Forward modelling tests for TWG. Format of plot is the same as for FigureA.1.

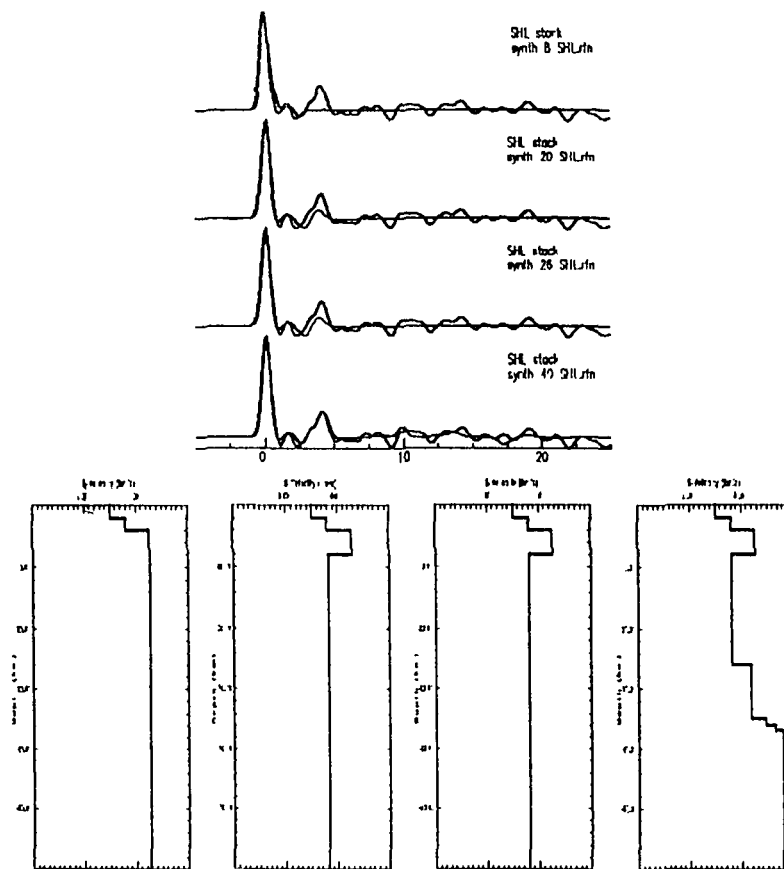Figure A.3: Forward modelling tests for BPN. Format of plot is the same as for FigureA.1.

Figure A.4: Forward modelling tests for SHL. Format of plot is the same as for FigureA.1.
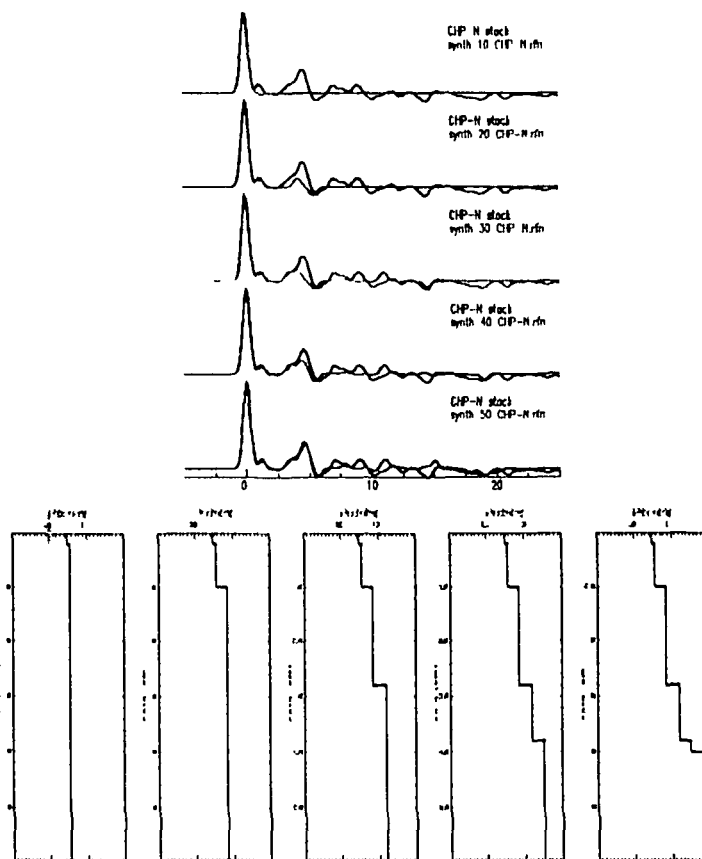
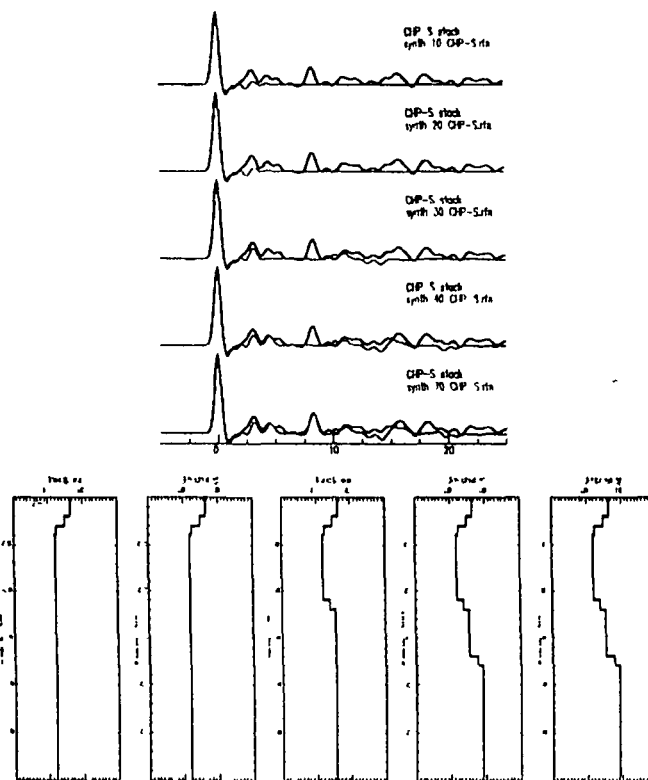Figure A.5: Forward modelling tests for CHP-N. Format of plot is the same as for FigureA.1.

Figure A.6: Forward modelling tests for CHP-S. Format of plot is the same as for FigureA.1.
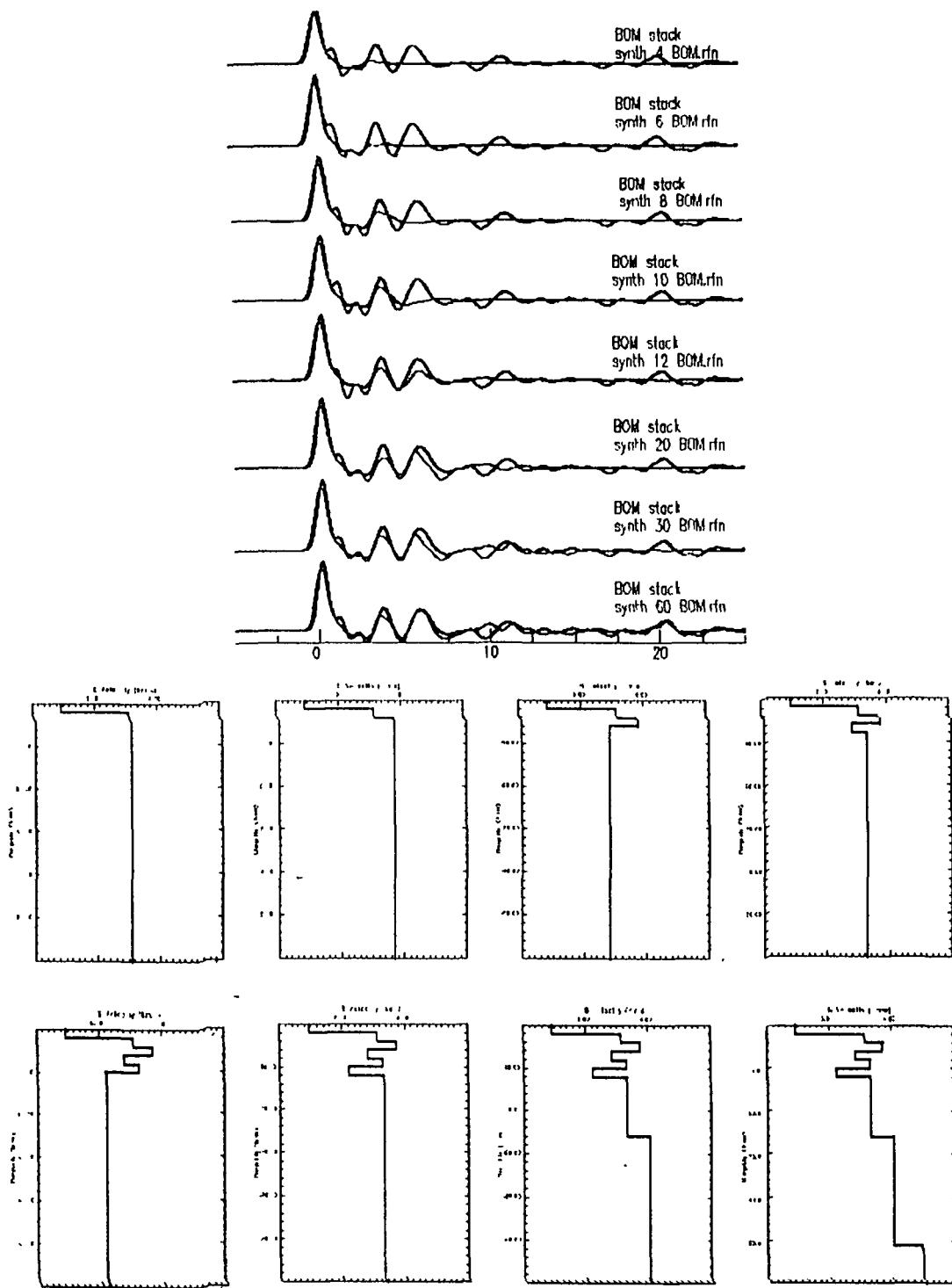
Figure A.7: Forward modelling tests for GAU. Format of plot is the same as for FigureA.1.

Figure A.8: Forward modelling tests for TEZ. Format of plot is the same as for FigureA.1.

Figure A.9: Forward modelling tests for BOM. Format of plot is the same as for FigureA.1.